Free Surface Liquid Metal Flow in a Surface Normal Magnetic Field for Fusion Applications



Naomi Thoitu Mburu

University College

University of Oxford

A thesis submitted for the degree of

Doctor of Philosophy

Trinity 2024

Abstract

Naomi Thoitu Mburu
University College, University of Oxford
A thesis submitted for the degree of Doctor of Philosophy, Trinity 2024

Free Surface Liquid Metal Flow in a Surface Normal Magnetic Field for Fusion Applications

One major challenge to the realisation of commercial fusion energy is the development of plasma facing components (PFCs) that can withstand large heat and particle fluxes. A liquid metal PFC can reduce PFC surface erosion due to the self-healing nature of liquids, increase heat removal capabilities, and reduce plasma exhaust recycling. These benefits can significantly reduce reactor maintenance needs. There is a lack of quantitative experimental studies of liquid metal flows in a surface normal magnetic field. The aim of this thesis was to design and build an experimental facility, the Oxford Liquid Metal Experiment (OLME), to quantify the effects of surface normal magnetic field on thin film ($\approx 5mm$), slow ($\approx 40-67mm/s$) developing liquid metal flow in a flat, conductive channel.

The effect of a magnetic field on liquid metal height was quantified within the ranges of 0.075 T - 0.16 T and 0.0318 kg/s - 0.053 kg/s. This was accompanied by the derivation of an analytical solution for developing flow across a flat channel in the presence of a surface normal magnetic field. Additionally, the use of ANSYS [1] CFX to model low aspect ratio geometry flows was validated, and a 3D numerical model of the OLME was then developed using this software. This allowed for the unique comparison of analytical, numerical and experimental results.

The primary result achieved on the OLME was the novel quantitative measurement of magnetohydrodynamic (MHD) effects in a surface normal magnetic field, and comparison to relevant numerical and analytical solutions. The trend of increasing height change with increasing Hartmann number was confirmed, particularly for higher Hartmann number flows. Methods to improve flow wetting and measure fluid velocity were explored as it was determined that these were key barriers to realising liquid metal PFCs.

This work contributed a new facility that has great future potential to measure different field orientations, channel geometries, and channel angles. The development of a relevant numerical model provided a much needed bridge between experimental and analytical liquid metal MHD work. There remains much left to be explored regarding liquid metal MHD flow before this technology will be suitable for use in a commercial fusion device. This thesis concluded with recommendations for future work.

[1] www.ansys.com

Keywords: plasma facing components, tokamak, magnetohydrodynamics

Dedication

For my brother, Nick, whom I loved dearly.

Acknowledgements

I would like to thank my primary supervisor, Professor Peter Ireland, for his guidance, support, and great humour throughout this process. I would also like to thank Peter Buxton, my industrial supervisor, and the Tokamak Energy team who provided expert knowledge on tokamak science and assisted me in every step of my DPhil process. Also, thank you to Tokamak Energy for providing the financial support required to build the OLME. Another huge thanks belongs to Andrei Khodak, who joined my supervision team after the pandemic and provided invaluable numerical and analytical knowledge and advice. Along the way, I received support from many other academics including Jack Nicholas, Ghassan Antar, Daniel Ibanez, and Rajesh Maingi, and I am truly grateful for their support. Also, I would like to thank Zhen Sun and Adam Fisher for showing me around the Liquid Metal Experiment at Princeton Plasma Physics Laboratory and providing a sounding board to discuss ideas for my own liquid metal experiment at Oxford. Along that same vein, I would like to thank the team of graduate students and post docs at the Centre for Plasma Materials Interactions at the University of Illinois, Urbana Champaign who were always happy to brainstorm and troubleshoot with me.

From the Engineering Science department, there are many people whom I must thank. When I first joined the lab, Gladys Ngetich was a source of encouragement and light. I must thank her for her crash course in latex- this thesis wouldn't exist without that! I would also like to recognise Lucy Cross who made DPhil and life during the pandemic bearable. I would like to thank Emily Berexa and Emeka Nwangele for brightening the last few years of my DPhil, and supervising many tests in the final mad dash to the finish line. In the summer of 2021, I hired an undergraduate intern, James Leader, who infused enthusiasm and new ideas into my research- thank you! I must also thank Alex Murray for supervising many of my experiments and providing general assistance along the way. Thank you to all of the technicians, building staff, and administrative team for supporting the construction of my experiments and handling my many purchase order requests. Special thank you to Jason McCluskey for helping me deal with the constant mess that liquid metal leaves after experiments.

Outside of the lab, I must thank the many amazing friendships I have gained while in Oxford. Starting with my friends who have been with me in Oxford since 2018 (Ruthie and Jelani), thank you for all of the unforgettable dinner parties, long deep conversations, and endless laughs throughout the years. Huge thanks to my running group (Kevin, Sandra, Gloria, Natasha and Rita) who made sure I left my house during the pandemic and have become lifelong friends. I would also like to thank Kelly-Ann for her friendship and support. From University College, I must thank Andrew Gregory for providing pastoral support when needed, and Valerie Amos for her efforts in making the college a more welcoming space. From Rhodes House, I must thank Mary Eaton for her endless support through the rollercoaster of my DPhil, and the rest of Rhodes House for providing a safe haven. Finally, I must thank the members of the Weldon House for providing endless entertainment during the pandemic.

To end, I must thank my family for being supportive of my journey and always willing to help in any way possible. Thank you to my friends in the USA, Olanike and Mary, for always checking in on me and rooting me on from afar. Thank you to my undergraduate research mentor Dr. Slaughter for continuously helping me navigate the ups and down of the DPhil. Thank you to my partner Victor for providing endless love, support and wonderful memories from my time in Oxford. Finally, thank you to my parents for all of the sacrifices made and support given to help me reach this point, and to my extended family for continuously rooting me on.

Contents

Abstract i

Dedication ii

Acknowledgements iii

Nomenclature xvi

1 INTRODUCTION 1

1.1 Nuclear Fusion: An Overview 1

1.1.1 Magnetic Field Orientations 5

1.1.2 Fusion is a Global Initiative 7

1.1.3 The Case for Liquid Metal Plasma Facing Components 9

1.2 Research Aims 13

1.3 Thesis Contributions 14

1.4 Thesis Structure 15

2 LITERATURE REVIEW OF LIQUID METAL PLASMA FACING COMPONENTS 17

2.1 Overview 17

2.2 Magnetohydrodynamics 17

2.3 Literature Review of Analytical Analyses of Liquid Metal Free Surface MHD 20

2.4 Literature Review of Numerical Modelling of Liquid Metal Free Surface MHD 22

2.5 Literature Review of Experimental Liquid Metal Free Surface MHD 25

2.5.1 Solid Plasma Facing Components 25

2.5.2 Liquid Metal PFC Experiments 28

2.5.2.1 Liquid Metal Experiments in Fusion Devices 28

2.5.2.2 Bench Scale Free Surface Liquid Metal Experiments . . . 29

2.6 Summary of Literature Gaps 32

3 LIQUID METAL EXPERIMENTAL FACILITY AND APPARATUS 34
3.1 Overview . . . 34
3.2 Background Information . . . 34
3.2.1 Overview . . . 34
3.2.2 Choice of Liquid Metal . . . 35
3.3 Experimental Facility Overview . . . 36
3.3.1 Test Section . . . 37
3.3.2 Electromagnet . . . 39
3.3.2.1 Electromagnet Specifications . . . 39
3.3.2.2 Electromagnet Modelling . . . 41
3.3.3 Safety . . . 46
3.3.3.1 Magnet Safety . . . 46
3.3.4 Instrumentation . . . 49
3.3.4.1 Laser Triangulation Methodology . . . 51
3.3.5 Labview . . . 52
3.4 Looking to the Future: Experimental Incorporation of TEMHD Effects . . . 53
3.5 Looking to the Future: Liquid Metal Velocity Tracking Technique Development . . . 55
3.6 Summary . . . 61

4 ANALYTICAL AND NUMERICAL MODELLING OF LIQUID METAL FLOW 62
4.1 Analytical and Numerical Modelling Approach . . . 62
4.1.1 ANSYS CFX MHD Solver Theory . . . 64
4.1.1.1 Boundary Conditions . . . 66
4.1.2 Numerical Modelling Overview . . . 67
4.1.2.1 Mesh Sensitivity Analysis . . . 72
4.2 Benchmarking for Fully Developed MHD Flow . . . 75
4.2.1 Validation Cases . . . 75
4.2.1.1 2D Duct Flow with Non Conducting Walls and Transverse Magnetic Field . . . 75
4.2.1.2 2D Duct Flow with Conductive Hartmann Walls and Transverse Magnetic Field . . . 79
4.2.1.3 2D Free Surface Flow with Transverse Magnetic Field . . . 80
4.2.1.4 2D Free Surface Flow with Surface Normal Magnetic Field 83
4.3 Benchmarking for Developing Flow MHD . . . 86
4.3.1 Analytical Derivation of Developing Flow in a Flat Channel . . . 87
4.3.1.1 Numerical Modelling of Developing 3D Free Surface Flow on a Flat channel . . . 91
4.4 Method for Experimental Validation . . . 102

4.5 Summary . . . 103

5 Experimental Measure of Surface Normal Field Effects 104
5.1 Data Collection Methodology . . . 104
5.2 Summary of Experimental Findings . . . 107
5.3 Areas for Improvement . . . 114
5.4 Challenges for Liquid Metal Flows . . . 117
5.4.1 Alternative Channel Designs . . . 119
5.4.2 Contact Angle Theory and Measurements . . . 124
5.4.3 Contact Angle Measurements . . . 124
5.4.4 Dynamic Surface Wetting . . . 129
5.5 Summary . . . 132

6 SUMMARY AND CONCLUSION 133
6.1 Summary of Major Themes and Assessment of Aims . . . 134
6.1.1 OLME Development . . . 134
6.1.2 Analytical and Numerical Modelling of OLME Experimental Set Up 134
6.1.3 Analytical, Numerical, and Experimental Result Comparison . . . 135

7 RECOMMENDATIONS 137
7.1 Suggested Improvements to the OLME . . . 137
7.2 Suggested Future Experiments . . . 138
7.2.1 MHD Experiments . . . 138
7.3 Suggested Improvement for the Analytical and Numerical Models . . . 138

Bibliography 140

Appendix A Data Processing MATLAB File 153

Appendix B Particle Tracking Velocity Method 156

List of Figures

1.1 Plot of the reaction rate against the plasma temperature for three potential fusion fuel combinations where D is deuterium, T is tritium and He is helium (8). . . . 3

1.2 Comparison of a) tokamak and b) stellarator magnetic field configurations from (11) . . . 5

1.3 Diagram of magnetic field coils and resultant field orientations in a tokamak, from (12). . . . 6

1.4 Diagram of a limiter in a tokamak, showing the poloidal (red) and toroidal field (blue) components. An additional frame of the limiter shows the direction of the streamwise, surface normal and transverse components, shown in red and blue for those contributed by the poloidal and toroidal fields in this scene, respectively. . . . 7

1.5 Map of public institution involvement in nuclear fusion research, from (3). The colour map represent the number of institutions in each country. . . . 9

1.6 Map of private company involvement in commercialised fusion development (excluding work on DEMO), from (3). The colour map represent the number of institutions in each country. . . . 10

1.7 Schematic of the plasma facing components in a fusion device showing a limited plasma (a) and a diverted plasma (b) from (20). . . . 10

2.1 Plot of numerical and experimental results produced on the Liquid Metal Experiment (LMX) at PPPL for galinstan flow across a flat channel in the presence of 0 (black lines), 0.2 T (orange lines), and 0.3 T (blue lines) transverse magnetic fields. (Figure 5 from (45)) . . . 25

2.2 Tungsten monoblock divertor after 300 thermal cycles at 20 $\frac{MW}{m^2}$, from (71). (a) shows the impacted area on the monoblock, and (b) and (c) show cracks formed due to high heat flux loading. . . . 27

2.3 Plot of energy confinement time in the Current Drive Experiment Upgrade spherical tokamak device for trials run with liquid lithium (red) and solid lithium (blue), from (74). . . . 28

2.4 Summary plot of liquid metal experiments described in this chapter showing relative liquid metal thickness and velocity (the experiments described in this thesis are noted by the yellow star). These images include Figure 5 from (44), Figure 8 from (30), Figure 48 from (87), Figure 12 from (45), Figure 4.2 from (62), Figure 3 from (88), Figure 3 from (82) , and Figure 32 from (77) 32

3.1 CAD drawing of the Oxford Liquid Metal Experiment, showing the electromagnet, channel, and laser triangulation system 35
3.2 Process flow diagram for the liquid metal loop constructed for the OLME. The blue lines represent flow of argon, and the black lines represent flow of galinstan. 37
3.3 Top view of the channel design, showing the copper channel slotted into the polycarbonate base channel. Flow occurs from right to left. 38
3.4 CAD drawing of the electromagnet labelled with key features. 40
3.5 Finite Element Magnetic Model of the magnetic field present at full power (1800 A). The relative location of the channel is shown in grey. 43
3.6 Comparison of magnetic field output near the bottom coil surface from the magnet (blue points) compared to the FEMM model (orange points). 44
3.7 Results from an ANSYS Mechanical FEA analysis of the bottom copper coil with iron core heating over 400 seconds with 200 A current. 44
3.8 Comparison of ANSYS Mechanical FEA simulated temperature and experimental (actual) temperature of the bottom copper coil with iron core heating over 400 seconds with 200 A current. 45
3.9 Comparison of ANSYS Mechanical FEA simulated temperature and experimental (actual) temperature of the top copper coil with air core heating over 400 seconds with 200 A current. 46
3.10 Schematic of the magnet and relevant safety related control systems. 48
3.11 Side-view schematic of liquid metal flow and relevant diagnostics. 50
3.12 Top view schematic of liquid metal flow and laser line overlay, showing the position of laser line on the liquid metal surface. 50
3.13 Schematic illustrating the triangulation method, from (105) 51
3.14 Labview set up for data capture and system monitoring. 53
3.15 Comparison curve showing average velocity as a function of toroidal magnetic field for a 20 mm wide channel for A) lithium and B) galinstan, assuming a temperature gradient of 2500 K/m, Seebeck coefficients of 2.5e-5 V/K for lithium and 1.24e-5 for galinstan, and no pressure gradient. A stainless steel channel was used. 55

3.16 Matrix of possible optical velocity measurement combinations. Red signifies system incompatibility. Yellow signifies slight or possible compatibility. Green signifies system compatibility. 57
3.17 Diagram of partially embedded, 1 mm galinstan or gallium particles flowing in a 1 mm galinstan film. 58
3.18 Experimental set up for galinstan heat tracking studies 59
3.19 Heat tracking experimental set up. 60

4.1 Illustration (not to scale) of electric current lines in the case of conductive substrate and walls for transverse magnetic field and surface normal magnetic field. The blue area represents the channel walls, the grey area represents the fluid, and the yellow represents the current path. 67
4.2 Illustration (not to scale) of liquid metal duct flow through insulated walls in the presence of transverse magnetic field. The location of Hartmann and Shercliff layers are shown. 68
4.3 Illustration (not to scale) of liquid metal duct flow through conductive Hartmann walls and insulated Shercliff walls in the presence of transverse magnetic field. The location of Hartmann and Shercliff layers are shown 69
4.4 Illustration (not to scale) of free surface, liquid metal flow through all conductive walls in the presence of a transverse magnetic field. The location of Hartmann and Shercliff layers are shown 69
4.5 Illustration (not to scale) of free surface, liquid metal flow through all conductive walls in the presence of a surface normal magnetic field. The location of Hartmann and Shercliff layers are shown 70
4.6 Mesh sensitivity analysis results for Hartmann number 76 run for duct flow with non conductive walls. 74
4.7 Optimum mesh generated for the insulated walls case with Hartmann number 76. 74
4.8 Velocity contour plot for flow with insulating walls in the presence of transverse (x direction) magnetic field, where flow is in the z direction 78
4.9 Velocity contour for the case of conducting Hartmann walls in the presence of transverse (x direction) magnetic field, where flow is in the z direction. . 79
4.10 Velocity contour for the case of free surface flow in the presence of transverse (x direction) magnetic field, with flow in the z direction. 82
4.11 Current density vectors showing the direction and magnitude of the induced current. The colour map represents the component of the current density that is perpendicular to the magnetic field. 82
4.12 Force vectors showing the generated MHD drag force. The colour map represents the magnitude of the MHD drag force. 83

4.13 Velocity contour for the case of free surface flow in the presence of a surface normal (y direction) magnetic field, with flow in the z direction. 85
4.14 Current density vectors showing the direction and magnitude of the induced current. The colour map represents the component of the current density that is perpendicular to the magnetic field. 85
4.15 Force vectors showing the generated MHD drag force. The colour map represents the magnitude of the MHD drag force. 86
4.16 2D schematic of developing flow down a channel, showing the control volume outlined in red. 87
4.17 Mesh sensitivity analysis performed for a 3D simulation of liquid metal flow in ANSYS CFX. Liquid metal free surface height along the centreline of the channel was compared for various meshes. One mesh was made with all tetrahedral elements, and the other four were made using hexahedral elements on the fluid domain and tetrahedral elements on the solid domain, as well as inflation layers near the boundary region. 92
4.18 Current density streamlines for the case of B = 0.16 T and a flow rate of 0.053 kg/s showing a recirculating induced current. 93
4.19 Transverse velocity profile for the case of B = 0.16 T and a 0.053 kg/s flow rate, showing high velocity jet formation along the walls parallel to the surface normal magnetic field. 94
4.20 Velocity contour plot on the free surface, for the 3D ANSYS model of developing flow across a channel for a flow rate of 0.053 kg/s and magnetic field of 0.16 T. Flow is from left to right, along to z axis, and the magnetic field is surface normal (y direction). 94
4.21 Streamwise velocity contour plot along the channel centreline for a flow rate of 0.053 kg/s and magnetic field of 0.16 T. Flow is from left to right, along to z axis, and the magnetic field is surface normal (y direction). 95
4.22 Fluid height along the channel length for a flow rate of 0.0318 kg/s at various values of magnetic field. 96
4.23 Fluid height along the channel length for a flow rate of 0.0424 kg/s at various values of magnetic field. 97
4.24 Fluid height along the channel length for a flow rate of 0.053 kg/s at various values of magnetic field. 97
4.25 Fluid height along the channel length for a flow rate of 0.0318 kg/s at lower values of magnetic field. The B = 0 T case is plotted using the hydrodynamic equation and plotted in blue. The remaining cases are plotted using the surface normal solution derived in this chapter. 98
4.26 Fluid height change plotted against the Hartmann number for numerical and analytical solutions. 100

4.27 Fluid height change plotted against the Hartmann number for numerical and analytical solutions. 101
4.28 Fluid height change plotted against the Stuart Number for numerical and analytical solutions. 102

5.1 Comparison plot of average liquid metal height before and after introduction of a magnetic field, for transverse vs. surface normal magnetic field, showing a significantly larger height change in the surface normal magnetic field. . . 106
5.2 3D Plot of liquid metal height profiles collected over time, in the presence of a surface normal magnetic field. The magnetic field was turned on at 12 seconds and turned off at 20 seconds. 106
5.3 Streamwise fluid height across the channel for the analytical, numerical, and experimental cases. This data was collected at an inlet flow rate of 0.053 kg/s and at various magnetic field values between 0 T and 0.16 T. 107
5.4 Streamwise fluid height change across the channel for the analytical, numerical, and experimental cases. This data was collected at an inlet flow rate of 0.053 kg/s. 109
5.5 Comparison plot of analytical, numerical and experimental data height change values at various Hartmann Numbers collected at all three flow rate (0.0318 kg/s, 0.0424 kg/s, and 0.053 kg/s). 110
5.6 Comparison plot of analytical, numerical and experimental data height change values at various Hartmann Numbers collected for an inlet flow rate 0.0318 kg/s. 111
5.7 Comparison plot of analytical, numerical and experimental data height change values at various Hartmann Numbers collected for an inlet flow rate of 0.0424 kg/s. 112
5.8 Comparison plot of analytical, numerical and experimental data height change values at various Hartmann Numbers collected for an inlet flow rate of 0.053 kg/s. 112
5.9 Comparison plot of analytical, numerical and experimental data height change values at various Hartmann Numbers collected for an inlet flow rate of 0.053 kg/s. 113
5.10 Image of the flowing liquid lithium limiter in the EAST tokamak, showing lithium flowing in streams down the limiter. Image from (127). 118
5.11 Image (from (127) of the liquid lithium limiter in air after the experiments conducted at EAST, showing in red outline the areas where lithium did not wet. 119

5.12 Side by side comparison of the **a)** striated inlet design used on the 180 mm flow area width channel and **b)** staggered post inlet design used on the 100 mm flow area width channel. 121
5.13 Galinstan at 300 ml/min flowing down a) the 180 mm wide channel with striated inlet and b) the 100 mm wide channel with inlet posts, both at a 4°angle. 122
5.14 View of the updated galinstan flow spreader, with a 2mm gap between the flow spreader's lower edge and the surface of the main flow area 123
5.15 Comparison of a) galinstan flow without the inlet cover and b) galinstan flow with the inlet cover, both at 7°. 123
5.16 Image of three channel inserts made of 316 stainless steel with 1.27, 0.53, and 0.05 micron average surface roughness 125
5.17 Contact angle measurement parameters for a droplet of gallium (131) . . . 126
5.18 Example of contact angle measurement of liquid galinstan on a 0.05 micron average surface roughness stainless steel channel. 126
5.19 Sketch of oxidised (a) and unoxidised (b) galinstan on a substrate material (133) 127
5.20 Comparison plot of gallium based liquid metal contact angles on various metals. Data collected at OTI is represented by the black circles, all other data is sourced from literature review (131, 133, 134, 135). 128
5.21 Visualisation of convex vs. concave meniscus 128
5.22 Schematic of the divertor design and strike point position for the JET tokamak, from (137). 130
5.23 Galinstan streams flowing down stainless steel channels at a variety of surface roughness at channel angle 7°. 130
5.24 Galinstan streams flowing down stainless steel channels at a variety of surface roughness. Results from a fully horizontal channel are not shown, as this case led to full wetting at all surface roughnesses. 131
5.25 Galinstan flowing from the inlet hole down **a)** a flat channel and **b)** a channel at 1°, both at 0.05 micron surface roughness. 131

B.1 Schematic of the simplified model of solid metal melting in an ambient pool of liquid. 157
B.2 Melting curves for spherical galinstan particles of various initial diameter, with an initial temperature of -18°C, submerged in room temperature (25°C) galinstan. 159

B.3 **a)** Needle sizes available in the OTI lab. The measurements correspond to the needle inner diameters. **b)** An image of liquid metal being injected into the surfactant solution during the particle fabrication method. Image from (140) 160
B.4 Liquid galinstan droplets in SDS-water solution at room temperature 161
B.5 Results from particle fabrication trials. **A)** Liquid galinstan spheres of $<$ 1 mm diameter in solid SDS solution. **B)** Solid galinstan particles formed from droplets. **C)** A successful batch of solid spherical gallium particles, with diameters in the range 2-4 mm. **D)** Spherical gallium particles with 2 mm diameter. 162
B.6 Melting curves for spherical galinstan particles of various initial diameter, with an initial temperature of -18°C, submerged in 30°C water. 163
B.7 Setup of the model verification experiment. An initially solid galinstan particle is placed within the Y of a funnel which is submerged in a heated water bath. 164
B.8 Process and Instrumentation Diagram for a method to embed particles. The black lines show liquid galinstan lines and the blue lines have liquid galinstan and solid gallium. 164

List of Tables

2.1 Review of MHD Computational Model, LM stands for liquid metal 23

3.1 Comparison of key parameters for galinstan and lithium. 36
3.2 Oxford Liquid Metal Experiment Characteristics 37
3.3 Electromagnet Specifications 39
3.4 Magnetic Field Safety Guidelines 49

4.1 Model parameters input to ANSYS CFX 71
4.2 Benchmarking Results for Duct Flow Through Non Conductive Walls. . . . 76
4.3 Benchmarking Results for Duct Flow Through Non Conductive Wall with Correction Factor 78
4.4 Benchmarking Results for Duct Flow Through Conductive Hartmann Walls. 80
4.5 Benchmarking Results for Free Surface Flow Through Conductive Hartmann and Side Walls in the Presence of Transverse Magnetic Field 81
4.6 Benchmarking Results for Free Surface Flow Through Conductive Hartmann and Side Walls in the Presence of vertical magnetic field 84

5.1 Comparison of analytical, numerical, and experimental initial height values for developing, free surface flow with surface normal magnetic field 109
5.2 Results from Contact Angle Measurements 125

B.1 Parameters used in the model equations. Parameters without a subscript are always particle properties. 158
B.2 Physical constants used in the melting particle model to produce the melting curves shown in Figures B.2 and B.6. 159

Nomenclature

A	Magnetic Vector Potential [T.m]
a	Half trench width [m]
B	Magnetic Flux Density [T]
b	Half free surface height [m]
c	Conductivty Ratio [-]
C_{fmag}	Momentum source coefficient [$S.m^{-1}.T^2$]
d	Pipe diameter [m]
E	Electric field [$V.m^{-1}$]
F	Required duty cycle [-]
g	Gravity [$m.s^{-2}$]
h	Liquid metal film height [m]
I	Current [A]
j	Current Density [$A.m^{-2}$]
K	Discharge coefficient [-]
k	Thermal conductivity [$W.m^{-1}.K^{-1}$]
l_s	Solenoidal length [m]
L	Flow length scale [m]
m	Mass flow rate [$kg.s^{-1}$]
n	Number of turns [-]
P	Pressure [Pa]
p	Power [W]
Q	Flow Rate [$m^3.s^{-1}$]
q	Linear flow rate [$m^2.s$]
r	radius [m]
R_a	Roughness average [m]
R	Resistance [V.m^{-1}]
r	Radius [m]
S	Seebeck coefficient [$V.k^{-1}$]
T	Tensile strength [Pa]
t	Time [s]
U	Velocity [$m.s^{-1}$]
V	Voltage [V]
w	Trench width [m]
y, z	Cartesian Coordinate [-]
Greek Symbols	
α	Plate inclination angle [Degree]
χ	Conductivity Ratio [-]
ε	Aspect ratio [-]

μ	Dynamic viscosity $[Pa.s^{-1}]$
μ_0	Magnetic permeability in a classical vacuum $[kg.m.s^{-2}.A^{-2}]$
ν	Kinematic viscosity $[m.s^{-2}]$
φ	Electric Scalar Potential $[V]$
ρ	Density $[kg.m^{-3}]$
σ	Electrical Conductivity $[S.m^{-1}]$

Subscripts

analytical	Analytical
0	Initial
100	100 %
in	Inlet
f	Fluid
mag	Magnetic
numerical	numerical
out	Outlet
p	Piping
r	Reference
s	Solid
w	Wall

Abbreviations

CAD	Computer Aided Design
CCFE	Culham Centre for Fusion Energy
CFD	Computational Fluid Dynamics
CMOS	Complementary Metal Oxide Semiconductor
DAQ	Data Acquisition
DEMO	Demonstration Power Plant
EAST	Experimental Advanced Superconducting Tokamak
ELM	Edge Localised Mode
EP	Electric Potential
FEA	Finite Element Analysis
FEMM	Finite Element Method Magnetics
FLiLi	The Flowing Liquid Lithium Limiter
Ha	Hartmann Number
HIMAG	HyPerComp Incompressible MHD solver for Arbitrary Geometry
HTS	High Temperature Superconducting
IR	Infrared
LM	Liquid Metal
LMX	Liquid Metal Experiment
LTX	Lithium Tokamak Experiment
MCF	Magnetic Confinement Fusion
MI	Magnetic Induction
MHD	Magnetohydrodynamics
MTor	Magnetic Torus
MVP	Magnetic Vector Potential
OLME	Oxford Liquid Metal Experiment
OTI	Oxford Thermofluids Institute
PFC	Plasma Facing Component
PPPL	Princeton Plasma Physics Laboratory

Re	Reynolds number
Re_m	Magnetic Reynolds Number
SDG	Sustainable Development Goal
ST	Spherical Tokamak
TEMHD	Thermoelectric Magnetohydrodynamics
UKCA	UK Conformity Assessed
UV	Ultraviolet

Chapter 1

INTRODUCTION

This chapter provides an introduction to nuclear fusion reactors, chiefly focused on magnetic confinement fusion (MCF) in a tokamak. The challenge of developing plasma facing materials robust to high heat and particle fluxes is expanded in further detail and a case for liquid metal plasma facing components is made. Finally, the overall aims and achievements of this thesis are clearly defined.

1.1 Nuclear Fusion: An Overview

One of the greatest challenges of the 21st century is the development of sustainable energy sources that minimise carbon emissions and meet the growing energy demands of our world. In 2015, the United Nations published a list of 17 Sustainable Development Goals (SDGs) which should be pursued globally towards ”peace and prosperity for people and the planet, now and into the future” (1). SDG 7 and 13 communicate the need for low carbon energy sources that are widely accessible and affordable to promote global energy equity. As of 2018, the source of over 80% of the world's energy consumption was still attributed to fossil fuels (2), and currently the largest source of global greenhouse gas emissions are generated from fossil fuels (3). There have been significant advances in alternative fuel sources such as solar, hydroelectric, geothermal, nuclear fission and wind power, but all these sources have major drawbacks such as availability, efficiency and cost, that have prevented them from fully replacing fossil fuels (4). Nuclear fission reactors currently produce about one-third of the world's carbon free energy; however, nuclear fission power plants have been increasingly

decommissioned in the past 10 years due to costly accidents and increased safety regulations which have raised the costs of long term radioactive waste storage. A nuclear fusion reactor could produce over seven times more energy per nucleon than nuclear fission, but the fusion process requires more engineering expertise to carry out because of the high temperatures and particle densities required to initiate fusion (5). When compared to traditional chemical reactions involved in fossil fuel usage, nuclear fusion reactions produce over 1 million times more energy per mass of fuel (6). The benefits of fusion energy and proliferation include abundant fuel, reliable power production, minimal long-term radioactive waste, zero carbon emissions, and no potential for reactor meltdown. Deuterium and tritium are the optimal fuel sources for a nuclear fusion reactor this reaction has the highest fusion cross-section at the lowest temperatures, as is shown in Figure 1.1. Deuterium can be extracted from seawater and tritium currently is created in fission reactors and would eventually be bred in fusion reactors from lithium (7). Tritium breeding blankets are a complex but integral part of fusion reactors designed to run on deuterium and tritium fuel.

The collision of deuterium ($^{2}_{1}\mathrm{H}$) and tritium ($^{3}_{1}\mathrm{H}$) produces a neutron ($^{1}_{0}\mathrm{n}$), an alpha particle ($^{4}_{2}\mathrm{He}$), carrying 17.6 MeV of energy, as shown in Equation 1.1. This high energy neutron is then used to generate electricity by generating heat that is converted to electricity in a traditional thermal power plant.

$$^{2}_{1}\mathrm{H} + {}^{3}_{1}\mathrm{H} \longrightarrow {}^{4}_{2}\mathrm{He} + {}^{1}_{0}\mathrm{n} + 17.6\,\mathrm{Mev} \tag{1.1}$$

There are several criteria used to assess the success of a fusion reaction. The primary parameters for assessing plasma performance are plasma temperature, density and confinement time. The Lawson criterion was developed by J. D. Lawson in 1955 to define the combination of plasma density and confinement time required to reach breakeven. A modification of this also exists called the fusion triple product which incorporates plasma temperature. Breakeven occurs when the heat generated by the alpha particles and neutrons produced is equivalent to both bremsstrahlung, which is radiation emitted from the deflection of a charged particle by another charged particle, and thermal conduction losses (i.e. heating power) within the plasma (3).

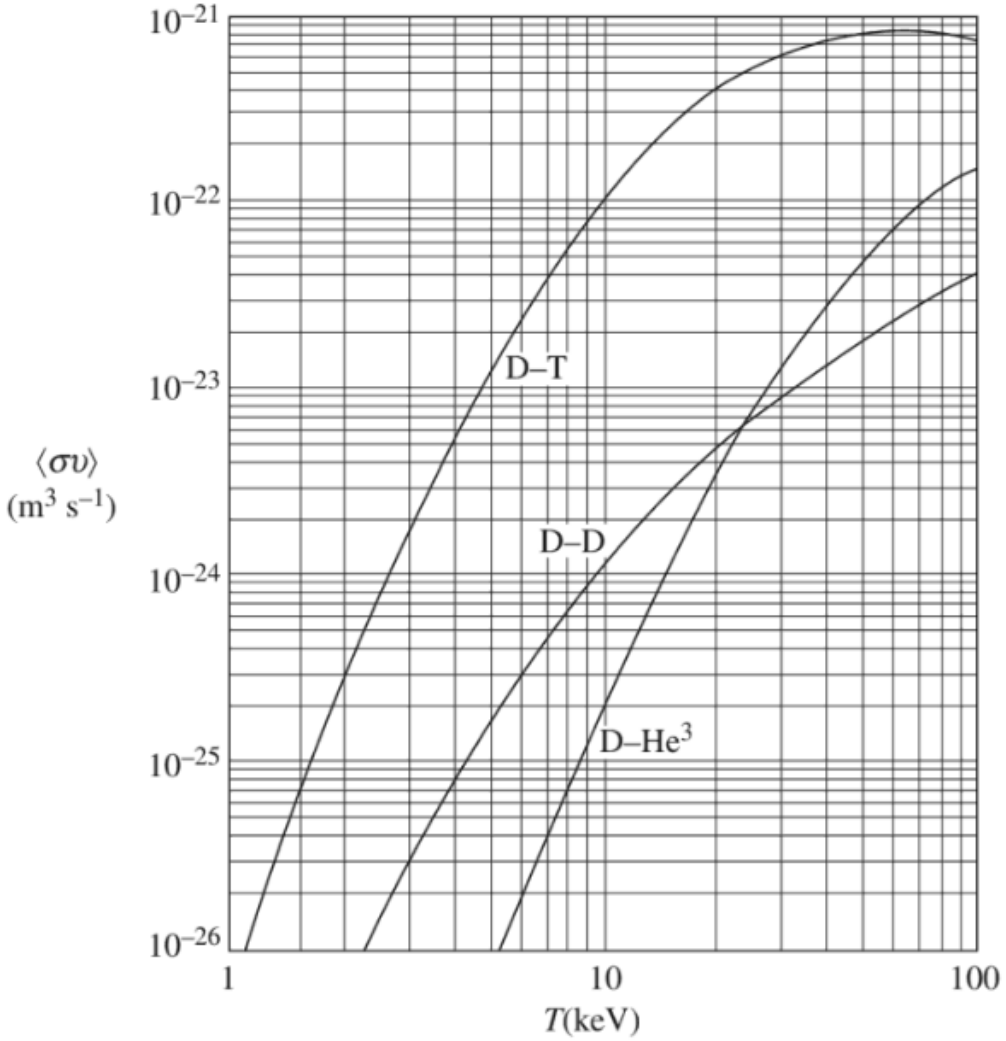


Figure 1.1: Plot of the reaction rate against the plasma temperature for three potential fusion fuel combinations where D is deuterium, T is tritium and He is helium (8).

For nuclear fusion reactors, there are two definitions of the gain factor. As a baseline, the gain factor is defined as the ratio of the net thermal power produced relative to the power required to heat the plasma, and a value greater than one is defined as the Lawson criterion. In a deuterium-tritium fusion reaction, 20% of energy produced serves to heat the plasma and the remaining 80% is stored as kinetic energy in neutrons which do not interact with the plasma due to their neutral charge. The kinetic energy in these neutrons heats heats the cooling fluid present in the walls of the device. Then electricity can be generated through the transfer of this heat in a turbine. External heating methods are required to initiate plasma temperatures at fusion relevant values. Furthermore, additional power inputs are required to run auxiliary reactor equipment (heaters, cryogenics, power supplies, pumps, etc.) and the conversion of neutron power to electricity is critically limited by the efficiency of the thermal energy conversion cycle. The engineering gain factor provides a more realistic measure of reactor energy production by describing the ratio of net electricity production relative to total energy input to the plasma and all auxiliary equipment. This engineering gain factor is above 10 for power production and above 20 to yield a profit.

MCF is currently the most technologically developed fusion approach, but there are many approaches currently under study at less developed stages including inertial confinement fusion, magnetized target fusion, and hybrid fission-fusion devices (9). In MCF, plasma is heated to temperatures in excess of 150 million degrees Celsius confined at a distance from the inner walls by a strong magnetic field. There are two mainstream configurations for magnetic confinement fusion reactors: the tokamak and the stellerator. Both configurations confine plasma using magnetic fields, however, different techniques are used to rotationally transform the magnetic field and prevent plasma drift (10). For tokamaks, the toroidal plasma electric current produces a poloidal magnetic field that twists the overall magnetic field. In the stellarator configuration, non-planar electromagnets and rotated magnetic flux surfaces are used to twist the magnetic field. Schematics of both designs are shown in Figure 1.2. The tokamak is currently the best understood configuration and will be the focus of this thesis.

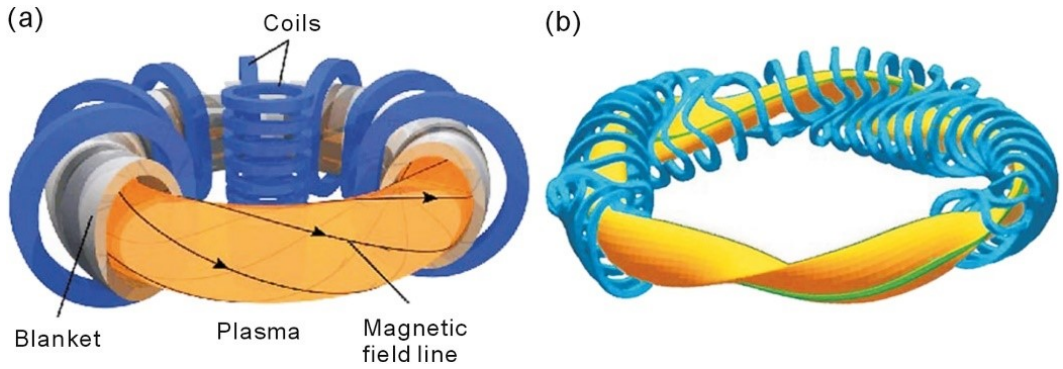


Figure 1.2: Comparison of a) tokamak and b) stellarator magnetic field configurations from (11)

1.1.1 Magnetic Field Orientations

In a tokamak, the toroidal magnetic field component is generated by the toroidal field coils, which contain high current that results in a magnetic field that charged particles are effectively tied to. However, since the toroidal field coils are arranged in a torus shape, there is a higher density of current in the centre of the tokamak than there is in the outer region. This leads to a 1/r magnetic field gradient where the region near the centre column, shown as the inner poloidal field coils in Figure 1.3, is the high field side and the region near the outer walls is the low field side. In the presence of a toroidal field and plasma current, the plasma would drift towards the sides of the tokamak. Poloidal field coils are used to control the direction of the plasma to prevent plasma drifting to the tokamak walls and quenching. Figure 1.3 shows the resultant toroidal and poloidal magnetic fields present in a typical fusion device.

In a tokamak, the toroidal magnetic field component is larger in magnitude than the poloidal magnetic field component. For example, (ITER) will have a toroidal field strength of 11.8 T and a poloidal field strength of 6 T (13). For a given plasma facing component, the toroidal and poloidal magnetic fields together impose a transverse, surface normal and streamwise magnetic field component which have varying effects on liquid metal flow. For example, looking at a limiter at the bottom of a tokamak, as shown in Figure 1.4, a flowing liquid metal surface would experience surface normal and streamwise components due to the poloidal magnetic field, and a transverse component due to the toroidal magnetic field. The surface normal and transverse components generate a magnetohydrodynamic drag force

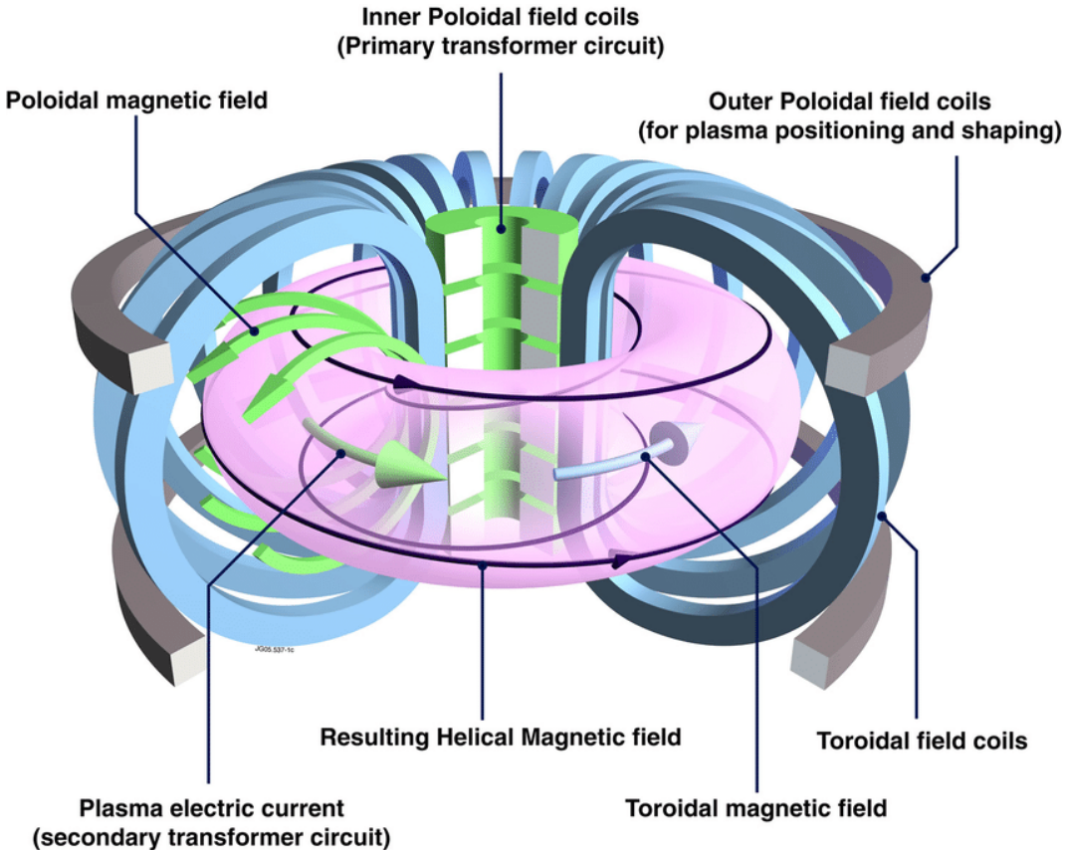


Figure 1.3: Diagram of magnetic field coils and resultant field orientations in a tokamak, from (12).

because they act perpendicular to the liquid metal flow, whilst the streamwise component has no effect. From the literature, it is known that the surface normal field generates a stronger MHD drag than the transverse field (14). So although the surface normal magnetic field will be smaller than the transverse magnetic field for a typical limiter configuration, its effects cannot be ignored.

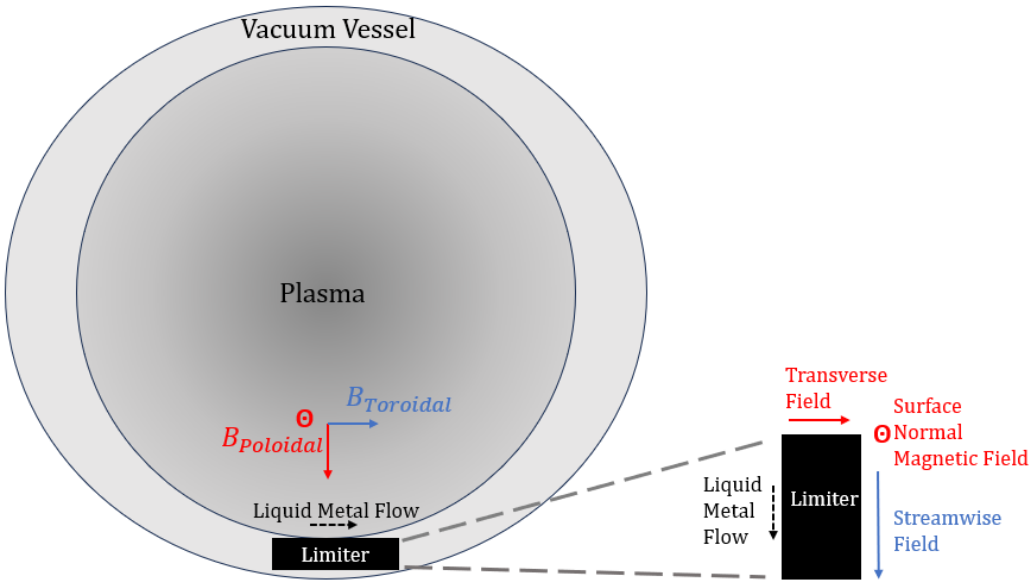


Figure 1.4: Diagram of a limiter in a tokamak, showing the poloidal (red) and toroidal field (blue) components. An additional frame of the limiter shows the direction of the streamwise, surface normal and transverse components, shown in red and blue for those contributed by the poloidal and toroidal fields in this scene, respectively.

1.1.2 Fusion is a Global Initiative

A 2022 survey by the International Atomic Energy Agency found that there are over 40 tokamaks around the world that are currently in operation or under construction (15). ITER, Latin for "The Way," is an international, experimental tokamak currently under construction in France that is projected to be the first fusion device to reach a gain factor greater than 10. Following ITER, there are research efforts towards a full nuclear fusion Demonstration Power Plant (DEMO). The fusion reactor conditions expected in a DEMO exceed current research facility capabilities, so relevant facilities and numerical models are currently being developed to aid in the necessary scaling efforts (16).

The novelty of nuclear fusion technology translates to large research and development

costs that are driven by raw material costs and lack of standardisation of essential technologies such as large vacuum vessels and high temperature superconducting (HTS) magnets (3). The cost to build ITER is projected as €20 billion, primarily due to the sheer size of the device. Reactor size is a key cost driver as larger reactors are significantly more expensive to build. This has motivated increased research and development on the production of smaller scale fusion reactors which can be produced in a factory and shipped to site. Smaller fusion devices come with several challenges such as reduced power output, potentially increased heat flux loading on internal walls, and reduction in confinement time which are all currently under study on numerous smaller scale fusion reactors around the world. With the more recent development of HTS to aid in creating larger magnetic fields in smaller devices, challenges in the manufacturing and cost of HTS cables have been highlighted (17).

Tokamak Energy is a nuclear fusion based company based in the United Kingdom that seeks to achieve sustainable fusion energy through the development of a low aspect ratio, spherical tokamak using HTS magnets. Employing an aspect ratio (major plasma torus radius to minor plasma torus radius) of less than 2 increases plasma stability and confinement time (18). In 2022, Tokamak Energy achieved a major milestone for the spherical tokamak with the achievement of plasma temperature in excess of 100 million Kelvin in their ST40 device, a significant step towards approaching commercial fusion. The challenge of designing a fusion device that can handle high heat flux loads remains a key area of research for Tokamak Energy and sparked the inspiration for the onset of the work carried out in this thesis.

In recent years, nuclear fusion has gained increasing support from governments around the world to aid in the quickening of fusion reactor development, notably in South Korea, Japan, China, the United States, the European Union, and the United Kingdom (3). The sheer scale of research and development work required to reach net energy gain has made fusion research a historically international endeavour, as can be shown in Figure 1.5. However, much of fusion research occurs in high income countries, and private fusion activity remains constrained to a handful of countries (see Figure 1.6). As fusion energy continues to develop, concerted effort must be made to ensure those that benefit from fusion technology are not only those who can afford to participate in its development. The impending energy crisis is

a global concern that will require collaborative efforts from thought leaders across the globe. Reaching SDG 7's aim of developing energy solutions that are accessible around the world means that effort must be made to distribute fusion energy worldwide in aims of creating a more equitable global energy economy

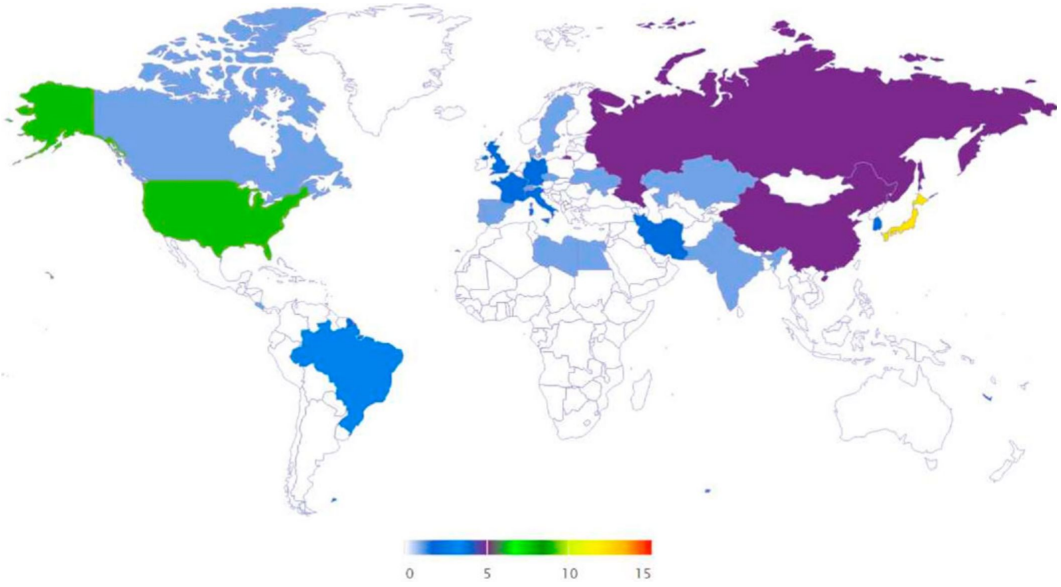


Figure 1.5: Map of public institution involvement in nuclear fusion research, from (3). The colour map represent the number of institutions in each country.

1.1.3 The Case for Liquid Metal Plasma Facing Components

In 2012, the EUROfusion consortium published a list of the seven current challenges to fusion commercialization (16). The development of resilient heat exhausts systems is listed as one of the challenges. In fact, a 2020 study of plasma disruption sources on Experimental Advanced Superconducting Tokamak (EAST) attributed 38% of plasma disruptions to plasma-wall interactions, and predicts that this percentage will increase as tokamaks reach higher power outputs and longer shot times, thus highlighting the need for more robust materials plasma facing components (PFCs) (19).

The plasma facing components of a fusion reactor include: 1) the first wall, which is the inner wall of the reactor vacuum vessel that contains the plasma, 2) limiters, or armour, which are placed between the first wall and the plasma as physical bounds for the plasma, and 3) divertors, which are often placed at the top and/or bottom of the machine to exhaust

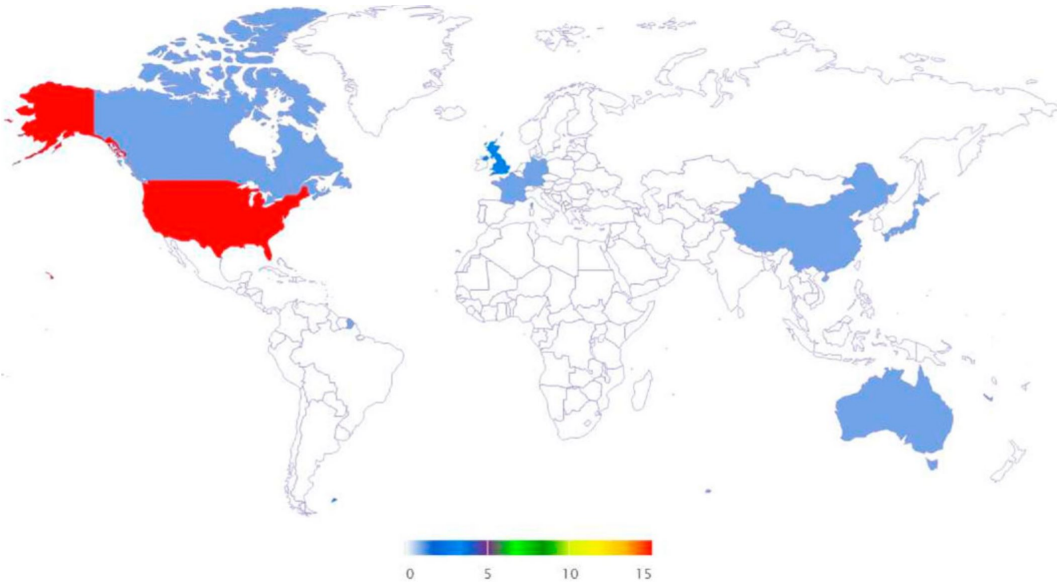


Figure 1.6: Map of private company involvement in commercialised fusion development (excluding work on DEMO), from (3). The colour map represent the number of institutions in each country.

plasma waste. These three components, and their effect on the plasma shape, are illustrated in Figure 1.7 .

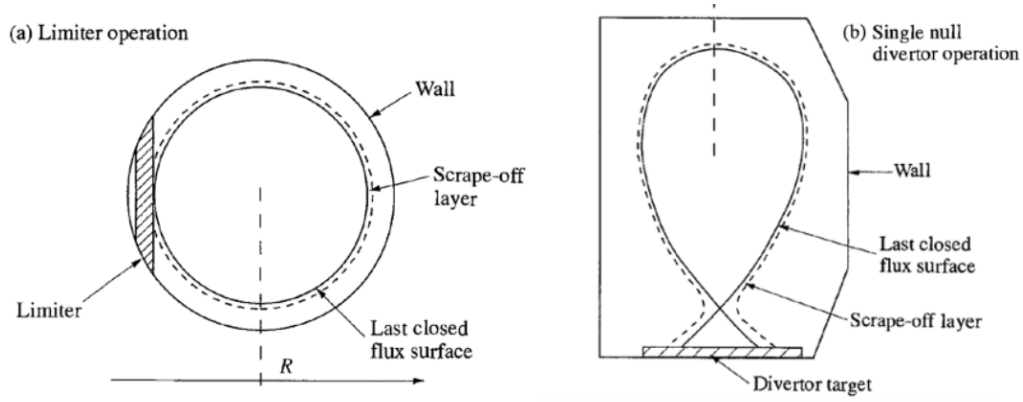


Figure 1.7: Schematic of the plasma facing components in a fusion device showing a limited plasma (a) and a diverted plasma (b) from (20).

In order to build compact and/or high power fusion devices, large plasma currents are required to sustainably confine the plasma over a long thermal confinement time required to reach the Lawson criterion. As the reactor current increases, the loads experienced by the divertor increase as well due to the narrowing of the plasma scrape off layer, which is the portion of the plasma where the magnetic field lines begin or end on a surface, which guides ”cold” plasma towards the divertor surface (21). The design of future, DEMO-like fusion

reactors is limited by present technology surrounding PFC loading capacities (22).

Current heat exhaust systems utilise solid metal composites as the plasma facing materials (23, 24). These surfaces suffer from significant surface damage from neutron bombardment, high incident heat fluxes, and hydrogen and helium interactions caused by plasma wall interactions, so they would need to be replaced often in a steady state nuclear fusion device (25). This reduces the time the reactor is available to produce energy to the grid, which impacts the financial viability of this technology. It is estimated that a DEMO size fusion device would experience quasi-stationary heat flux loads of up to 20 MW/m^2, with occasional short transient loads on the order of gigawatts per m^2 in the presence of edge localised modes (ELMs), which are a type of plasma instability occurring in the plasma edge (25). ELMs naturally occur during tokamak operation but their frequency can be increased through methods of gas puffing and pellet injection technologies to reduce their peak power density.

Liquid metals have been investigated as a possible plasma facing material to be located between the solid PFC and the plasma. A liquid metal PFC could serve to protect the underlying solid metal from surface degradation and transmutation, reduce the magnitude of mechanical and thermal stresses experienced by solid PFC, and potentially reduce incident heat flux loads (26). This can lead to increased reactor lifetime, reduced reactor maintenance, and a reduction in plasma recycling. Plasma recycling occurs when ”cold” plasma that has drifted towards the PFC is not efficiently removed from the inner vessel but instead re-enters the central, hot plasma region, further cooling surrounding plasma (27). Liquid lithium can act to more efficiently remove ”cold” plasma to boost overall plasma temperature by pumping away reactive and inert gases through co-deposition (28, 29). Liquid metals also provide a surface that can regenerate itself despite disruptions, which avoids permanent damage from the plasma.

These novel surfaces come with a variety of challenges such as surface dryout, droplet formation, diagnostic window coating, safety concerns in the event of a loss of vacuum accident and the complication of magnetohydrodynamic effects on the flow. In a nuclear fusion reactor, liquid metals are subject to large magnetic fields and currents that have a signific-

ant impact on the flow behaviour of the liquid metal. This magnetohydrodynamic (MHD) flow of liquid metal in fusion environments has been studied theoretically and much experimental and numerical work is currently underway to validate these theories. Thermoelectric magnetohydrodynamics (TEMHD) is another closely related phenomena involving the generation of electric currents due to temperature gradients along the interface of two metals with different Seebeck Coefficient values. TEMHD is not a focus of this research, but efforts are made to ensure the work done can be easily expanded to include TEMHD effects in the future, and these efforts are described throughout the thesis.

An overview of liquid metal PFC experiments is provided in the literature review. Those experiments point to the compatibility and viability of liquid metal PFC's. However, they also highlight a key vulnerability, which is the lack quantitative measurements of the impacts of magnetic field and plasma on the liquid metal flow. Such quantitative measurements are difficult to pursue in a fusion device due to many limitations such as restrictive geometric constraints, lack of visual access, magnetic interference with measurement equipment, and general challenges in liquid metal flow characteristic measurements. The lack of even liquid metal spreading across plasma facing components has been studied qualitatively (30), but quantitatively there is little information about the height or velocity of the flow and how that was impacted by the magnetic field or plasma. Liquid metal surfaces are highly reflective which makes most noninvasive flow measurement techniques difficult. Due to the difficulty of in-situ measurements, liquid metal bench scale experiments are of prime importance to aid in understanding of the quantitative influence of fusion relevant parameters on fluid flow.

The effects of magnetic fields on flowing liquid metal surfaces are currently being studied analytically, numerically, and experimentally. For example, analytical theory suggests the surface normal magnetic field will have the primary effect on liquid metal flow, however, this effect has not yet been experimentally quantified for free surface flow because access to the free surface to make measurements is typically restricted by the magnet placement (14). The quantification of this effect, along with additional factors such as flow angle, velocity, and channel geometry, will be invaluable for future design of liquid metal plasma facing components.

The work described in this thesis describes the development of a new experimental facility built at the University of Oxford, the Oxford Liquid Metal Experiment (OLME), with the novel capability of quantitatively measuring relative impacts of magnetic field orientation and strength on liquid metal flow parameters. Analytical and numerical models describing the projected behaviour of liquid metal on the OLME were developed alongside the construction of the OLME, to facilitate comparison of experimental results with established liquid metal MHD theory.

1.2 Research Aims

The main aim of this thesis was to develop an experimental facility to quantitatively measure the impact of surface normal magnetic field on liquid metal height, alongside appropriate analytical and numerical models for use in future extrapolation. The following objectives were formulated to reach this goal.

1. To undertake a literature review of relevant experimental, analytical, and numerical work

2. To adjust current analytical models of developing, free surface MHD flow to incorporate surface normal magnetic field effects

3. To develop and validate a numerical model of developing liquid metal flow in the presence of a surface normal magnetic field using the commercial software ANSYS CFX[1]

4. To design and build an experiment, the Oxford Liquid Metal Experiment (OLME), to allow for novel experimental measurements of liquid metal height changes in the presence of a surface normal magnetic field

5. To experimentally measure the change in liquid metal height in response to a surface normal field at various flow rates, and compare these results with analytical and numerical predictions

[1] www.ansys.com

1.3 Thesis Contributions

The main scientific contributions of the current research are summarised as follows;

1. The present work has developed a novel experimental facility at the University of Oxford for studying liquid metal MHD behaviour, referred to as the Oxford Liquid Metal Experiment (OLME). The facility was composed of a liquid metal loop, a bespoke electromagnet, and a laser triangulation system to allow for safe and efficient quantitative measurements in both surface normal and transverse magnetic fields. The experimental set up was designed to allow for ease of iteration in channel design and magnetic field composition for future research.

2. The work has yielded an analytical solution and accompanying numerical model of developing liquid metal flow in a surface normal magnetic fields for a low aspect ratio geometry. This model will be useful in the future design of PFCs for rapid determination of suitable flow parameters to yield desired film thicknesses.

3. This thesis provided a novel comparison of analytical, numerical, and experimental data quantifying the impacts of a surface normal magnetic field on free surface liquid metal height. This was the first reported quantitative measurement of free surface, liquid metal height response to a surface normal magnetic field. Challenges incurred in the measurement of free surface liquid metal height were explored and the impact of surface roughness and channel geometry was measured to improve future free surface liquid metal PFC experimentation.

4. The present work has yielded two conference presentations: one oral presentation at the 2022 International Symposium on Liquid Metal Applications for Fusion Applications at Chubu University in Japan and one poster at the 2019 Symposium on Fusion Engineering in Jacksonville, Florida. Additionally, this work has yielded one invited seminar at the University of Michigan department of Nuclear Engineering in 2021.

This thesis has laid the groundwork for a much needed bridge between analytical, numerical and experimental work that have mostly been studied in silos to date. This work

has developed an experimental basis for understanding relative impacts of magnetic field orientation on liquid metal flow, and has suggested potential improvements to analytical and numerical methods to better align with experimental phenomena. Throughout this research process, several additional questions arose such as how to measure liquid metal velocity. Progress made towards answering these questions was documented at the end of each chapter in the ”Looking to the Future” section to aid in future research efforts. Overall, this work produces several tools that will aid in the development of liquid metal PFCs in the near future.

1.4 Thesis Structure

This thesis is composed of seven chapters. A brief description of each chapter is listen here:

Chapter 1 Introduces the overall research topic within the context of nuclear fusion plasma facing component design. This chapter identifies the relevant literature gaps and outlines the objects and contributions of this work.

Chapter 2 Presents a thorough literature review of existing work related to this topic and describes the need for the work presented in this thesis.

Chapter 3 Describes the design and construction of the Oxford Liquid Metal Experiment (OLME) built by the author to measure liquid metal behaviour in MHD relevant conditions. Also, suggestions for future modifications of the OLME to measure velocity and incorporate TEMHD effects are included.

Chapter 4 Presents the development of a numerical model of free surface, developing MHD flow for a low aspect ratio geometry, This model is validated firstly against established fully developed analytical solution, and then against a novel developing flow analytical solution derived by the author.

Chapter 5 Presents a comparison of analytical, numerical, and experimental MHD height change in response to surface normal magnetic field at various Hartmann numbers. Contact

angle measurements made for galinstan at OTI are also included, alongside alternative channel designs employed to study wetting.

Chapter 6 Concludes the work contained in this thesis and evaluates the products of this work in relation to the overall thesis aims.

Chapter 7 Recommendations are made for the continuation of this work in the analytical, numerical and experimental realms.

Chapter 2

LITERATURE REVIEW OF LIQUID METAL PLASMA FACING COMPONENTS

2.1 Overview

This chapter provides a literature survey of relevant publications relating to the work carried out for this thesis. Section 2.2 briefly reviews the history of magnetohydrodynamics (MHD) and provides an introduction to plasma facing components (PFCs). Section 2.3 details analytical theory developed surrounding MHD in liquid metals. Section 2.4 delves into numerical modelling of liquid metal MHD. Finally, Section 2.5 describes the current status of PFC technology and experimental work relating to liquid metal PFC development.

2.2 Magnetohydrodynamics

In 1942, MHD theory was formally developed by Hannes Alfv́en in an effort to describe observed astrophysical phenomena (24). Magnetohydrodynamics describes the flow of an electrically conductive fluid through a magnetic field. For decades, MHD applications remained confined to plasma physics and astronomical research. In 1970, Christofilos from the Lawrence Livermore National laboratory proposed the concept of using liquid lithium as

a replacement material for the niobium plasma facing walls for a field reversed fusion reactor to reduce material irradiation and overall reactor costs (23). The proposed wall would be 75 cm thick and move at about 30 m/s. In 1981, Moir proposed a liquid metal wall design for a magnetic confinement fusion device (31).

MHD is known to have two effects:

1. The induction of a magnetic field caused by currents induced in the electrically conductive fluids. This induced magnetic field perturbs the original, imposed magnetic field.

2. The development of an electromagnetic force caused by interactions of the magnetic field and currents, that alters the fluid motion.

The magnetic Reynolds number, Re_m, shown as Equation 2.1, compares the effects of magnetic field induction and diffusion. In this equation, μ_0 is the vacuum permeability constant $\left(1.26 \times 10^{-6} \frac{N}{A^2}\right)$, σ is the fluid electrical conductivity, U is fluid velocity, and L is the length scale along the field direction. To determine the magnetic Reynolds number relevant in this thesis, values of $\sigma = 3.46 \times 10^6 S/m$ and $U = 40mm/s$ were used, based on the experimental set up described in Chapter 3. The length scale was fluid height ($\approx 5mm$) for surface normal field and fluid width ($\approx 25mm$) for transverse magnetic field. A magnetic Reynolds number much less than one indicates that induced magnetic field has a negligible effect on the flow of the liquid metal. For the work discussed in this thesis, the magnetic Reynolds numbers were on the order of 10^{-3} and 10^{-5} for the transverse and surface normal field configurations, respectively, which allowed us to make the assumption that any induced magnetic fields caused by the induced currents formed in the flowing liquid metal could be ignored (32). This allowed for simplifications in the MHD equations as the imposed magnetic field was the sole field of interest.

$$Re_m = \mu_0 \sigma U L \tag{2.1}$$

The electromagnetic force that occurs in MHD is described as the Lorentz force, $\vec{F}_{MHD}$, given by the Equation 2.2, where $\vec{j}$ represents current density and $\vec{B}$ represents magnetic

field. The current density is defined by Ohm's Law (see Equation 2.3), were $\vec{E}$ represents electric field.

$$\vec{F}_{MHD} = \vec{j} \times \vec{B} \tag{2.2}$$

$$j = \sigma(\vec{E} + \vec{U} \times \vec{B}) \tag{2.3}$$

For the cases explored in this thesis, there is no external electric field, so the current can be simplified to Equation 2.4, where the fluid current is the cross product of fluid velocity and the external magnetic field. Magnetic field components that act perpendicular to the fluid flow generate MHD drag which tends to decelerate and stabilise liquid metal flow (33, 34, 35). The streamwise field component has no impact on liquid metal flow because the magnetic field is parallel to the fluid velocity.

$$\vec{j} = \sigma(\vec{U} \times \vec{B}) \tag{2.4}$$

In the presence of a temperature gradient perpendicular to the magnetic field and flow directions, a thermoelectric current is generated. This phenomena is known as thermoelectric magnetohydrodynamics (TEMHD). This adds a third term to Ohm's law, as shown in Equation 2.5, where S is the seebeck coefficient and ∇T is the temperature gradient. The negative sign signifies that thermoelectric current is generated in the direction opposite to the MHD current. TEMHD effects are not the focus of this work, but they are mentioned in literature survey, as well as in the later parts of thesis thesis to describe proposed future work.

$$\vec{j}_{TEMHD} = -\sigma \Delta S \nabla T \tag{2.5}$$

The use of flowing liquid metal surfaces is proposed for future fusion reactor PFCs, such as the divertor and limiter, to reduce the effects of thermal and mechanical stresses on the underlying solid substrate surfaces and minimise plasma wall interactions while im-

proving plasma performance (36). Many designs of liquid metal PFCs have developed over time. These can be broadly categorised into three groups: capillary porous structures, vapour shielding, and flowing liquid metal systems (37). Capillary porous structures exploit strong capillary forces in porous mesh grids to wick liquid metal to the plasma facing surface. Vapour shielding involves generating a controlled vapour cloud in a baffled region between the plasma and wall material that acts to shield PFC surfaces from incident particle flux. Flowing liquid metal systems involve continually refreshing PFC surfaces with liquid metal coatings through a recirculation system. The remainder of this thesis will focus on flowing liquid metal technologies.

There are different flow regimes which are under investigation. Broadly, these relate to liquid metal film thickness and speed. Thin films and thick films are generally regarded as less than 2 cm and greater than 40 cm, respectively (23). Thick films have the advantage of greater heat flux removal. Thin films require less fluid inventory and pumping power, and are less prone to surface ejections which can cause plasma disruptions. Fast flows remove incident heat fluxes quickly, which leads to lower liquid free surface temperatures. Slower flows, particularly laminar flows, produce smoother films that are easier to control and require less pumping power (38).

The remainder of this chapter comprises a literature survey of analytical, numerical and experimental work relating to free surface flow of mainly thin film liquid metals for fusion applications. Literature gaps are highlighted and the positioning of the research completed by the author in the overall landscape is established.

2.3 Literature Review of Analytical Analyses of Liquid Metal Free Surface MHD

In 1953, Shercliff produced a study of fully developed, conductive fluid flow in insulating pipes under transverse magnetic fields, building off of the work of Hartmann and Alfv́en earlier in the century (32, 39). This analytical solution calculated the velocity profile, induced currents, and induced fields generated by conductive fluids, and confirmed that strong

magnetic fields generate a uniform velocity in the core region and boundary layers on the side walls. This model was expanded to incorporate pipes of any symmetrical shape, and was successfully experimentally validated by comparing MHD pressure gradients for certain flow rates in both square and circular pipes

In 1961, Chang and Lundgren expanded upon the work of Shercliff and Hunt to incorporate the effects of conducting walls (40). This study explores conductive fluid flow through a rectangular duct where the walls parallel to the magnetic field are infinitely far away and the case of flow through rectangular duct with all infinitely conductive walls. The main conclusion from this work was the inversely proportional relationship between wall conductivity and average velocity.

In 1964, Hunt explored two additional conductive wall cases: (i) walls perpendicular to the magnetic field with infinite conductivity and thin walls parallel to the magnetic field with arbitrary conductivity and (ii) thin walls perpendicular to the magnetic field with arbitrary conductivity and walls parallel to the magnetic field with zero conductivity (41). He characterised the nature of the boundary layers and the stability of these layers in relation to Hartmann and Reynolds numbers.

In 1986, Miyazaki generated a theoretical approximation of MHD pressure gradient in a conductive rectangular duct with a fully developed flowing conductive fluid (42). This theoretical prediction showed strong agreement with experimental results for both uniform and non uniform magnetic fields. This approximation provided a useful method for readily predicting MHD pressure drops.

In 1992, the impact of a transverse magnetic field on free surface, fully developed, conductive fluid flow was explored by Shishko (43). This paper derived a formulation for the free surface, fully developed flow of conductive fluid in the cases of: (i) insulated side walls and conductive substrate, and (ii) conductive side walls and substrate. This was one of the first studies to successfully account for free surface flow rather than duct flow.

The effect of surface normal magnetic field on free surface liquid metal flow was theoretically approximated by Platacis (44). This formula predicted liquid metal height as a function of channel angle, flow rate, and surface normal magnetic field. An attempt was

made to experimentally validate this model, though no quantitative data was secured.

In 2020, Lunz derived a solution for 3D, free surface, thin film flow across a simplified tokamak divertor geometry (38). The model incorporated gravitational, thermocapillary and thermoelectric forces, as well as thermal and mechanical plasma effects . This study found the poloidal magnetic field effects to be dominant, causing a significant MHD drag and decelerating the lithium flow. A sweeping plasma strike point was imposed on the fluid surface to explore the impact of transient events on fluid stability, which is important in relation to dry out and droplet ejection. This study provided essential theory supporting the non steady flow behaviour of conductive fluids.

Most recently, Sun et. al. developed an analytical approximation for developing free surface flow across a flat surface in the presence of a transverse magnetic field (45). This solution was compared with experimental results and showed strong agreement in the trends predicted. This laid the groundwork for the analytical derivations of developing flow produced in this thesis, where the effect of surface normal magnetic fields were incorporated into the analytical solution.

2.4 Literature Review of Numerical Modelling of Liquid Metal Free Surface MHD

The numerical modelling of liquid metal MHD flow in fusion relevant magnetic fields has improved significantly over the past two decades. In 2004, the MHD code HyPerComp Incompressible MHD solver for Arbitrary Geometry (HIMAG) was developed at the University of California, Los Angeles to predict qualitative trends for free surface, liquid metal flowing in complex geometries under high magnetic fields (46). More recently, commercial and open source codes such as ANSYS, COMSOL, and OpenFOAM have been modified to allow for more widespread and standardized liquid metal MHD modelling. Table 2.1 contains a summary of liquid metal MHD numerical models developed across each platform and their applications. Most liquid metal MHD codes have been developed for duct flow in the blanket region of a fusion device, which is the section following the vacuum vessel wall

where coolant flows, or for metallurgy purposes. More recently, free surface liquid metal modelling has been considered. ANSYS is currently the most widely used commercial code for liquid metal MHD modelling.

Table 2.1: Review of MHD Computational Model, LM stands for liquid metal

CFD Programme	**Application**	**Purpose**	**Year**	**Institution**
HEIGHTS	First Wall	2D, free surface flow, Hydrogen/Helium entrapment	2001	Argonne, USA (47)
HIMAG	Liquid metal (LM) free surface	3D, complex flow geometries, modelling fusion magnetic fields and heat effects	2004	University of California, Los Angeles (46)
OpenFOAM	LM Blanket	2D, coupling of MHD and Heat transfer	2008	Universitat Politècnica de Catalunya (48)
MTC-H 1.0	LM Blanket	3D, duct flow	2010	Institute of Plasma Physics, Chinese Academy of Sciences (49)
COMSOL	Metallurgy	3D, LM levitation	2010	University of Greenwich (50)
ANSYS CFX	LM Blanket	3D, duct flow, Korean Test Blanket Module Geometry	2012	Pochang University of Science and Technology, Korea (51)
ANSYS FLUENT	LM Blanket	3D, duct flow, 4T magnetic field, flexible geometry	2012	Institute of Plasma Research, India (52)
FLUIDYN MP	LM Blanket	3D, U Shaped Duct, neutronic heat load	2012	Institute of Plasma Research (53)
ANSYS CFX	Metallurgy	3D, LM Levitation	2012	Leibniz University of Hanover (54)
ANSYS CFX	Metallurgy	3D, bubble-driven LM	2013	Helmholtz-Zentrum Dresden-Rossendor (55)
OpenFOAM	LM Blanket	3D, Uniform and non uniform magnetic field, round and rectangular duct flow	2015	University of Science and Technology of China (56)
ANSYS CFX	LM Blanket	3D Duct Flow, high magnetic field	2015	Princeton Plasma Physics Laboratory (57, 58)
COMSOL	LM Blanket	3D, duct flow	2017	University of California, Los Angeles (59)
ANSYS CFX	LM Blanket	3D, U shaped duct, uniform transverse magnetic field	2017	Kyung Hee University (60)
COMSOL	LM Blanket	3D, duct flow, transverse magnetic field	2018	Institute of Plasma Research, India (61)
COMSOL	LM free surface	3D, TEMHD flow	2017	University of Illinois, Urbana Champaign (62)
ANSYS CFX and OpenFOAM	LM free surface	3D, developing flow, transverse magnetic field	2023	Princeton Plasma Physics Laboratory (45)

ANSYS has two codes for numerical fluid dynamics: CFX and Fluent. Both codes utilize different physical approaches to solving MHD systems. CFX uses a magnetic induction approach and Fluent uses a magnetic vector potential approach. CFX has been more widely validated for MHD flows at low magnetic Reynolds numbers, so CFX was chosen for the simulations described in this thesis (51, 57).

The use of ANSYS CFX for fully developed blanket calculations was validated experimentally in 2012 by Kim et. al. using MHD pressure loss measurements collected on the Korean Test Blanket Module as well as with existing analytical solutions (51). In this paper, CFX's built in electromagnetic module produced MHD pressure drop values that showed good agreement with both experimental data and analytical solutions, without the need for modifications to the module.

Khodak from Princeton Plasma Physics Laboratory (PPPL) further validated the use of the magnetic induction method in ANSYS CFX for MHD duct flow and suggested the addition of source coefficients to the momentum and magnetic field equations to improve the numerical accuracy accuracy of the code (57, 63). Further discussion of these coefficients are describe in Chapter 4. Khodak validated ANYS CFX for both simple and divertor relevant geometries, and for Hartmann numbers up to 15,000 to illustrate the relevance of the model at fusion relevant conditions (58). More recently, Khodak studied the free surface capabilities of the CFX solver and proposed adaptations to the momentum equation to account for the impacts of the Lorentz force and surface tension (64, 65). In these studies, Khodak performed a stability analysis of the free surface in response to small perturbations, to explore the impact of incident plasma strikes on free surface stability.

One current challenge remains the experimental validation of free surface, MHD numerical simulations. This challenge was recently tackled by Sun in 2023, where 3D numerical simulations of developing liquid metal flow on the Liquid Metal Experiment at PPPL (described in Section 2.5.2.2) were created in ANSYS CFX and OpenFOAM, and compared directly to experimental data collected (45). Figure 2.1 shows the experimental results overlaid with the numerical solution, showing a strong agreement in the predicted trends including the presence of liquid metal "pileup" near the inlet. The analytical and numerical modelling de-

tailed in this thesis was built from this work by Sun, which was modified here to incorporate a surface normal rather than transverse magnetic field.

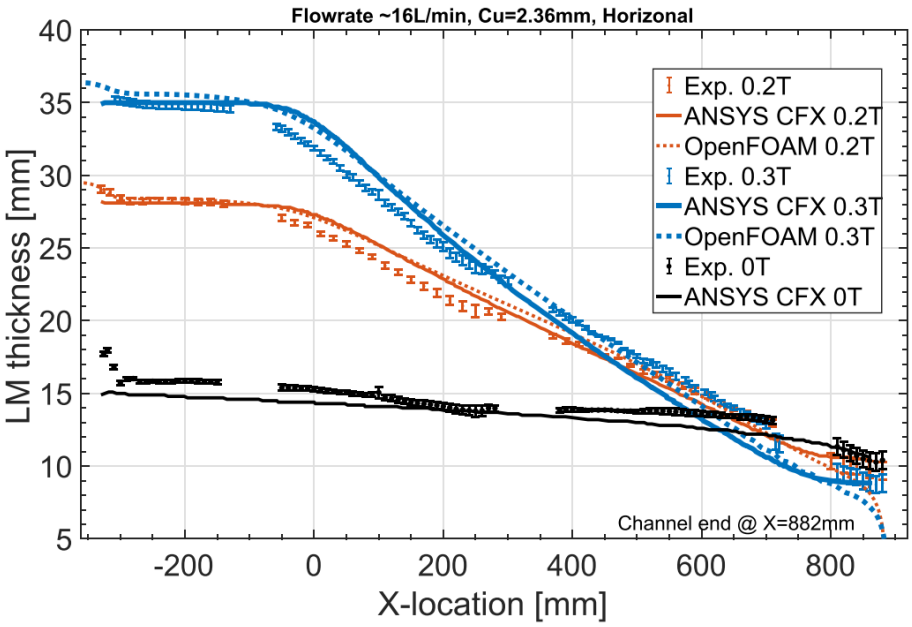


Figure 2.1: Plot of numerical and experimental results produced on the Liquid Metal Experiment (LMX) at PPPL for galinstan flow across a flat channel in the presence of 0 (black lines), 0.2 T (orange lines), and 0.3 T (blue lines) transverse magnetic fields. (Figure 5 from (45))

Much work remains in the area of numerical simulations of liquid metal flow, primarily in the incorporation of surface tension effects and thermoelectric effects. Researchers at the University of Illinois at Urbana Champaign (UIUC) are developing a 3D, free surface, numerical model of thermoelectric MHD flow in COMSOL and experimental validations are underway (62, 66).

2.5 Literature Review of Experimental Liquid Metal Free Surface MHD

2.5.1 Solid Plasma Facing Components

Currently tungsten is the most promising plasma facing material due to its high melting point and thermal conductivity. However tungsten forms a ”fuzz” in the presence of he-

lium irradiation which can negatively impact the plasma (67). Tungsten also suffers from recrystallisation at temperatures projected for DEMO operation in both the quasistationary heat flux and transient ELM heat flux ranges and transmutation of tungsten to rhenium and osmium can significantly alter the material properties such as ductility and embrittlement temperature (68, 69). Alternatively, new tungsten grades are under development to improve material performance in fusion relevant conditions (70). Figure 2.2 shows cracks formed in a tungsten monoblock after 300 thermal cycles at 20 $\frac{MW}{m^2}$. The most robust design for solid plasma facing materials is the monoblock design which involves rectangular blocks of the selected plasma facing material with a cylindrical hole thorough the middle for coolant flow. Though significant progress has been made in the development of solid plasma facing components; no solution has been determined that can withstand projected steady state and transient mechanical, thermal, neutron and particle loads required for net power gain without frequent replacement.

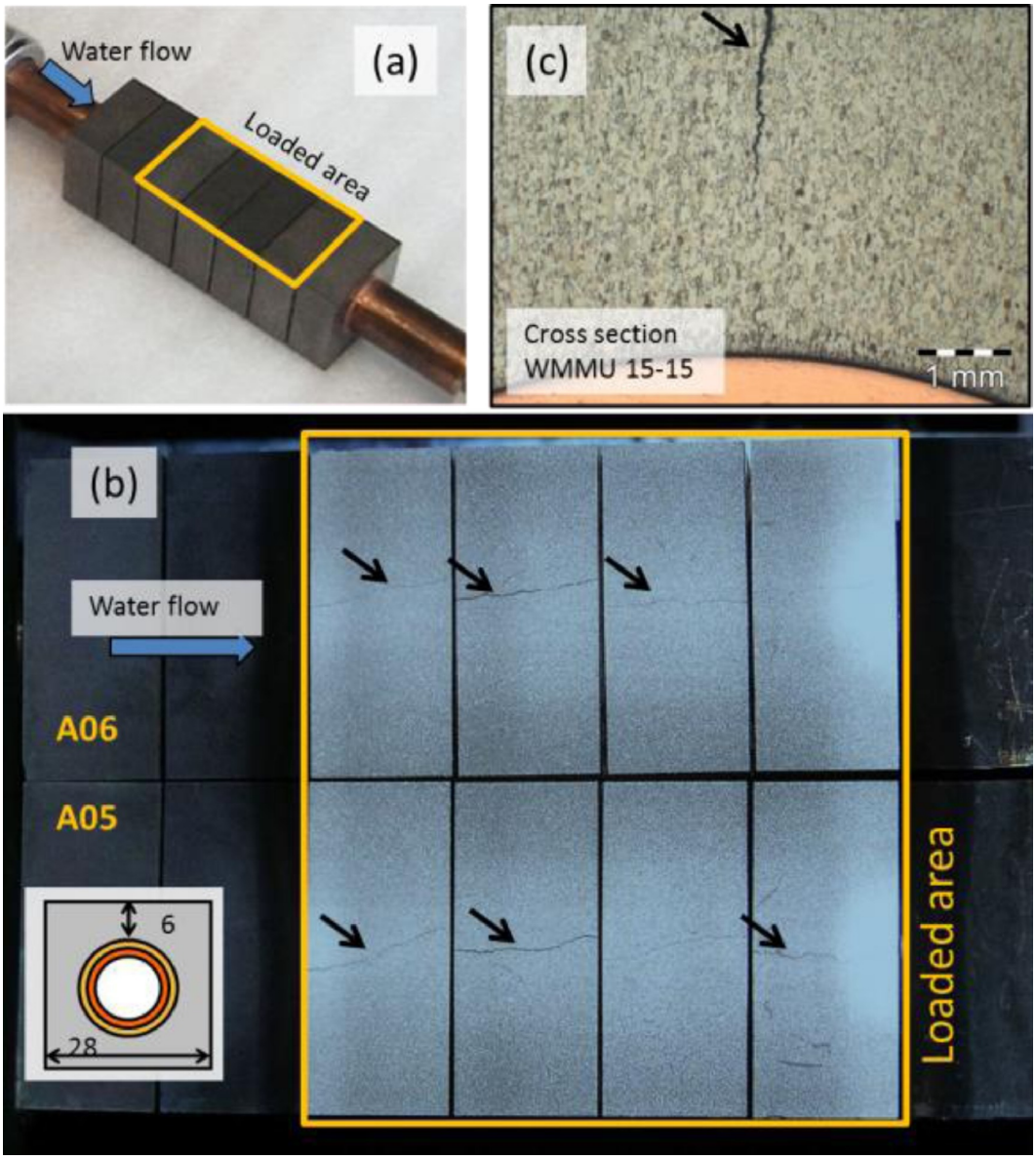


Figure 2.2: Tungsten monoblock divertor after 300 thermal cycles at 20 $\frac{MW}{m^2}$, from (71). (a) shows the impacted area on the monoblock, and (b) and (c) show cracks formed due to high heat flux loading.

2.5.2 Liquid Metal PFC Experiments

2.5.2.1 Liquid Metal Experiments in Fusion Devices

The first experiment to employ lithium as a plasma facing material in a fusion device was on the Tokamak Fusion Test Reactor in America in the 1980s, where lithium wall conditioning was employed to significantly reduce plasma recycling and achieve a significant improvement in plasma performance, so called "super shots" (72). In the 1990's, the first flowing lithium experiments were completed on the T3 and T11-M devices in Russia in the form of jet drops, full sheets, and capillary porous systems (73). This was followed by American experiments running the Current Drive Experiment Upgrade spherical tokamak with a large tray of liquid lithium placed inside of the vacuum vessel in the early 2000s (74). These experiments showed significant improvement in energy confinement time due to improvements in plasma recycling due to lithium presence (see Figure 2.3). Soon after, the National Spherical Torus Experiment tokamak imitated a flowing liquid lithium divertor by replenishing a static liquid lithium film on the divertor surface (75).

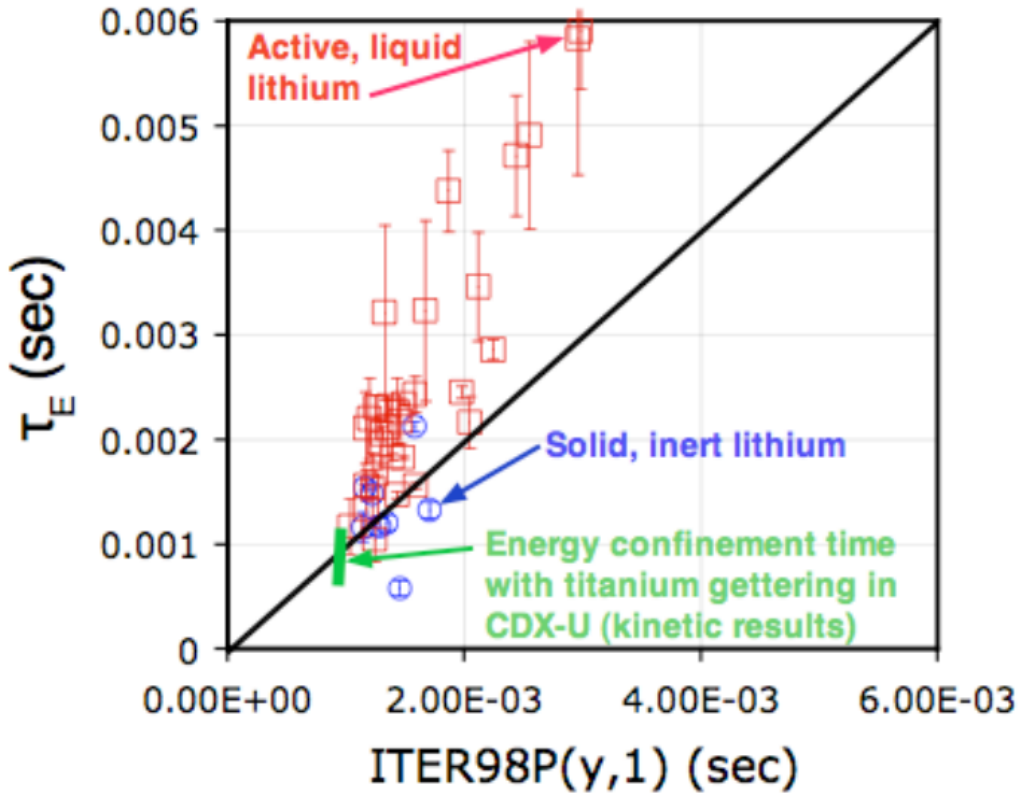


Figure 2.3: Plot of energy confinement time in the Current Drive Experiment Upgrade spherical tokamak device for trials run with liquid lithium (red) and solid lithium (blue), from (74).

Currently, there are several MHD-focused and fusion relevant liquid metal experiments performed globally. The Lithium Tokamak Experiment (LTX) was the first tokamak to have liquid lithium covering all of the interior vacuum vessel walls, which led to a six-fold improvement in energy confinement due to the decreased plasma recycling as the lithium coating absorbed incident cold plasma (76). This was a static lithium experiment where a tray of liquid lithium was heated in LTX and evaporated lithium condensed on the walls of the device and evaporated along the vacuum vessel internal walls as the vessel heats up. The Flowing Liquid Lithium Limiter (FLiLi) was the first study of continuously flowing liquid metal in a fusion device. The limiter flows approximately 0.1 mm of lithium at about 2 $\frac{cm^3}{s}$ down a stainless-steel coated channel in the presence of high-performance plasmas at EAST to confirm the operational stability and heat exhaust abilities of flowing liquid lithium (30). Results showed the emission of lithium from the limiter surface led to a measurable reduction in plasma recycling and presence of PFC impurities (such as tungsten or molybdenum) in the plasma (30). The focus of these experiments is limited to lithium-plasma interactions using pre-existing plasma diagnostics, as there is currently no reliable method to measure the fluid properties such as velocity or height of liquid metal in a fusion device. This remains an area for future development.

2.5.2.2 Bench Scale Free Surface Liquid Metal Experiments

The University of California, Los Angeles pioneered the experimental study of flowing, free surface liquid metal flow in fusion-relevant magnetic fields (46, 77, 78) at the bench scale. The Magnetic Torus (MTOR) facility measured the surface flow characteristics of a liquid metal jet placed within spatially varying magnetic field gradients. A 2 mm jet of galinstan - a eutectic alloy of gallium, indium and tin - was introduced to an arrangement of toroidal field coils and permanent magnets producing overall magnetic fields of 1.3 T. The toroidal magnetic field varied spatially from 1.12 T to 0.6 T from inboard to outboard, respectively. This was the first liquid metal study to utilise the non-invasive, laser triangulation method to gather surface height information across the galinstan jet. The physical flow characteristics that were measured include turbulence, hydraulic jump, flow deflection, surface wetting, and

the presence of waves. Overall, MTOR provided an experimental basis for liquid metal flows under large, spatially varying magnetic fields, which guided the design of more complex liquid metal experiments.

The Liquid Metal Experiment (LMX) is the main liquid metal experiment at PPPL that is not run in a fusion device. This experiment has been built to study the electromagnetic control of liquid metal to optimize flow parameters and heat transfer (79). LMX utilizes a thin (few millimeter) film of galinstan flowing at 4-10 litres per minute across a 100 cm long acrylic channel. The set up includes an electromagnet capable of producing a transverse magnetic field up to 0.33 T and copper electrodes to generate parallel and antiparallel electrical current up to 140 A. Laser triangulation is used to measure the height of the surface across the sheet, and this facility has been used to confirm that wave damping, heat transfer, flow velocity, and hydraulic jumps can all be electromagnetically controlled. Additionally, researchers from PPPL and Johns Hopkins University have measured liquid metal velocity using an IR camera and particle tracking software (80). Recently, the effect of a transverse magnetic field on free surface, developing liquid metal flow was recently measured at PPPL and compared to analytical and numerical solutions (45). This work showed strong agreement near the fluid outlet, but a higher height was measured near the inlet than what was predicted. Throughout these bench scale experiments, as well as the experiments performed in fusion devices, uniform flow spreading is a significant issue that remains a key area for future development. Some work is described in this thesis towards solving this dilemma (see Chapter 5); however a solution has yet to be identified.

Facilities similar to LMX have been developed at Xi'an Jiaotong University to study the effects of MHD drag on the development of surface waves on thin-film, liquid metal flows (81). This experiment has shown transverse magnetic fields dampen flow turbulence along the field lines (81). In 2020, they produced a scaling law relating liquid metal height change to flow rate, channel angle, and transverse field strength (82).

The Centre for Plasma Material Interactions at UIUC studies plasma material interactions for applications in fusion, semiconductor and plasma manufacturing industries. The Materials Characterization Test Stand (MCATS), Lithium Metal Infused Trenches (LIMIT) and the

Hybrid Illinois Device for Research Applications (HIDRA) experiments are most relevant to this research. The Materials Characterization Test Stand (MCATS) is a test chamber for experiments involving the wetting and surface corrosion of various liquid metals on fusion relevant metal surfaces to optimize liquid metal wetting parameters (83). The LIMIT experiment uses thermoelectric magnetohydronamic (TEMHD) flow of liquid Lithium on laser textured stainless steel trenches to study potential methods of reducing liquid metal dry out and improving surface wettability (84). More recently, UIUC has demonstrated that liquid lithium will also pump (28, 29) and remove helium (85) and this potentially solves the critical helium ash problem in fusion. UIUC is also exploring the use of 3D posts and meshes to induce TEMHD flow (86).

Only one study has been completed investigating the effects of a surface normal magnetic field on free surface, liquid metal flow (44). This study was performed by Platacis at the University of Latvia and it derives an approximate formulation for the effect of a poloidal magnetic field, flow rate and channel angle on liquid metal height. This is accompanied by qualitative observations of galinstan flow down a 16 cm long and 10 cm wide copper channel in the presence of a poloidal magnetic field. Video recordings show an improvement in flow stability in the presence of the 4 T poloidal field, but no quantitative measures of the liquid metal flow were made. A summary of liquid metal experiments discussed in this section are summarised in Figure 2.4.

Development of facilities to test the capabilities of liquid metals under steady-state, DEMO-like neutron conditions are currently underway. The International Fusion Materials Irradiation Facility DEMO Oriented Neutron Source is currently under construction and will test materials, including liquid metals, at DEMO-relevant neutron fluxes (89, 90). Also, the Flowing Liquid Torus has been proposed by PPPL to study the flow mechanics of a liquid metal divertor and develop appropriate diagnostics (91). In addition to liquid metal PFCs, Goldston has proposed a lithium vapour box detached divertor design which is scheduled to be tested experimentally at the linear plasma generator Magnetised Plasma Generator and Numerical Modelling for Plasma-Surface Interaction (Magnum PSI) (92, 93). From the literature, it is clear that liquid metal research for PFCs is under development and significant

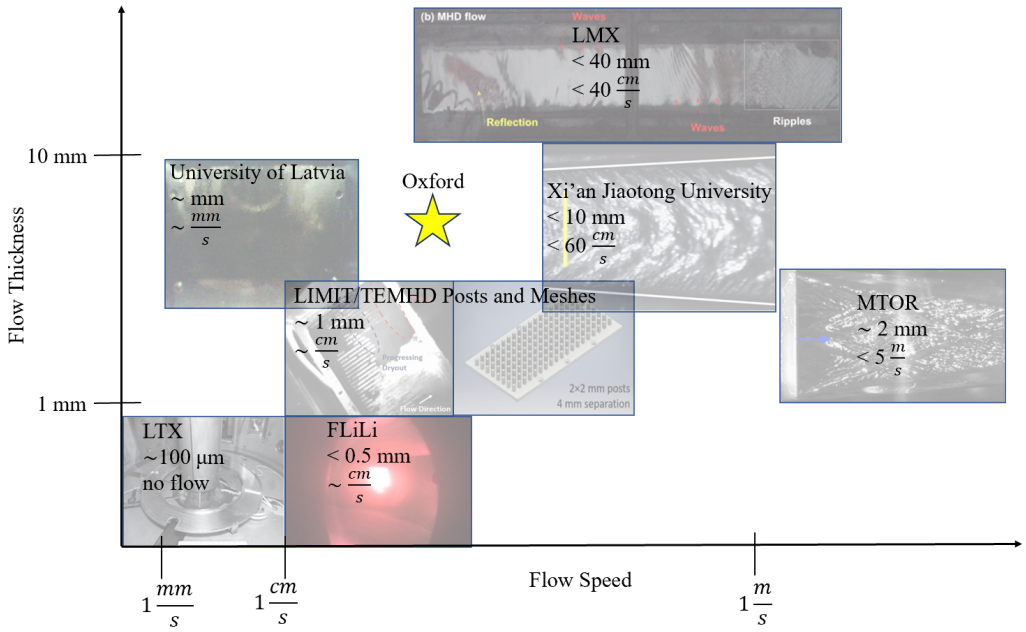


Figure 2.4: Summary plot of liquid metal experiments described in this chapter showing relative liquid metal thickness and velocity (the experiments described in this thesis are noted by the yellow star). These images include Figure 5 from (44), Figure 8 from (30), Figure 48 from (87), Figure 12 from (45), Figure 4.2 from (62), Figure 3 from (88), Figure 3 from (82) , and Figure 32 from (77)

work remains to quantify liquid metal behaviour against existing analytical and numerical solutions.

2.6 Summary of Literature Gaps

From the literature survey, it is shown that free surface liquid metal flows have been studied extensively for a fully developed flow scenario, but significant work remains to derive suitable developing flow equations for liquid metal flow. The numerical modelling of liquid metal flows has evolved from solely bespoke numerical models to a more recent focus on modifying existing commercial codes to simulate liquid metal behaviour; however very few numerical models have been experimentally validated. Lastly, the experimental study of free surface liquid metals has focused primarily on the effects of transverse magnetic fields, almost no quantitative data regarding the impacts of surface normal fields exists in the literature. This thesis describes work carried out to close the analytical and numerical gaps in Chapter 4 and experimental gaps in Chapter 5 by producing an analytical, numerical, and

experimental study of liquid metal flow in the presence of a surface normal magnetic field.

Chapter 3

LIQUID METAL EXPERIMENTAL FACILITY AND APPARATUS

3.1 Overview

This chapter details the design of a new experimental facility constructed at the Oxford Thermofluids Institute (OTI) at the University of Oxford, called the Oxford Liquid Metal Experiment (OLME), to explore the effects of unidirectional magnetic fields on liquid metal flow. The effects of magnetic fields on liquid metal flow have been explored analytically and numerically, but there is a dearth of experimental data to support these theoretical claims (81). The aim of this chapter is to describe the design and testing of the OLME.

3.2 Background Information

3.2.1 Overview

In this study, a simplified case of flow down a flat channel, representative of a section of a divertor or limiter and neglecting the curvature of the fusion vessel, was considered. A general overview of the key equipment described in the remainder of this chapter is shown in Figure 3.1.

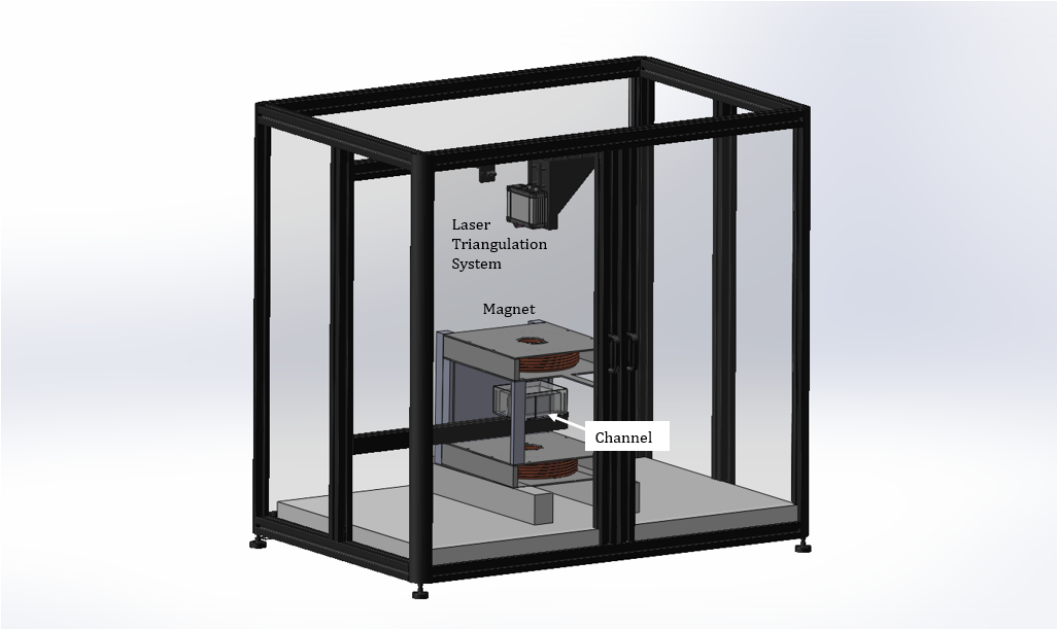


Figure 3.1: CAD drawing of the Oxford Liquid Metal Experiment, showing the electromagnet, channel, and laser triangulation system

3.2.2 Choice of Liquid Metal

There are several liquid metals currently under investigation for PFCs: lithium, tin, tin lithium, and gallium. Lithium is currently considered the most promising liquid metal for plasma facing components. Lithium has a low atomic mass, which leads to lower Bremsstrahlung radiation losses and less dilution of the plasma fuel (94). Additionally, lithium can absorb and pump hydrogen isotopes from the scrape off layer to enable a low recycling plasma regime, which in turn leads to more stable plasma with higher confinement time and average temperature (95). However, because lithium absorbs tritium, there is a need for efficient tritium extraction technologies in order to reduce the overall tritium inventory in a fusion plant(37).

Lithium has a melting point of 180°C and is highly flammable when exposed to air, which is not a limitation in a fusion environment due to the high temperatures and vacuum requirements present in the PFC region. However, lower melting point fluids that are less reactive are preferred for bench scale experiments outside of a traditional fusion environment.

In the present study, galinstan[1], an alloy of gallium, indium and tin, is used as the liquid metal. Galinstan has similar electrical properties to lithium (see Table 3.1) however, galinstan

[1]Galinstan is a trademark of Geratherm Medical AG, a German medical company.

Table 3.1: Comparison of key parameters for galinstan and lithium.

Property	Lithium	Galinstan
Melting Point (°C)	180	-19
Electrical Conductivity (S/m)	4×10^6	3.46×10^6
Density (kg/m^3)	510	6400
Kinematic Viscosity (m^2/s)	1.2×10^{-6}	$0.375x10^{-6}$
Surface Tension (N/m)	0.4	0.535

is liquid at room temperature and is not flammable in air (96). In the presence of air, galinstan forms an oxide layer which can be chemically reduced by mixing with aluminum foil strips. The aluminum combines with the oxide layer to exothermically form a solid aluminum oxide crust. This crust can be scraped off the surface, leaving pure liquid galinstan.

3.3 Experimental Facility Overview

The OLME was designed by the author and constructed at the OTI to enable a quantitative investigation of liquid metal flow under uniform magnetic fields. A process flow diagram of the experimental facility is shown in Figure 3.2 and key OLME parameters are listed in Table 3.2, where characteristic length is the distance from the inlet to outlet. The facility was comprised of a flowing galinstan loop with a test section exposed to a strong magnetic field produced by a bespoke electromagnet[2]. The test section was where the liquid metal free surface developed. This section included a polycarbonate base with a copper channel insert and a fitted polycarbonate lid that provided an inert environment to slow down the oxidation of galinstan. Both copper and stainless steel channel inserts were created, but the copper channel was used to capture the data recorded in this thesis because copper has a greater electrical conductivity than stainless steel, leading to greater MHD effects. Additionally, larger and more complex channel designs were explored in an effort to enhance surface wetting, including various distributor designs to improve flow around the inlet. These are detailed at the end of Chapter 5. A gear pump[3] moved galinstan from the test section to the storage tank, which was constructed from polytetrafluoroethylene.

[2]Woodruff Scientific, a scientific instrumentation development company based in New Mexico, USA, built the electromagnet

[3]The gear pump used in this experiment if the WZ-74014-22, manufactured by Cole Parmer

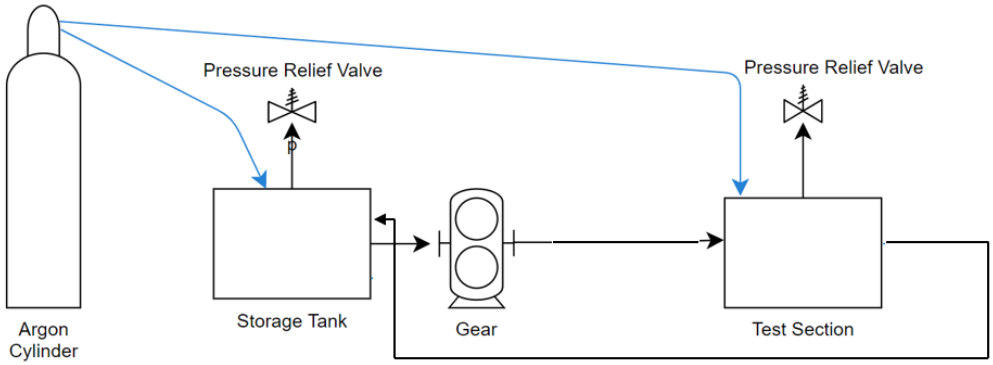


Figure 3.2: Process flow diagram for the liquid metal loop constructed for the OLME. The blue lines represent flow of argon, and the black lines represent flow of galinstan.

Table 3.2: Oxford Liquid Metal Experiment Characteristics

Variable	Value	Definition
L	90 mm	Characteristic flow length
a	12.5 mm	Half channel width
t	3 mm	Wall thickness
ρ	6400 kg m^{-3}	Galinstan density
Q	(5 - 8.33) mm^3 s^{-1}	Flow rate
σ	3.46×10^6 S m^{-1}	Electrical conductivity of galinstan
σ_w	5.96×10^6 S m^{-1}	Electrical conductivity of copper
μ	2.4×10^{-3} Pa s	Dynamic viscosity of galinstan
g	9.81 m s^{-2}	Acceleration due to gravity
B_z	up to 0.16 T	Surface Normal magnetic field

3.3.1 Test Section

The test section was primarily made of polycarbonate, with a 100 mm x 100 mm base and a fitted lid. A removable copper channel insert is fitted on the polycarbonate base, as shown in Figure 3.3, with dimensions shown in Figure 3.12. This design allows for quick iteration of channel material in the future. The channel was connected to the rest of the liquid metal loop as shown in the process flow diagram in Figure 3.2. The liquid metal was studied at flow rates ranging from 5 to 8.33 mm^3/s to generate average flow speeds from 40 mm/s to 67 mm/s for a 5 mm deep film of flowing galinstan.

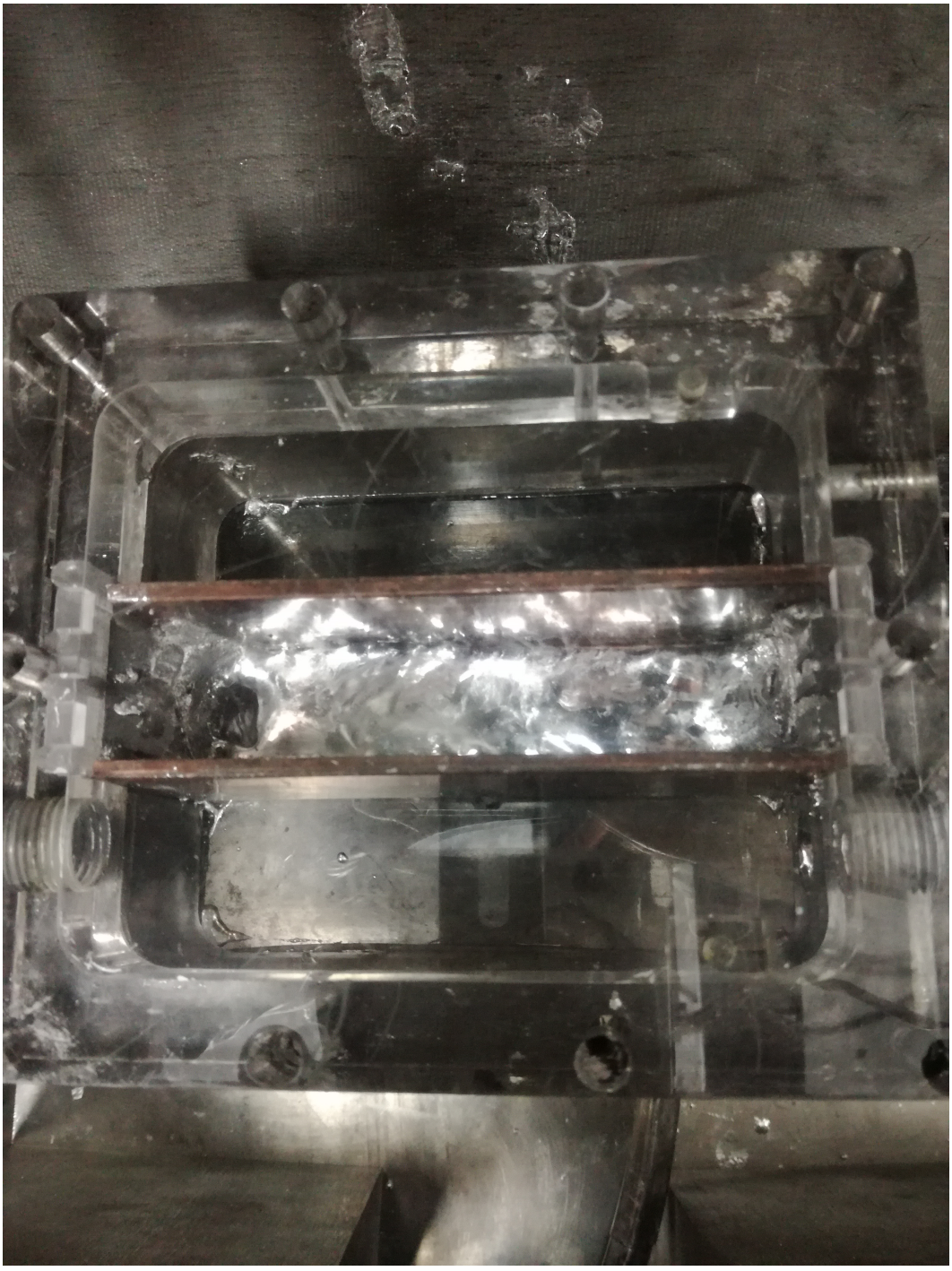


Figure 3.3: Top view of the channel design, showing the copper channel slotted into the polycarbonate base channel. Flow occurs from right to left.

3.3.2 Electromagnet

3.3.2.1 Electromagnet Specifications

An electromagnet composed of two copper solenoids capable of achieving a magnetic field of 0.16 Tesla was procured by the author to perform experiments to study the effect of magnetic field strength and orientation on liquid metal flow. The magnet specifications are listed in Table 3.3.

Table 3.3: Electromagnet Specifications

Parameter	Value
Maximum Magnetic field (200 mm coil spacing)	0.16 Tesla
Current	1800 A
Voltage	23.92 V
Maximum on time at maximum power	30 seconds
Maximum Temperature	240°C
Magnet Mass	50 kg
Coil Outer Diameter	210 mm
Coil Inner Diameter	70 mm
Number of turns in copper coil	48 (8 layers of 6)
Wire Gauge	0 square HAPT
Winding Pack Height	50 mm
Winding Pack Width	6 6mm
Upper Coil Inductance	0.194 mH
Lower Coil Inductance	0.281 mH
Total Resistance	0.02 Ohms

The magnet was constructed from 0 gauge (8.25 mm diameter) copper wire. A cylindrical iron core (50 mm length and outer diameter 70 mm) was included in the bore of the lower electromagnet to increase both the strength and uniformity of the magnetic field (see Figure 3.4). An identical, but removable, iron bore was placed in the upper electromagnet. This iron bore was removed to allow for visual access of the liquid metal test section when the magnetic field was surface normal to the fluid flow. This bore would be replaced for future experiments involving a transverse magnetic field, where visual access to the liquid metal flow would be unaffected by the presence of the additional iron bore.

The electromagnet was limited to an operation time of 30 seconds at full power due to the temperature rating for the polyimide coating of the copper wires (240°C). This duration was sufficient as we expect the liquid metal to reach steady state in a significantly shorter

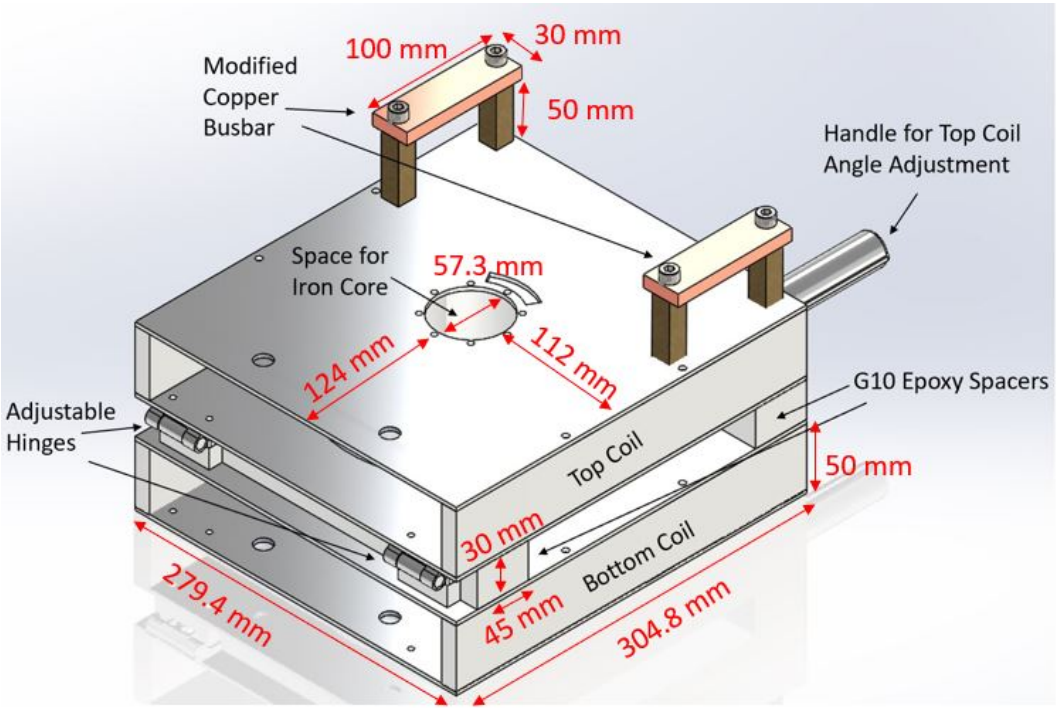


Figure 3.4: CAD drawing of the electromagnet labelled with key features.

time. The magnet frame was machined from stainless steel. One thermocouple was placed on the interior of the magnet winding on both the top and bottom coil, between the third and fourth winding layer along the coil midplane. A third thermocouple was placed on the top of the lower iron core. A 50 KW power supply[4] was used to power the magnet. The magnet has an inductance to resistance ratio of 0.1527 seconds, meaning magnetic field fluctuations can be generated on the order of tens of Hz, for potential future experiments studying the influence of magnetic field fluctuations on liquid metal flow stability.

The magnet was designed to provide optimum flexibility for future experiments. There are several parameters of the magnet that can be modified. Firstly, the magnet can be physically rotated to deliver a transverse or streamwise magnetic field relative to the fluid flow. The distance between the top and bottom coil can be changed using different sized epoxy spacers. Also, the relative angle of both coils can be modified using angled epoxy blocks due to the hinge mechanism in place holding the two coils together (see Figure 3.4). This can be used to generate magnetic field that varies inversely along the channel length, which is more similar to what is experienced in a tokamak and suggested as future work.

[4]The power supply was manufactured by Magna-Power and is the model TSD25-2000/380.

$$I_p = I_{100}\sqrt{\frac{100}{F}} \tag{3.1}$$

To connect the magnet to the power supply, two 50 mm^2 (BS 638) cables were used in parallel for the power input and output. The BS 638 cables were rated for 285 A for a duty cycle of 5 minutes, but they were used on this experiment for 30 seconds. Equation 3.1 was used to calculate the permissible transient cable loading, where I_P is the permissible cable loading for a duty cycle less than 100 percent, I_{100} is the permissible cable loading for a duty cycle of 100 percent (285 A for this case), and F is the required duty cycle calculated as a percentage of 5 minutes (F = 10 for this case). From this equation, I_p was calculated as 901 A. Thus, by using two cables in parallel, a total of 1802 A can be safely achieved for over 30 seconds. The maximum operating temperature of the cable was 85°C, so it was considered necessary to measure the cable temperature at higher current values to ensure this temperature was not exceeded.

In an effort to facilitate safe connection of the power supply cables to the magnet, the original copper busbar attached to the magnet was enlarged from 27 mm x 15 mm to 100 mm x 30 mm and supported on the magnet frame using polyether ether ketone (PEEK) supports. This was done to improve the integrity of the connection point for the power cables and to prevent the formation of large electrical resistance at the cable connection point. This addition is visualised in the diagram of the magnet in Figure 3.4.

3.3.2.2 Electromagnet Modelling

The magnetic field (B) produced by an electromagnet at the pole face can be described by Equation 3.2, where μ_0 is the magnetic permeability of a vacuum, n is number of turns, (l_s) is solenoidal length. To generate a region of relatively uniform magnetic field, two electromagnets were used in series and the superposition of their magnetic fields can produce a relatively large region of uniform magnetic field.

$$B = \mu_0 \frac{nI}{l_s} \tag{3.2}$$

To model this superimposed magnetic field region and optimise the magnet design parameters, FIESTA[5], a MATLAB based code, was used. The input values for this code were the electrical current, inner diameter of the electromagnet coil, wire gauge, dimensions of the coil winding pack, number of layers of copper wire and number of turns of the copper wire. The outputs include a magnetic field distribution plot, required supply voltage, and electrical power.

This code was used to determine the optimal parameters for the electromagnet so that the power requirements can be reduced below 50 KW due to the high cost of a larger power supplies. From FIESTA, it was determined by the present author that a coil with the parameters in Table 3.3 should be used to reduce the required power parameters. The minimum inner diameter of the magnet was set to 70 mm to allow for adequate visual access to the uniform field region for the optical diagnostic used to measure liquid metal film height. The number of turns was maximised as well as the wire diameter in order to significantly reduce the current requirements for the coil.

The uniform field region existing between the two coils was maximised to allow for as much of the channel volume to be included in the region of high, uniform magnetic field while remaining below the 50 KW power requirement. However, increasing the spacing between the coils reduced the peak magnetic field reached, so a magnet with adjustable spacing was selected to allow for precise maximisation of the peak field for various channel volumes. Additionally, to keep the power requirements below 50 KW, the maximum liquid metal channel length was limited to 100 mm, to allow for uniform magnetic field across the entire channel length.

The magnetic flux density plot for the magnet run at full power (24 V and 1800 A) is shown in Figure 3.5.

Magnetic field density plots were generated using Finite Element Method Magnetics (FEMM)[6]. Comparison between the experimental magnetic field and the FEMM prediction

[5]FIESTA was developed by Geoff Cunningham, who is a magnet engineer at the Culham Centre for Fusion Energy (CCFE), for use in the design of electromagnets in fusion environments (97)

[6]FEMM is a programme developed by David Meeker to solve electromagnet problems (98).

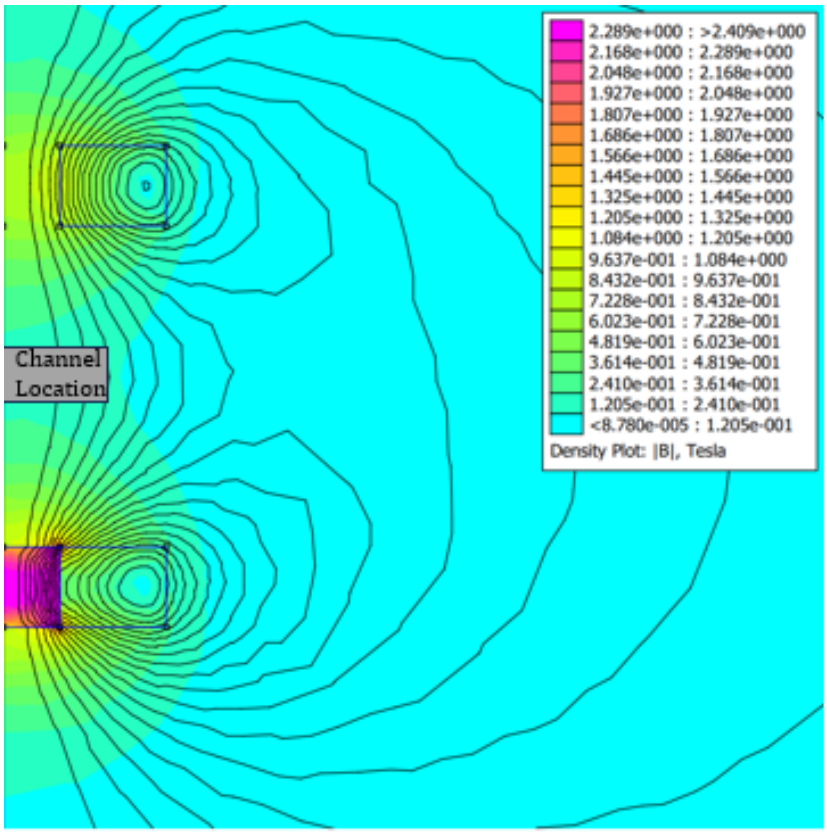


Figure 3.5: Finite Element Magnetic Model of the magnetic field present at full power (1800 A). The relative location of the channel is shown in grey.

showed very good agreement, as shown in Figure 3.6. This plot was constructed by placing the gaussmeter just above the iron core (where the field is it's greatest) and comparing the measured field to the estimated field from the FEMM model.

Additionally, a transient thermal, finite element analysis model was undertaken to describe the magnet heating using ANSYS Mechanical (see Figure 3.7). The copper coil was modelled as a solid copper cylinder with a central iron core. To account for the presence of air gaps, primarily in the radial direction from the core to the outer surface, the thermal conductivity along the x and y axis was represented as 23% of the thermal conductivity of copper. This percentage was determined iteratively through comparison with experimental data, and could be reasonably interpreted as the coil fill factor. The fill factor is the ratio of conductor material to the provided area. For hand-wound round cables, the fill factor is usually a maximum of 45%, and lower fill factors yield lower thermal conductivity (99, 100).

To validate the model, a comparison plot of the temperature profiles generated for the magnet run at 200 A for 400 seconds is shown in Figures 3.8 and 3.9. Temperature probes

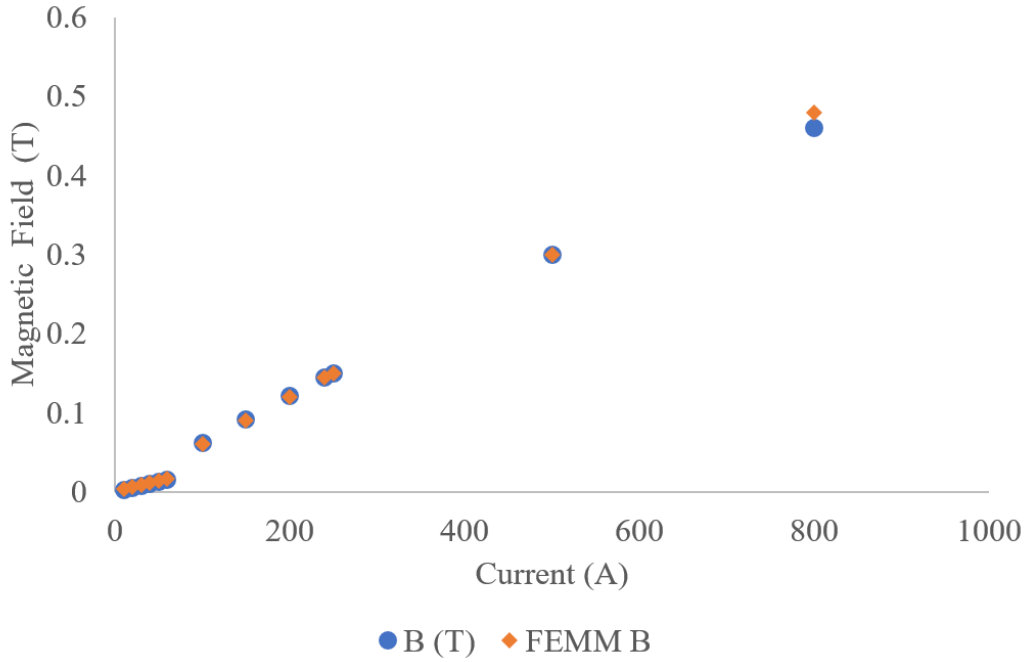


Figure 3.6: Comparison of magnetic field output near the bottom coil surface from the magnet (blue points) compared to the FEMM model (orange points).

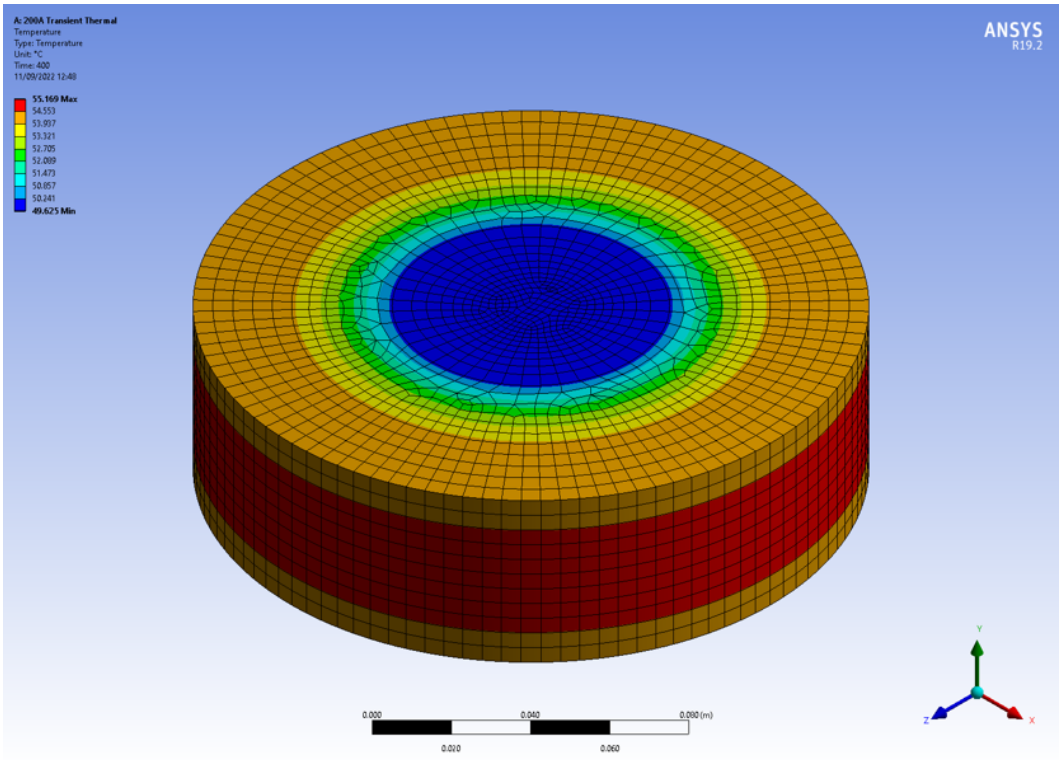


Figure 3.7: Results from an ANSYS Mechanical FEA analysis of the bottom copper coil with iron core heating over 400 seconds with 200 A current.

were placed in the FEA model in the same location as the thermocouples placed in the magnet for accurate comparison. The bottom copper coil has an iron core and the top copper coil is an air core. The model shows good agreement with the experimental findings.

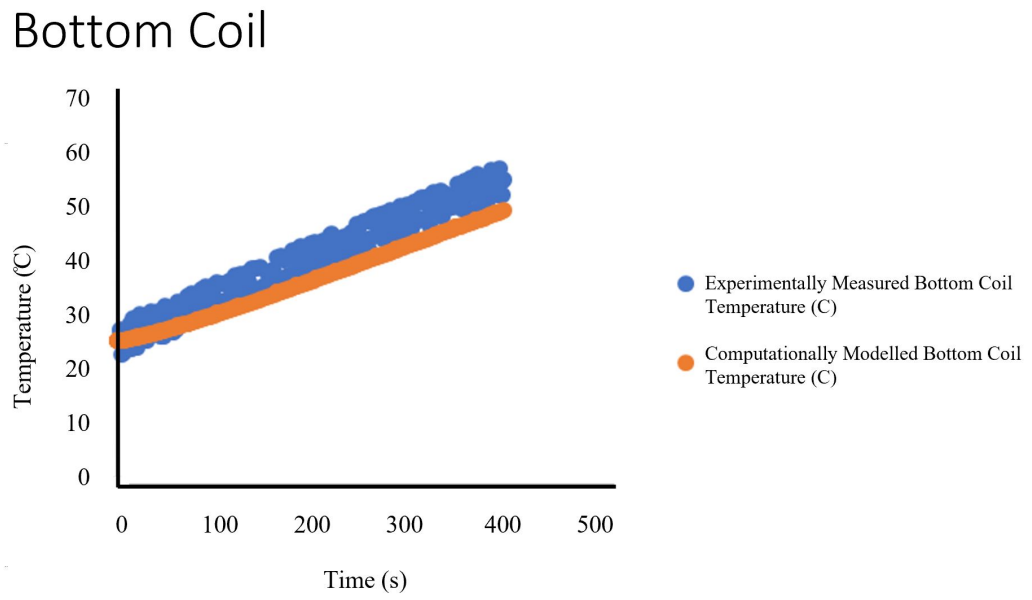


Figure 3.8: Comparison of ANSYS Mechanical FEA simulated temperature and experimental (actual) temperature of the bottom copper coil with iron core heating over 400 seconds with 200 A current.

The maximum operable current was 1200 A in practice rather than the 1800 A predicted, due to the larger internal electromagnet than expected.

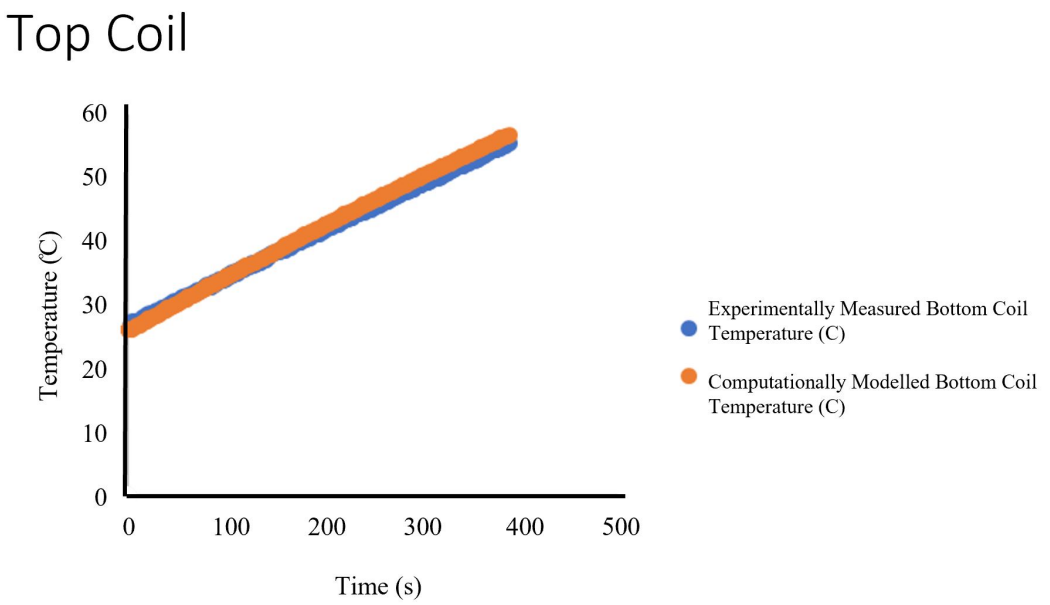


Figure 3.9: Comparison of ANSYS Mechanical FEA simulated temperature and experimental (actual) temperature of the top copper coil with air core heating over 400 seconds with 200 A current.

3.3.3 Safety

Throughout the design and implementation of this new experimental facility, personal protection and protection of investment was considered and accounted for. The electromagnet was the source of the most significant risks and measures used to mitigate these risks are discussed in this section.

3.3.3.1 Magnet Safety

The three major safety concerns that must be thoroughly considered when using the magnet are: (1) magnetic ”snatching” or interference with nearby magnetic equipment and (2) melting of equipment, physical burns and risk of fire due to ohmic heating, and (3) electrical short circuits. A summary of mechanisms incorporated by the author to mitigate these concerns is found here:

1. The magnet was placed in a corner and in a space with low foot traffic to prevent accidental exposure of people and equipment to magnetic fields (Targeting risk #1).

2. Two emergency stop buttons were placed in the laboratory space. One is near the closest exit door and is used to shut off three phase power to the room. The second

is near the control computer and is used to locally shut off power to the power supply (Targeting risk #2 and 3).

3. The space around the magnet where the magnetic field was strong enough for ferrous objects ”snatching” or interference with metallic or electronic equipment was clearly delineated in the space and warning signs were placed on all entrance doors to notify those entering the room that a magnetic field may be present (Targeting risk #1).

4. A perspex case was constructed around the magnet to prevent physical access when the magnet was in operation (Targeting risks #2 and 3).

5. The hardware-based power supply interlock was set to shut the electrical supply off if the magnet case door was opened or if the emergency stop was pressed (Targeting risks #2 and 3).

6. The power supply automatically shuts off when the magnet temperature exceeds 240°C, measured by a Labview programme (Targeting risk #2).

7. The magnet underwent the UK Conformity Assessed (UKCA) marking process to ensure safe operation. This process involved a physical assessment of the magnet and operating procedure by an external conformity marking agency[7] (Targeting risks #1,2 and 3).

Threshold limit values for human exposure to magnetic fields are provided by he International Commission on Non Ionising Radiation Protection and Health Protection Agency UK (101). For people without ferrous metal implants, the maximum allowed magnetic field value is 2 Tesla (20,000 Gauss), and the 8 hour time weighted average maximum exposure is 60 mT (600 G). Exposure to high magnetic fields may cause nausea, dizziness, and a metallic taste in the mouth.

[7]UKCA marking was performed by Conformance, which is an independent specialist in compliance regulations.

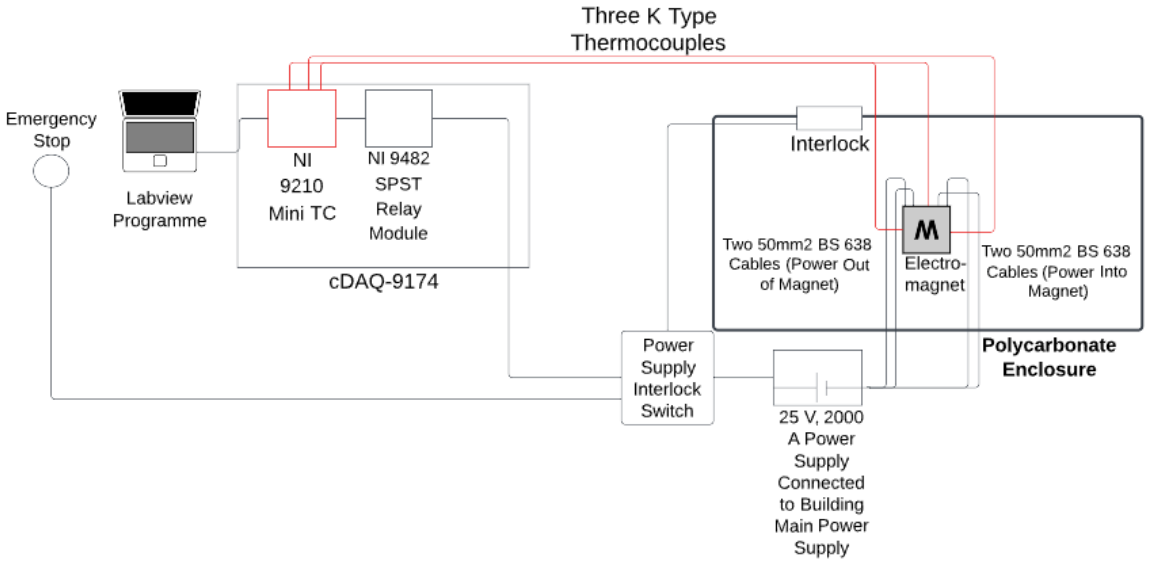


Figure 3.10: Schematic of the magnet and relevant safety related control systems.

In the vicinity of a powerful magnet, there are three magnetic field zones, classified according to potential hazard, specified in these guidelines (102):

1. 5 Gauss (0.5 mT) and Above: Interference with metallic body implants may occur.

2. 30 Gauss (3 mT) and Above: Magnetic attraction of ferrous objects can occur.

3. 150 Gauss (15 mT) and Above: Magnetic "snatching" of stationary ferrous tools and equipment can occur.

In order to respect these guidelines, it was important to design the laboratory space such that ferrous objects and vulnerable persons were kept at appropriate distances. The FEMM model was used to determine the location of the 5, 30 and 150 Gauss magnetic fields at full power. The horizontal and vertical distance from the centre region of the electromagnet pair where the field tapers off to each of these values is listed in Table 3.4. Because the magnet orientation rotates to generate transverse and surface normal oriented magnetic fields, the further distance (the vertical distance from the magnet centre) was used when physically marking the laboratory space. All people and ferrous equipment were kept out of the 5 Gauss line during operation of the magnet, except for flowing liquid metal, the copper channel, a camera and a laser triangulation system used to measure the liquid metal thickness. The copper channel was bolted in place to prevent any ferrous "snatching."

Table 3.4: Magnetic Field Safety Guidelines

Magnetic Field Guideline	**Horizontal Distance from Magnet Centre (mm)**	**Vertical Distance from Magnet Centre (mm)**
150 Gauss	156	154
30 Gauss	194	402
5 Gauss	816	1075

3.3.4 Instrumentation

A height detection system that could work around restrictive optical access was required for the proposed experiment. A review of both invasive and non-invasive liquid metal height detection methods can be found in (103). A system that was non-invasive, requires minimal optical access, and can operate in the presence of magnetic field was ideal. Accordingly, a Micro-Epsilon ScanControl LLT3000-100/BL was used to collect liquid metal height values in this experiment. This system projected a blue (405 nm) semiconductor laser line with linearity ±0.006 % across a surface. Blue light has a smaller wavelength than red light, which is the traditional laser colour used for laser triangulation systems. Smaller wavelengths provide a sharper, more narrow beam and less surface penetration (resulting in less interreflections), which results in a more clear signal when measuring specular surfaces like liquid metals (104). The measurement line spreads 26 mm along the liquid metal film and measurements can be taken in the range 200 mm to 340 mm from the sensor, with profile frequency up to 10,000 Hz. The measurement resolution is stated as 9 micron. The placement of this data capture instruments are visualised in Figures 3.11 and 3.12.

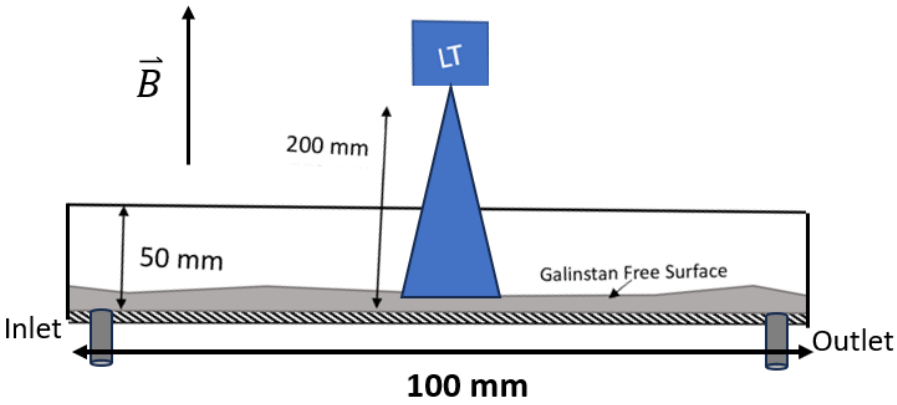


Figure 3.11: Side-view schematic of liquid metal flow and relevant diagnostics.

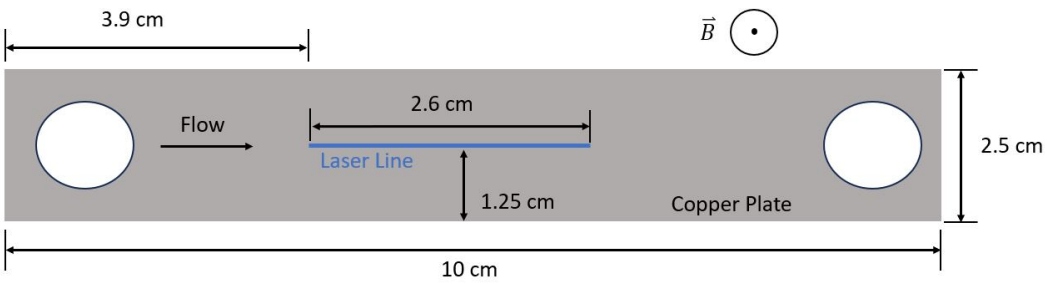


Figure 3.12: Top view schematic of liquid metal flow and laser line overlay, showing the position of laser line on the liquid metal surface.

3.3.4.1 Laser Triangulation Methodology

Laser triangulation involves the projection of light in the form of a point, line or pattern onto a reference surface and the capture of the reflected light by a camera array sensor. The light is then projected onto the same surface but with the object of interest (in this case, the liquid metal film) placed on top of the reference surface. This causes the light received by the camera array sensor to change position and create a distorted image. A calibration of physical height changes, in micrometres, to perceived height changes by the camera sensor, in pixels, must be completed. This process requires diffuse reflection from the measured surface. This is followed by cross-correlation to create displacement vectors that relate the distorted image to the reference image (105, 106). A triangulation schematic is shown as Figure 3.13.

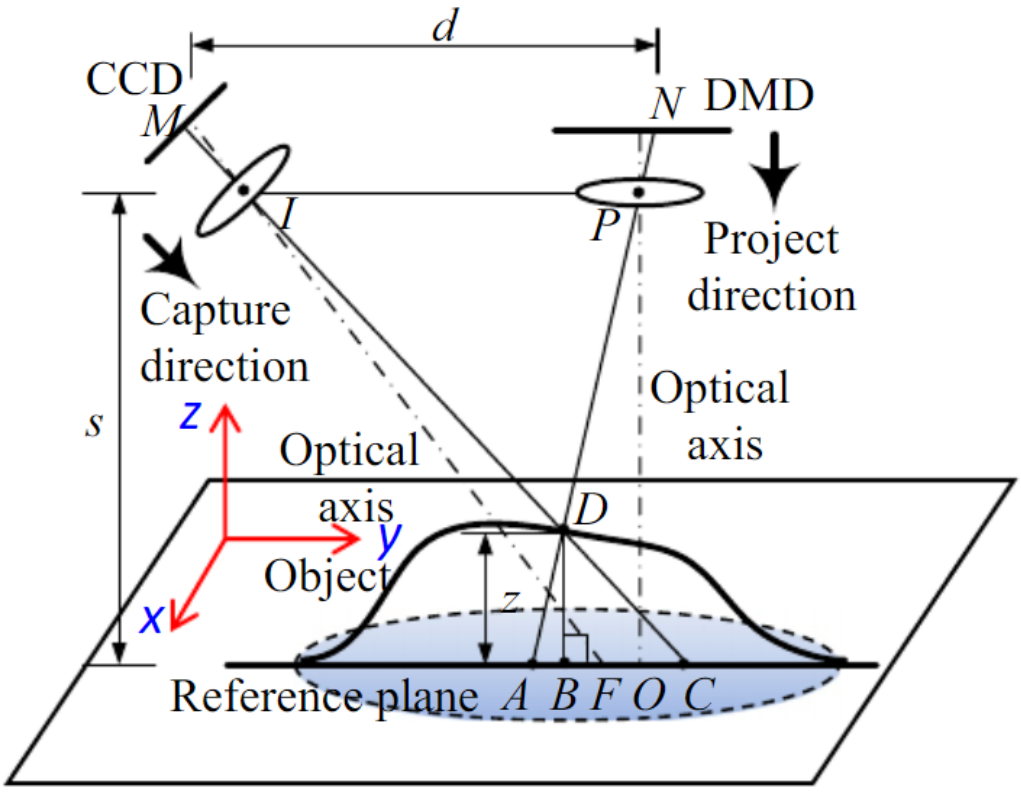


Figure 3.13: Schematic illustrating the triangulation method, from (105)

In Figure 3.13 , the object height $\overline{BD}$ can be linearly related to $\overline{CA}$, which is the perceived pixel displacement by the sensor, using trigonometry and the assumption that the distance 's' from the sensor to the reference plane is much larger than the object depth ($\overline{BD}$). This

result is captured in Equation 3.3, where K is a constant that is determined by comparing the known physical height changes to height changes captured by the sensor, as shown in Figure 3.13.

$$\overline{BD} = K\overline{CA} \tag{3.3}$$

Cross-correlation is then used to create displacement vectors that match each illuminated point from the distorted image to an illuminated point on the reference image. In cross-correlation, a small window of data in the reference image is compared to a larger window of data in the distorted image to find a local maximum of the cross-correlation coefficient, R, shown as Equation 3.4 (105). This allows for the alignment of data collected on the distorted plane to the appropriate physical location on the reference plane.

$$R(m,n) = \frac{\Sigma_i \Sigma_j (I_r(i,j) - I_r)(I(i+r, j+s) - \bar{I})}{\sqrt{\Sigma_i \Sigma_j (I_r(i,j) - I_r)^2 (I(i+r, j+s) - \bar{I})^2}} \tag{3.4}$$

where I and I_r represent the distorted and reference image, respectively, $\bar{I}$ and $\overline{I_r}$ are the image intensities for the distorted and reference image, respectively, i and j are image coordinates, and r and s are displacements.

3.3.5 Labview

A Labview programme was created to streamline the data capture process. The programme contains 5 main controls:

1. Control of the magnet power supply current and voltage settings
2. Monitoring of magnet temperature
3. Automatic shut off of the magnet's power supply in the event of overheating
4. Simultaneous capture of laser triangulation and colour camera data
5. Monitoring of the magnetic field

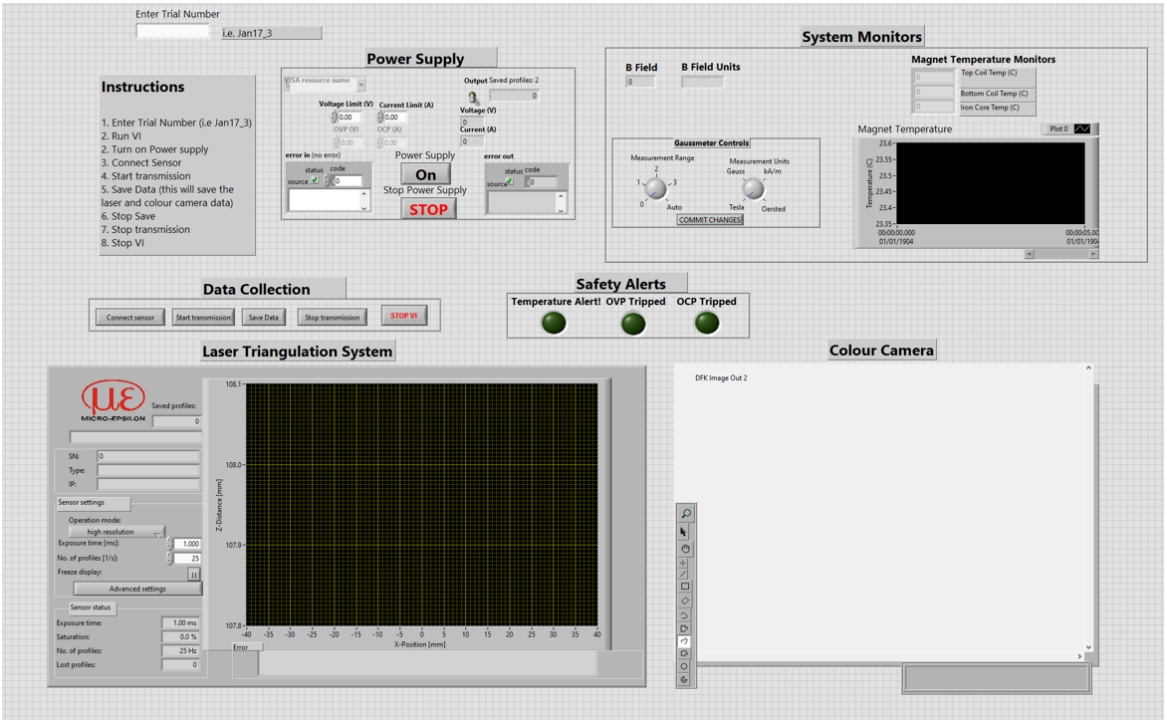


Figure 3.14: Labview set up for data capture and system monitoring.

To interface between the electromagnet and Labview, a National Instruments cDAQ-9174 was utilised with a NI 9210 mini thermocouple module to read thermocouple temperatures and a NI 9482 SPST Relay Module to shut down the power supply if a safety concern was triggered.

3.4 Looking to the Future: Experimental Incorporation of TEMHD Effects

In order for TEMHD effects to be viewed, the magnetic field must be oriented in the toroidal configuration and a temperature gradient must be imposed vertically from the bottom liquid metal interface to the liquid metal free surface. The thermoelectric current will then be generated by the difference in seebeck coefficient between galinstan and the metal channel.

To measure these TEMHD effects, a temperature gradient must be imposed and monitored on the system. A simplified thermal model, neglecting MHD effects, was generated to optimise the set up to include TEMHD effects using ANSYS Mechanical [8].

[8] ANSYS Mechanical is a finite element analysis tool.

From preliminary ANSYS CFX modelling, it was determined that a 220 W heater paired with dry ice could be utilised to generate the necessary temperature gradient. A 75 x 70 mm heater would be drilled into the back of the liquid metal channel channel and run at full power to heat the bottom interface of the liquid metal. Dry ice would used to cool the liquid metal storage tank reservoir and to cool the channel walls to facilitate the formation of a temperature gradient in the galinstan film. According to the model, this set up should generate a 25°C temperature difference across a 10 mm thick film, which corresponds to a 2500 K/m temperature gradient. For reference, a temperature gradient on the order of 10^3 K/m is projected for a thin lithium flowing over a molybdenum divertor on the National Spherical Torus Experiment fusion device, which aligns well with the temperature gradient suggested here (107).

The channel width selected for the work in this thesis was chosen to be compatible for future use in TEMHD experiments. For typical TEMHD experiments involving lithium, a 2 mm wide channel was used (108). However, the laser triangulation system used in this thesis for data collection suffered from severe interreflections between the liquid metal surface and adjacent metal channel walls when the channel width was less than 20 mm. TEMHD effects are produced from circulated electrical currents generated in the side wall boundary layer region of the flow, so the channel width must be kept to a minimum so that the boundary layer activity can propagate to the bulk flow region. Equation 3.5 shows the analytical solution for average velocity, U_{avg}, in response to TEMHD effects, derived by Shercliff (109). Fluid parameters for lithium and galinstan were listed in Table 3.1.

$$U_{avg} = \frac{Ha - tanh(Ha)}{Ha + Ctanh(Ha)} \left(\frac{S - S_w}{B} \frac{dT}{dy} - \frac{1 + C}{\sigma B^2} \frac{dP}{dz} \right) \tag{3.5}$$

Galinstan has a viscosity that is 100 times greater than lithium, and a higher viscosity translates to a larger boundary layer region which means a wider channel can still experience TEMHD effects in the bulk flow region (41). This is evident from Figure 3.15, where the average velocity over a range of toroidal magnetic field values is plotted using Equation 3.5 and the experimental parameters listed in Table 3.2. TEMHD drive is negligible for lithium flow in a 25 mm wide channel and present for galinstan flow in that same channel. For these

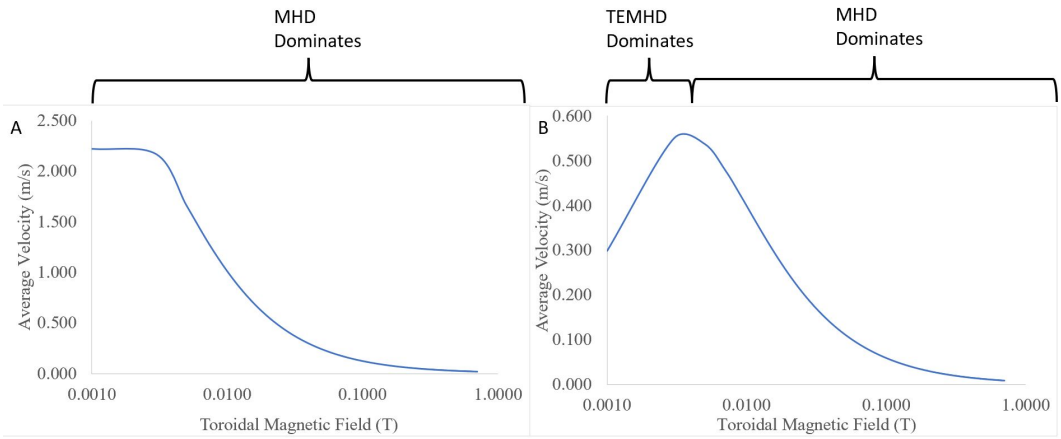


Figure 3.15: Comparison curve showing average velocity as a function of toroidal magnetic field for a 20 mm wide channel for A) lithium and B) galinstan, assuming a temperature gradient of 2500 K/m, Seebeck coefficients of 2.5e-5 V/K for lithium and 1.24e-5 for galinstan, and no pressure gradient. A stainless steel channel was used.

reasons, a 25 mm wide channel was used in the present study to allow for the current MHD experiments and potential future TEMHD experiments.

3.5 Looking to the Future: Liquid Metal Velocity Tracking Technique Development

To gain a comprehensive understanding of liquid metal flow, it is useful to have both height and velocity measurements available. Velocity measurements are inherently more complex to gather because velocity values vary both laterally across the liquid metal surface and vertically through the liquid metal height. As described in Section 5.4, galinstan and other liquid metals tend not to uniformly wet surfaces, meaning velocity profiles across a surface can vary dramatically depending on amount of wetting.

Two non-invasive methods to measure liquid metal velocities have been reported in the literature. Ultrasound doppler velocimetry methods have been used to measure liquid metal velocities, but this technology is prohibitively expensive and is limited to films greater than 3 mm in height (110). At the PPPL, surface oxides tracking using an infrared (IR) camera has been shown to provide accurate measures of galinstan surface velocity, but no measurements of velocity below the surface can be made (80). In the IR, galinstan impurities have emissiv-

ity's ranging from 0.73 to 0.99, and galinstan has emissivity of 0.04, so galinstan impurities are easily distinguishable using an IR camera. Surface oxides have been shown to form on galinstan in environments with less than 1ppm oxygen content (111).

In this section, several methods for measuring thin film liquid metal velocity were explored with the aim of developing an inexpensive method to measure bulk and surface velocities of liquid metal flow.

Overview of Explored Methods

As galinstan is completely opaque, optical methods for velocity tracking can only be applied to the surface. In the situation of a fully wetted channel, an estimate of average velocity can be made by dividing the volumetric flow rate by the fluid's cross sectional area. However, in most cases the liquid metal does not fully wet the channel surface, so flow area cannot be accurately estimated.

Several methods to measure liquid metal velocity were explored by the author and summarized in Figure 3.16. In short, six tracking mediums were explored:

1. 300 μm diameter fluorescent microspheres
2. 1000 μm diameter stainless steel microspheres
3. Air/Argon bubbles
4. Heat (or cold) pulses
5. Frozen galinstan/gallium particles
6. Surface oxides

The following optical instruments were available for use:

1. DFK 33UP5000 CMOS camera with 8 mm lens
2. Micro Epsilon TIM40 infrared (IR) camera
3. Micro Epsilon ScanControl LLT3000-50/BL laser triangulation system

Velocity measurements can be deduced from the IR and visual camera data using cross-correlation algorithms by tracking a visible particle present on the fluid surface. The ScanControl system has the potential to provide velocity measurements by measuring the surface height, which changes as the particle moves. It is reasonable to assume that a particle partially submerged in the liquid metal will provide a representative bulk velocity measurement (see Figure 3.17).

Tracking Medium	Compatibility with Galinstan	Visual Camera	Infrared Camera	ScanControl Laser Triangulation
Fluorescent microspheres (300 micron diameter)	Immiscible with galinstan	Fluorescent microspheres move with the galinstan surface and are visible through use of the UV torch	Fluorescent microspheres are visually distinct in the IR due to difference in emissivity from galinstan	Fluorescent microspheres can be tracked on the surface, but noisy specular signal hinders this
Stainless steel microspheres (1000 micron diameter)	Immiscible with galinstan and clogs the pump	Microspheres move with the galinstan surface	Microspheres visually distinct in the IR due to difference in emissivity from galinstan	Can be tracked on the surface, but there is significant noise
Argon Bubble tracking	Difficult to form in galinstan	Bubbles move with the galinstan surface	Not Yet Tested	Not Yet Tested
Frozen gallium particles (1000 micron)	Galinstan mixes well with itself	Particles move with the galinstan surface	Visually distinct in the IR	Can be tracked on the surface if only partially submerged
Heat Pulses	Can be applied to liquid galinstan (though high surface reflectivity of galinstan must be considered)	No visual difference for hot/cold surface spots in liquid galinstan	In absence of oxidised galinstan surface, temperature gradients are not visible in the IR	No change in depth occurs
Surface oxide tracking	Increases the viscosity of galinstan and causes stagnant surface flow	Somewhat visible in the visual spectrum	Visually distinct in the IR	No trackable change in depth occurs

Figure 3.16: Matrix of possible optical velocity measurement combinations. Red signifies system incompatibility. Yellow signifies slight or possible compatibility. Green signifies system compatibility.

After determining which mediums could be reliably tracked, compatibility of the tracking medium with galinstan and the flow loop were considered. Permanently solid media (fluorescent microspheres and stainless steel spheres) were consistently trapped in the gear shaft of the pump, causing pump failure. Adding and removing these particles after each cycle

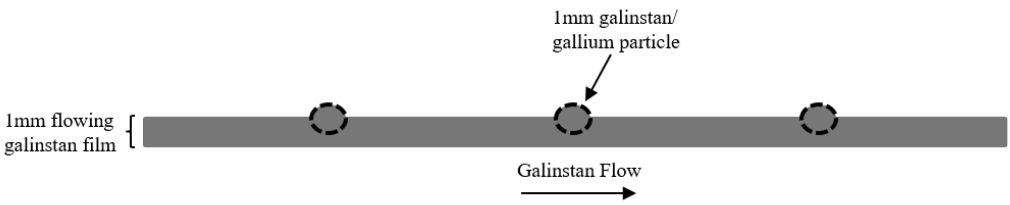


Figure 3.17: Diagram of partially embedded, 1 mm galinstan or gallium particles flowing in a 1 mm galinstan film.

was not sustainable, so these methods were not further pursued. The high surface tension of the galinstan film prevented embedding of stainless steel particles in the flow, although stainless steel particles were more dense than galinstan. This prevented any bulk measure of velocity to occur. Attempts were made to create air bubbles within the galinstan flow to measure bulk velocity, but a method to sustain the bubble along the channel length was not determined.

This leaves surface oxide tracking, heat pulse tracking, and frozen galinstan/gallium particle tracking as the remaining methods to explore.

The measurement of surface velocity using surface oxides was explored successfully at PPPL using an IR camera (80). This stands as a promising method to track liquid metal surface velocities, although the creation and placement of surface oxides cannot be easily controlled so the quantity of measurements would be limited.

Appendix B details efforts to manufacture galinstan and gallium particles and attempts to use these particles to measure bulk galinstan flow velocities. This work was completed by James Leader, under supervision of the author of this thesis. For this reason, it is included in the Appendix rather than in the main text. From this study, it was determined that frozen galinstan particles could be manufactured and tracked with an IR camera, visual camera and using the ScanControl laser triangulation system. Frozen gallium and galinstan particles were distinguishable from liquid galinstan in the IR, though it was unclear if this is due to surface oxidation/finish or actual temperature difference.

Finally, the measurement of velocity through tracking of heat pulses was explored by Ruzic (112) using lithium. In his experiment, 1.5 kW electron beam power was applied

to liquid lithium in LiMIT style trenches under 0.0589 T magnetic field. The velocity of the liquid lithium was measured both using a monochrome Canon SX200IS camera with 25 frames/second frame rate and an Inframetrics 760 IR camera. The monochrome camera captured velocity measurements using particle velocimetry for seeded lithium oxide particles. The IR camera estimated the average velocity using the inlet and outlet temperature difference and a heat balance (see equation 3.6), where p is absorbed power for one trench, C_p is lithium heat capacity, h is trench height, and w is trench width. This equation assumes that heat from the electron beam is transferred convectively down the trench and the trench bottom is around 0 .

$$u = \frac{2p}{\rho C_p h w \frac{\partial T}{\partial z}} \tag{3.6}$$

An alternative to tracking heat from the surface could be tracking heat from the plate surface (assuming a reasonably thin liquid metal film). This could be useful in scenarios where visual access to the liquid metal surface are limited. An experimental set up was developed at OTI to explore this heat tracking method using galinstan (Figures 3.18 and 3.19).

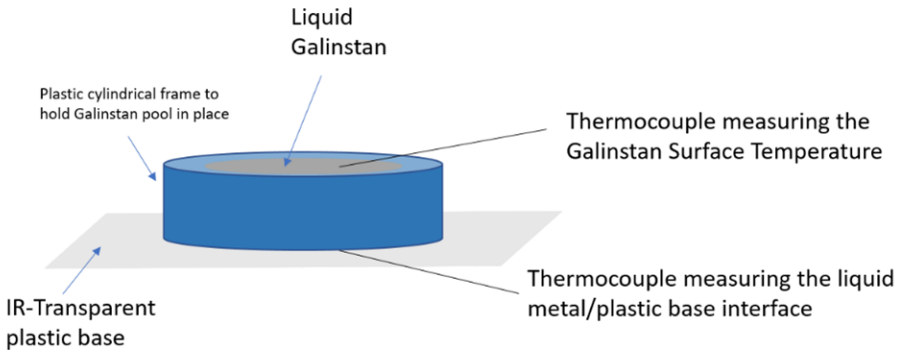


Figure 3.18: Experimental set up for galinstan heat tracking studies

The set up involved a static 2 mm pool of galinstan placed in a plastic, 60 mm diameter cylindrical frame. Heat pulses were added to the static pool by pipetting heated galinstan from a set distance from the liquid metal pool surface.

The pool of galinstan was supported underneath by an IR transparent window material.

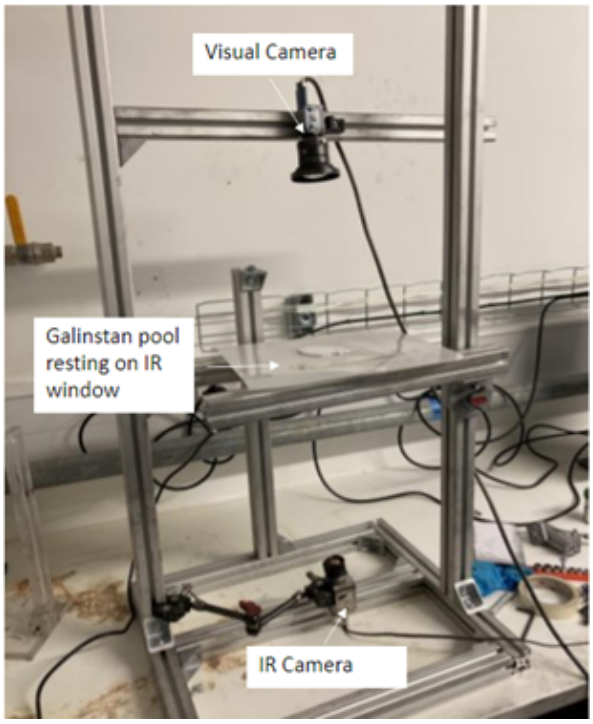


Figure 3.19: Heat tracking experimental set up.

The IR camera was set up 30 mm from the base and measures the temperature of the IR-transparent plastic base. This set up allowed for the observation of temperature changes from the bottom of a free surface pool of liquid metal.

Data from this experiment suggested that heat (or cold) pulses could be tracked using an array of thermocouples on the surface of the channel, as temperature pulses were clearly visible in the IR. When a drop of liquid 15°C warmer than ambient was pipetted on the pool surface, a 1°C temperature change was measured on the IR at the location of the drop.

These experiments suggested that a 2D array of thermocouples placed near the channel surface could reliably track the movement of a heat pulse moving down the channel. Future work could include integration of an array of thermocouples on the channel surface to track heat (or cold) pulses applied to flowing liquid metal. This change in temperature would migrate from the flowing liquid metal surface to the liquid metal-channel interface. The movement of heat profiled from the thermocouples could be related to the galinstan flow velocity, given high enough thermal resolution and small enough time response for the thermocouples. Future work should investigate this as a method for velocity tracking.

To further confirm this, an experiment involving hot or cold pulses generated in a non-

invasive manner (i.e. not droplets) should be devised. This would likely involve a laser point source. The low emissivity of liquid metal surfaces must be kept in mind when choosing a suitable laser power, as only a fraction of the incident laser power will be absorbed by the liquid metal. This issue was avoided in the current experimental set up as heat transfer was facilitated through gravity-driven mass transfer of hot or cold liquid metal. From preliminary numerical simulations, a laser source on the order of 1 MW would likely be required to witness temperature changes on the channel surface on the order of one degree. This adds significant safety requirements to prevent user eye damage and unwanted laser beam redirection from the specular liquid metal surface. Also, additional experimentation is required to understand the thermocouple response time needed to accurately track temperature changes when the galinstan is flowing. If the thermocouple response time is too low, then the moving heat pulse will not be registered by the thermocouple array.

From this survey, it is proposed that liquid metal surface flow would be best measured using surface oxides, and bulk measurements might be possible with frozen lithium particles or from heat tracking. Future work should investigate incorporating one of these methods into the experimental set up to increase the amount of information produced on the OLME.

3.6 Summary

In conclusion, this chapter detailed the design and development of the OLME at the University of Oxford to quantitatively measure the impact of magnetic field on liquid metal height for galinstan free surface flow. The design and modelling of a bespoke electromagnet to generate uniform magnetic fields was described, along with the safety measures in place to ensure safe operation of this new facility. The final two sections present suggested improvements to the facility to incorporate the measurement of velocity and TEMHD effects.

Chapter 4

ANALYTICAL AND NUMERICAL MODELLING OF LIQUID METAL FLOW

4.1 Analytical and Numerical Modelling Approach

A numerical model of liquid metal flow under MHD conditions was developed using ANSYS CFX. The purpose was to ease future iteration of PFC component design and to provide additional insight on the behaviour of liquid metal flow beyond the capabilities of the experimental facility.

Computational Fluid Dynamics (CFD) is a useful tool for numerically solving fluid flow problems efficiently. CFD is often used to expedite the engineering design process by allowing for rapid prototype testing (113). For this thesis, a CFD model is developed alongside the experimental work to allow for further generalisation of results and as an aid for adapting the findings of this research to more complex, reactor-relevant scenarios in the future. This also aids in understanding of phenomena that currently cannot easily be measured experimentally, such as the velocity profile along the fluid height and the generation of induced MHD currents. Additionally, 2D duct flow modelling is essential in the development of efficient breeder blankets (114).

The numerical modelling of liquid metal MHD flow in fusion relevant magnetic fields has improved significantly from the first MHD code developed in 1971 (114). Over time, analysis of flows at higher Hartmann numbers (see Equation 4.1) became possible, representing increasingly larger magnetic fields. In this equation, ρ represents the fluid density, and ν represents kinematic viscosity. Advancements in parallel computing have allowed for increasingly finer mesh structures that better capture MHD behaviour in the Hartmann and Shercliff boundary layers (115), as well as the effect of MHD on free surface flow (46).

$$Ha = \frac{1}{2}BL\sqrt{\frac{\sigma}{\rho\nu}} \tag{4.1}$$

Several commercial and open source CFD codes exist, including ANSYS FLUENT, ANSYS CFX, COMSOL, and OpenFOAM (116). Most liquid metal MHD codes have been developed to model duct flow in the blanket region of a fusion device and were validated through comparison to analytical solutions (114). There is a significant need for free surface numerical studies validated by experimental data.

This thesis seeks to develop an ANSYS CFX model of the Oxford Liquid Metal Experiment (OLME) representing free surface flow in the presence of a surface normal magnetic field. This chapter details the development of the numerical model and compares the results of this numerical model to existing analytic solutions. The chapter begins with an overview of the ANSYS MHD solver theory, followed by several validation cases where numerical results for fully developed flow are compared to established theoretical solutions from Hunt, Shishko, and Miyazaki to support the use of this solver (41, 42, 43). Then, a novel analytical solution is presented for MHD free surface flow, based on a solution recently presented by Sun (45), and used to validate a numerical model of a free surface, developing flow in the presence of surface normal magnetic field. In the following chapters, the numerical results generated by the developing flow model are compared to the experimental data to illustrate the practical relevance of this model for future PFC design and testing.

4.1.1 ANSYS CFX MHD Solver Theory

ANSYS CFX is a numerical fluid dynamics software that utilises a finite volume technique to model momentum, heat and mass transfer using the Navier-Stokes equation (117).

There are three methods frequently used to incorporate MHD equations into the Navier-Stokes equation in CFD solvers:

1. Magnetic Vector Potential (MVP)
2. Electric Potential (EP)
3. Magnetic Induction (MI)

These three methods mainly differ in the formulation used to solve for induced magnetic field. ANSYS CFX has two, built-in MHD solvers which can incorporate either the MVP or EP method. For MVP and EP, the electric potential equation, derived later in this chapter as Equation 4.7, is introduced and current density is calculated using Ohms law. The electric potential method is a modified version of the magnetic vector potential method which neglects induced magnetic field- an appropriate assumption for low magnetic Reynolds number. For the experiments conducted in this thesis, the magnetic Reynolds number is much less than one, which allows for induced magnetic fields to be ignored (32).

The magnetic induction method utilises Ohms law and Maxwell's equations to solve for induced magnetic field. This method assumes a constant electrical conductivity, which is not applicable for free surface flow due to the large jump in electrical conductivity at the free surface interface. For this thesis, the electric potential method is used due to the low magnetic Reynolds number and amenability to free surfaces.

Electric Potential Formulation

The electric scalar potential (φ) is introduced as Equation 4.2, where $\vec{A}$ represents the magnetic vector potential and t represents time.

$$\vec{E} = -\nabla\varphi - \frac{\partial \vec{A}}{\partial t} \tag{4.2}$$

This formulation was simplified for static magnetic field to yield:

$$\vec{E} = -\nabla\varphi \tag{4.3}$$

Ohms law was used to define the current density:

$$\vec{j} = \sigma(\vec{E} + \vec{U} \times \vec{B}) \tag{4.4}$$

Substituting 4.3 into Ohms law produced:

$$\vec{j} = \sigma(-\nabla\varphi + \vec{U} \times \vec{B}) \tag{4.5}$$

The principle of current conservation was included as:

$$\nabla \cdot \vec{j} = 0 \tag{4.6}$$

Equations 4.6 and 4.5 were combined to yield the final electric potential equation:

$$\nabla^2\vec{\varphi} = \nabla \cdot (\vec{U} \times \vec{B}) \tag{4.7}$$

Finally, the Lorentz Force, $\vec{F}_{mag}$ (Equation 4.8), was incorporated into the Navier-Stokes equation (Equation 4.9) as a source term, and momentum was conserved (Equation 4.10):

$$\vec{F}_{mag} = \vec{j} \times \vec{B} \tag{4.8}$$

$$\frac{\partial\rho\vec{U}}{\partial t} + \rho(\vec{U} \cdot \vec{\nabla})\vec{U} = -\nabla P + \mu\nabla^2\vec{U} + \vec{F}_{mag} + \vec{C}_{fmag} + \rho f_{ext} \tag{4.9}$$

$$\frac{\partial\rho}{\partial t} + \vec{\nabla} \cdot (\rho\vec{U}) = 0 \tag{4.10}$$

Here, P represents pressure, $\vec{C}_{fmag}$ represents the momentum source term (described in Section 4.2.1.1), and f_{ext} represents other external forces (0 for this work)

Equation Summary

To summarise, this problem consisted of five governing equations and five variable to solve for. There was one equation for electric potential (Equation 4.11), three Navier Stokes Equations representing the x,y, and z momentum components (Equation 4.12), and one for conservation of mass (Equation 4.13), which were used to solve for electric potential, fluid velocity (x, y and z components), and pressure. This thesis focuses on laminar flow across a horizontal surface, so the gravitational force is not included.

$$\nabla^2 \vec{\varphi} = \nabla \cdot (\vec{U} \times \vec{B}) \tag{4.11}$$

$$\frac{\partial \rho \vec{U}}{\partial t} + \rho(\vec{U} \cdot \vec{\nabla})\vec{U} = -\nabla P + \mu \nabla^2 \vec{U} + \sigma(-\nabla \varphi + \vec{U} \times \vec{B}) \times \vec{B} + \vec{C}_{fmag} \tag{4.12}$$

$$\frac{\partial \rho}{\partial t} + \vec{\nabla} \cdot (\rho \vec{U}) = 0 \tag{4.13}$$

4.1.1.1 Boundary Conditions

For the simulations described in the following section, we assumed steady state and incompressible flow.

$$\rho = constant \tag{4.14}$$

$$\frac{\partial \vec{U}}{\partial t} = 0 \tag{4.15}$$

$$\frac{\partial P}{\partial z} = constant \tag{4.16}$$

The walls have the following boundary conditions:

$$\vec{U}_{wall} = 0 \tag{4.17}$$

$$\frac{\partial \vec{\varphi_{wall}}}{\partial \vec{n}} = 0 \tag{4.18}$$

Here, $\vec{n}$ represents the unit vector perpendicular to the wall

4.1.2 Numerical Modelling Overview

When liquid metal flows perpendicular to a magnetic field, recirculating current lines are induced in the plane perpendicular to the flow direction, as illustrated in Figure 4.1. In the case of non conducting walls, the current lines must return through the fluid boundary layers. The Hartmann and Shercliff boundary layers exists on the duct walls perpendicular and parallel, respectively, to the external magnetic field. The core velocity profile for MHD flow is flat in the presence of a strong magnetic field, and the variation in velocity from the walls to this core flow region is defined as the Hartmann boundary layer when along a wall perpendicular to the magnetic field and Shercliff boundary layer when along a wall parallel to the magnetic field. The overall thickness of Hartmann boundary layers is inversely proportional to the Hartmann number, and the overall thickness of the Shercliff boundary layers is inversely proportional to the square root of the Hartmann number.

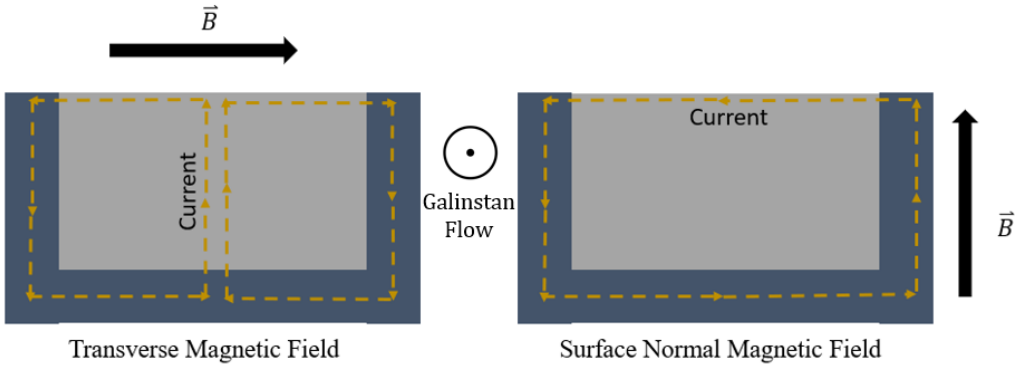


Figure 4.1: Illustration (not to scale) of electric current lines in the case of conductive substrate and walls for transverse magnetic field and surface normal magnetic field. The blue area represents the channel walls, the grey area represents the fluid, and the yellow represents the current path.

To foster confidence in the use of ANSYS CFX for numerical modeling of liquid metal MHD, four test cases were compared with established analytical solutions:

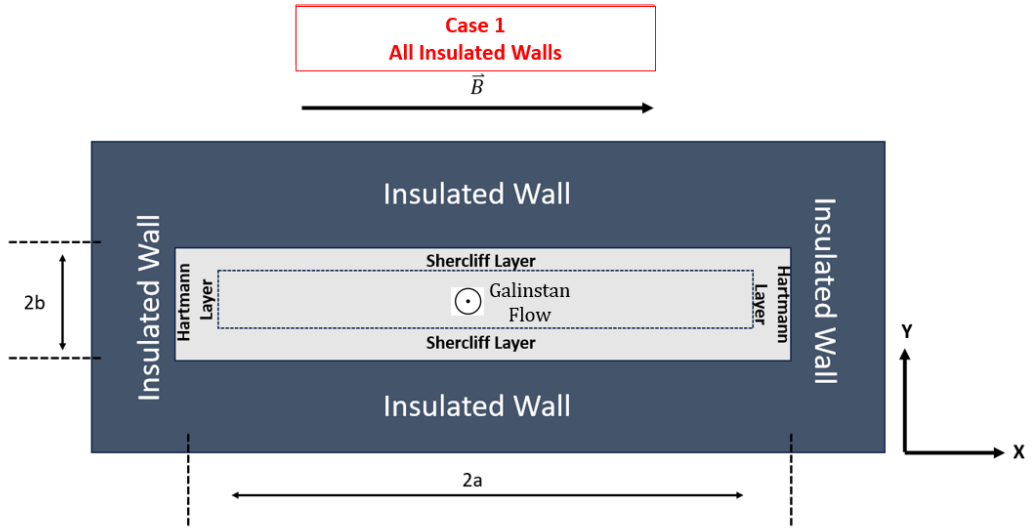


Figure 4.2: Illustration (not to scale) of liquid metal duct flow through insulated walls in the presence of transverse magnetic field. The location of Hartmann and Shercliff layers are shown.

- **Case 1:** Duct flow with all insulated walls in the presence of a transverse magnetic field (See Figure 4.2).
- **Case 2:** Duct flow with conductive Hartmann walls and insulated Shercliff walls in the presence of a transverse magnetic field (See Figure 4.3).
- **Case 3 (a):** Free surface flow with all conductive walls, in the presence of a transverse magnetic field (See Figure 4.4).
- **Case 3 (b):** Free surface flow with all conductive walls, in the presence of a surface normal magnetic field (See Figure 4.5).

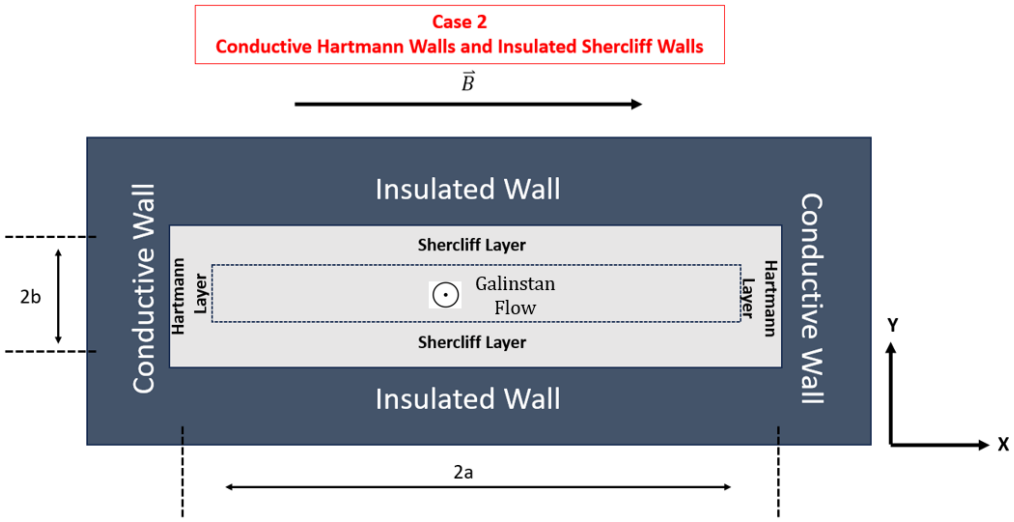


Figure 4.3: Illustration (not to scale) of liquid metal duct flow through conductive Hartmann walls and insulated Shercliff walls in the presence of transverse magnetic field. The location of Hartmann and Shercliff layers are shown

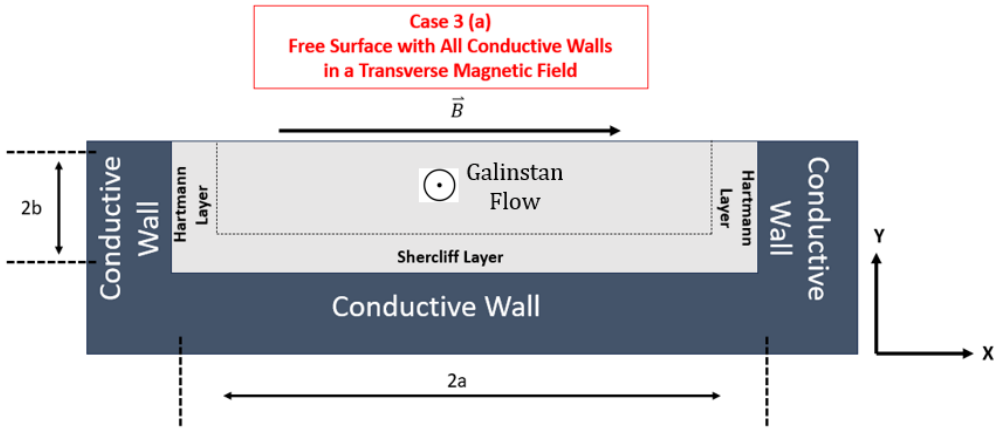


Figure 4.4: Illustration (not to scale) of free surface, liquid metal flow through all conductive walls in the presence of a transverse magnetic field. The location of Hartmann and Shercliff layers are shown

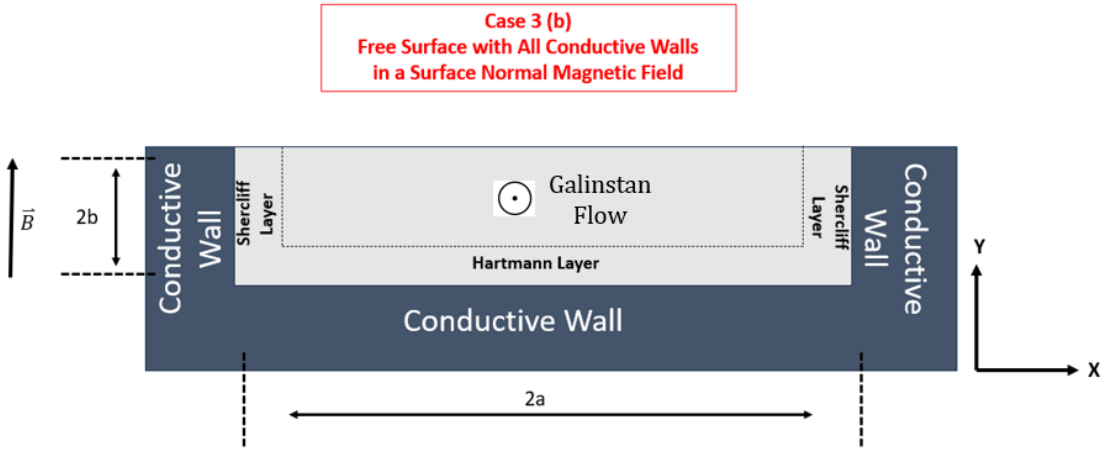


Figure 4.5: Illustration (not to scale) of free surface, liquid metal flow through all conductive walls in the presence of a surface normal magnetic field. The location of Hartmann and Shercliff layers are shown

All cases were run with a unidirectional magnetic field located in either the transverse, x, or surface normal, y, direction, relative to the fluid flow, through the z plane.

The results from the first two cases were compared to analytical solutions for liquid metal flow derived by Hunt (41), as suggested by Khodak (63). Both employ a transverse magnetic field. To better simulate the free surface experiments, case 3 was completed to validate the solvers ability to model a free surface in the presence of either a surface normal or transverse magnetic field. Shishko (43) provided an analytical solution for free surface flow in the presence of a transverse magnetic field. Miyazaki (42) provided a solution for duct flow with all conductive walls in the presence of a uni directional magnetic field. Free surface flow in the presence of a surface normal field was approximated by adapting the Miyazaki solution using a symmetry condition.

The ANSYS MHD solver has been validated for square geometries where the aspect ratio (the ratio of of the channel height to the channel width) is one (114), however, this geometry is not representative of the low aspect ratio flow geometries that often occurs in a fusion device. The validation study presented here utilised a low aspect ratio flow geometry to be representative of experiments performed on the OLME. Through this process, challenges in low aspect ratio numerical and analytical modelling were revealed and explored to improve the accuracy of these solutions in fusion relevant conditions.

Table 4.1: Model parameters input to ANSYS CFX

Symbol	Definition	Value
$\vec{B}$	Magnetic Field (T)	0.16 T
a	half fluid width	0.0125 m
w	full fluid width	0.025 m
b	half fluid height	0.001m
h	full fluid height	0.002 m
t	wall thickness	0.003 m
ν	fluid kinematic viscosity	3.75×10^{-7} m^2/s
ρ	fluid density	6440 kg/m^3
σ_{fluid}	fluid electrical conductivity	3.46×10^6 S/m
σ_{wall}	Wall electrical conductivity	5.998×10^7 S/m
dP/dz	Pressure Gradient	-661.57 Pa/m

A 2D model was developed describing liquid metal flow through a 25 mm x 2 mm rectangular duct with unidirectional magnetic field, to model the experimental set up. The mesh was one cell thick in the z direction to simulate a 2D case. To simulate steady, 2D flow in CFX, the fluid domain was modelled with translational periodicity and a 1:1 mesh (further described in section 4.1.2.1) between the inlet to outlet face. Galinstan was used as the working fluid, and a 661.57 Pa/m pressure gradient was imposed as a momentum source term to model a 0.6° channel angle (α). A low channel angle was chosen as an intermediate between the flat channel angle experimentally tested in this experiment and suggested future experiments at low angles. The relationship between channel angle and pressure gradient is described in Equation 4.19, where α represents flow angle and g represents gravity. Relevant parameters input to the model are shown in Table 4.1 and were chosen to approximate the experimental set up.

$$\frac{dP}{dz} = \rho g \sin\alpha \tag{4.19}$$

The non-dimensional flow rate, $\tilde{Q}$, (Equation 4.20) was used to compare numerical simulations to analytical solutions rather than flow velocity because flow rate is an integral quantity, meaning its value representative of the entire domain (114). In this equation, $\tilde{x} = \frac{x}{a}$ and $\tilde{y} = \frac{y}{b}$. In this thesis, dimensionless variables are notated with a tilde.

$$\tilde{Q} = \int_{-1}^{1} d\tilde{y} \int_{-1}^{1} \tilde{U} d\tilde{x} \tag{4.20}$$

$$\tilde{U} = \frac{\rho \nu U}{a^2 \left(-\frac{\partial p}{\partial z}\right)} \tag{4.21}$$

The simulation was run until $\tilde{Q}$ averaged over the liquid domain had achieved steady state described by the convergence criteria described in Equation 4.22 (114).

$$\left| \frac{\tilde{Q}^{n+1} - \tilde{Q}^{n}}{\tilde{Q}^{n}} \right| < 10^{-10} \tag{4.22}$$

Considering the magnetic field and geometry of the OLME, a Hartmann number of approximately 76 was representative. The characteristic length, L, used in the Hartmann number equation was half of the wall length parallel to the magnetic field direction. So for a transverse magnetic field, oriented in the x direction, this characteristic length was a, and for a surface normal magnetic field, oriented in the y direction, this characteristic length was b. Numerical simulations were performed on an Intel(R) Core(TM) i9-7920X CPU at 2.90GHz with 32 GB RAM with additional computing resources provided by the Advanced Research Computing facility at the University of Oxford.

To quantify the accuracy of the solver, the numerical results were compared to the analytical solutions for each case. Final results are reported as the percent difference between $\tilde{Q}_{analytical}$ and $\tilde{Q}_{numerical}$. The percent difference is calculated as:

$$PercentDifference = \frac{\tilde{Q}_{analytical} - \tilde{Q}_{numerical}}{\tilde{Q}_{analytical}} \times 100 \tag{4.23}$$

4.1.2.1 Mesh Sensitivity Analysis

A mesh with fine refinement near the Hartmann and Shercliff boundary layers was utilised to capture the boundary layer dynamics. Two factors were used to describe the mesh, number of divisions and bias factor. The same number of divisions was used along both Hartmann and Shercliff walls to ensure both boundary layer and bulk flow dynamics were captured. A

baseline of 100 divisions was used as suggested by Khodak (63). The bias factor determined the spacing of the divisions. Bias factor of one represented evenly spaced divisions and increasing the bias factor generated meshes where the division lengths gradually reduced in the direction specified. For these simulations, the bias factor direction was set such that the divisions reduced in size closer to the walls to better capture boundary layer physics.

A mesh sensitivity analysis was run to determine the optimum number of divisions. An upper limit on mesh refinement was determined when doubling the number of divisions changes the solution by less than 1%. The number of divisions on the Hartmann walls was divided by the geometric aspect ratio to determine the number of divisions for the Shercliff walls. A bias factor of 10 was used for all runs.

During the mesh sensitivity analysis, the key parameter of interest, $\tilde{Q}$, was utilised for comparison. The simulations were run until this variable converges within the guidelines specified earlier in this report. Results are shown for mesh divisions in Figures 4.6, where the dimensionless flow rate was plotted against total number of mesh elements. We found the optimal number of mesh divisions was 20 on the short edges and 250 on the long edges. Doubling the number of divisions changed the solution by 0.453%, which confirmed the solver has achieved convergence. The optimal generated mesh is found in Figure 4.7.

The following sections detail the analytical solutions for each case, followed by analysis of the the numerical results.

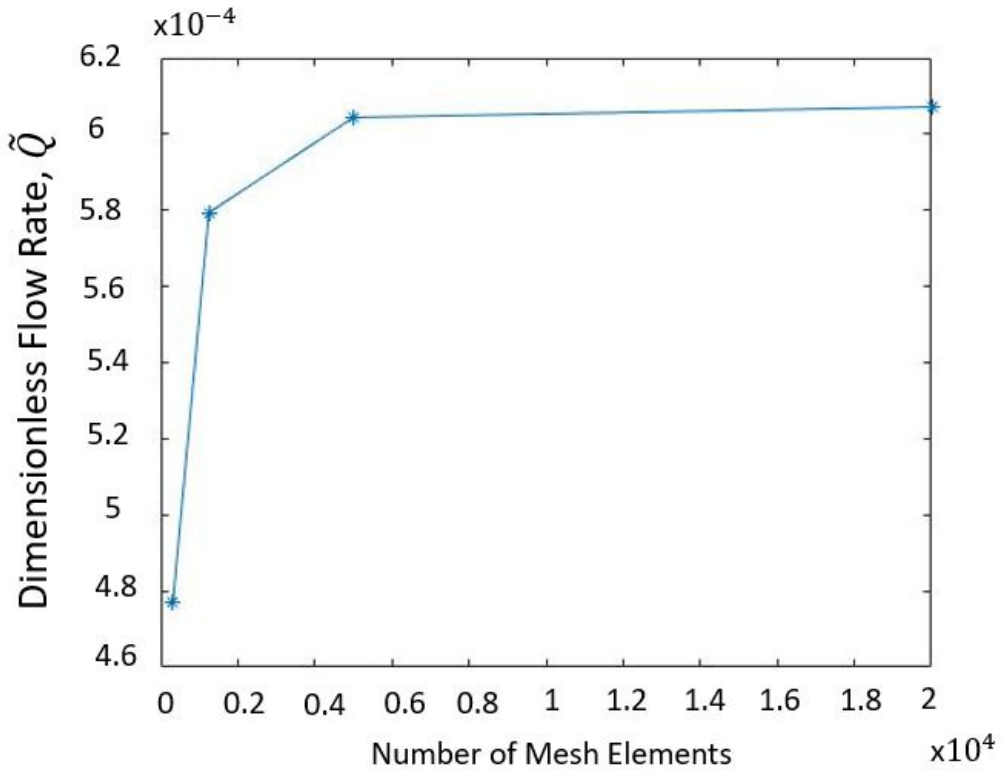


Figure 4.6: Mesh sensitivity analysis results for Hartmann number 76 run for duct flow with non conductive walls.

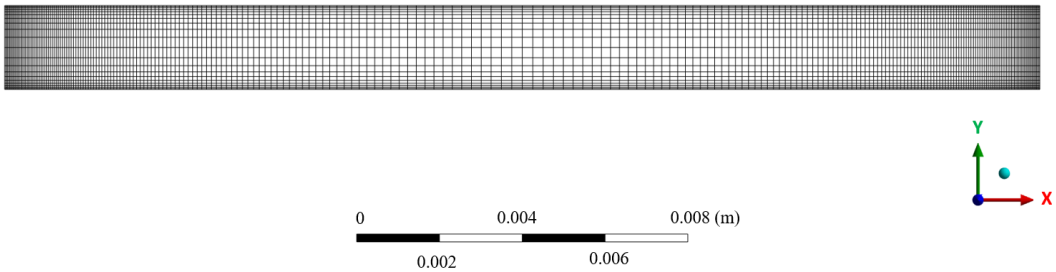


Figure 4.7: Optimum mesh generated for the insulated walls case with Hartmann number 76.

4.2 Benchmarking for Fully Developed MHD Flow

4.2.1 Validation Cases

4.2.1.1 2D Duct Flow with Non Conducting Walls and Transverse Magnetic Field

The case of fully developed duct flow with insulated walls is traditionally validated against the 1953 Shercliff analytical solution (39). In addition to a full solution, Shercliff provided a simplified solution for fully developed flow with insulated walls that works well for approximating MHD behaviour in a square channel in comparison to numerical solutions (63). This simplified solution is presented as Equation 4.24, where μ is dynamic viscosity.

$$U = \frac{a^2}{\mu Ha}\frac{dP}{dz}\left(1 - \frac{0.852}{\sqrt{Ha}}\frac{a}{b} - \frac{1}{Ha}\right) \tag{4.24}$$

Though this convenient equation works well for a square channel, it was found that the approximations do not hold for low aspect ratio geometries or problems with low Hartmann numbers. Accordingly, the full solution must be used for the work described in this thesis. Building from the work of Shercliff, Hunt in 1964 developed a solution for fully developed MHD duct flow that is accurate for both insulated and conductive walls. This solution reduced to the full Shercliff solution in the case of insulated walls, and was used here to validate the numerical model.

The analytical solution for this scenario was defined by Hunt in (41) as case two (see Equation 4.25). Here, k is the summation index, ξ is x/a, η is y/a, and σ_{solid} is the duct wall electrical conductivity. The thickness of the duct walls, shown in Table 4.1, was chosen so that the conductivity ratio, c_w, was 0.08.

$$\begin{aligned} U = \sum_{k=0}^{\infty} \frac{2(-1)^k cos(\alpha_k)\xi}{\frac{a}{b}\alpha_k^3} [1 - \\ \frac{(1+tanh(r_{2k}/c_w r_{2k}))cosh(r_{1k}\eta)}{cosh(r_{1k})(Ha^2+4\alpha_k^2)^{1/2}/r_{2k} + sinh(r_{1k}+r_{2k})/c_w r_{2k} coshr_{2k}} - \\ \frac{(1+tanh(r_{1k}/c_w r_{1k}))cosh(r_{2k}\eta)}{cosh(r_{2k})(Ha^2+4\alpha_k^2)^{1/2}/r_{1k} + sinh(r_{1k}+r_{1k})/c_w r_{2k} coshr_{1k}}] \end{aligned} \tag{4.25}$$

Table 4.2: Benchmarking Results for Duct Flow Through Non Conductive Walls.

Hartmann Number	$\tilde{Q}_{analytical}$	$\tilde{Q}_{numerical}$	**Percent Difference**
76	0.00060785	0.00058949	3.11

$$\alpha_k = \frac{(k+1/2)\pi}{\frac{a}{b}} \tag{4.26}$$

$$r_1 k = 0.5\left(Ha + Ha^2 + 4\alpha_k^2)^{1/2}\right) \tag{4.27}$$

$$r_2 k = 0.5\left(-Ha + Ha^2 + 4\alpha_k^2)^{1/2}\right) \tag{4.28}$$

$$c_w = \frac{t\sigma_{fluid}}{a\sigma_{solid}} \tag{4.29}$$

For Hartmann numbers below 120, convergence of the summation of Equation 4.25 occurred around k = 100,0000. Table 4.2 presents results from this validation case.

Four modifications were made to the built in MHD solver in order to facilitate a more accurate solution and better convergence. The first modification dealt with the numerical scheme used to solve the Navier Stokes equation. In CFD, equations can be solved explicitly or implicitly. An explicit scheme calculates the solution for each iteration based on values generated from the previous iteration. An implicit scheme involves solving a system of equations to solve for the dependant variables at each iteration. While an explicit scheme is easier to solve, this scheme often requires very small timescales to facilitate convergence. The implicit scheme requires more computing time per iteration, but yields better convergence and can handle larger timesteps.

Ansys CFX used an implicit scheme to solve the Navier Stokes equation for fluid flow problems in the absence of magnetic field. However, an explicit scheme was used for MHD problems to calculate the Lorentz force component of the Navier Stokes equation which inhibited convergence. To allow for implicit treatment of the Lorentz force component, a momentum source term coefficient, $(\vec{C}_{fmag})$ was included to facilitate convergence, as sugges-

ted by Khodak(63). This momentum source term was determined by expanding the Lorentz force (Equation 4.8) using the Ohm's law definition of current density (Equation 4.4) (58). This yielded the following expression:

$$\vec{j} \times \vec{B} = \sigma \vec{\nabla} \varphi \times \vec{B} - \sigma \vec{V} \vec{B}^2 + \sigma \vec{B} (\vec{U} \cdot \vec{B}) \tag{4.30}$$

If we rename the Lorentz force as S, the Lorentz force can be made implicit using a Taylor expansion of the form:

$$S_{u_i}^{n+1} = S_{u_i}^{n} + \frac{\partial S_{u_i}}{\partial u_i} (u_i^{n+1} - u_i^{n}) \tag{4.31}$$

$\vec{C}_{fmag}$ is equal to $\frac{\partial S_{u_i}}{\partial u_i}$ and can be defined using the second term on the right hand of Equation 4.30 to produce:

$$\vec{C}_{fmag} = -\sigma \vec{B}^2 \tag{4.32}$$

The second source of error in the electric potential solver arises from the use of Ohm's law to calculate current density in the Navier Stokes equation. When there is a significant magnetic field, the difference between two large values is calculated on the right hand side of Ohm's Law (see Equation 4.33). This causes numerical errors when the equations are discretised (118).

$$\vec{j} = \sigma(-\nabla \varphi + \vec{U} \times \vec{B}) \tag{4.33}$$

Incorporating the gradient of the divergence of the magnetic vector potential, $\vec{A}$, as a source term removes this numerical error (119). This led to a modified definition of Ohms law- Equation 4.34 which was incorporated into ANSYS by solving an additional Poisson equation for the gradient of the divergence of the magnetic vector potential, $\vec{A}$.

$$\vec{j} = \sigma(-\nabla \varphi + \vec{U} \times \vec{B}) + \frac{\nabla(\nabla \cdot \vec{A})}{\mu_0} \tag{4.34}$$

The value for the divergence of $\vec{A}$ was set to zero at the fluid boundaries because total

Table 4.3: Benchmarking Results for Duct Flow Through Non Conductive Wall with Correction Factor

Hartmann Number	$\tilde{Q}_{analytical}$	$\tilde{Q}_{numerical}$	**Percent Difference**
76	0.00060785	0.00060440	0.570

current is zero at the fluid boundaries.

The third modification involved imposing a dirichlet condition to prevent nonphysical rises in the value of the electric potential. This is required because the value for electric potential was not set anywhere on the domain, which causes instabilities in the solver. A value of 1000 $A^2s^3kg^{-1}m^{-5}$ was used in this work.

Finally, the expert parameter multigrid solver "mg solver" option 2 was selected to produce more stable convergence. The aforementioned mesh study was performed after these four modifications were input into the solver.

The difference in model accuracy from implementation of these four corrections is evident from comparison of the benchmarking results before the modifications (Table 4.2) and after the modifications (Table 4.3). A contour velocity plot is shown in Figure 4.8. The velocity contour shows a central, high velocity region surrounded by boundary layers on all walls, similar to what occurs in hydrodynamic flows but with slower velocity values due to MHD drag. The analytical and numerical results show less than 1% difference suggesting the adjustments to the numerical model were successful.

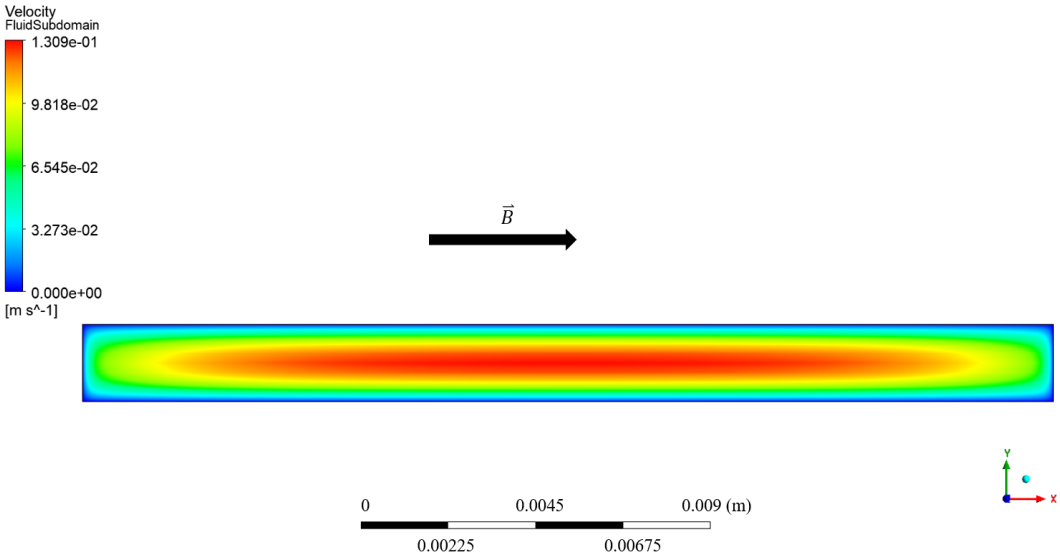


Figure 4.8: Velocity contour plot for flow with insulating walls in the presence of transverse (x direction) magnetic field, where flow is in the z direction

4.2.1.2 2D Duct Flow with Conductive Hartmann Walls and Transverse Magnetic Field

The next benchmarking case involved 2D duct flow with conductive Hartmann walls. The set-up was similar to the case of nonconducting walls, with the addition of 3 mm solid walls. Equation 4.25 was also used for this case.

In the presence of conducting walls, current lines flowed through the conductive walls rather than through the boundary layer. The presence of a conductive wall provided a low resistance return path which induced larger current and resulted in more MHD drag.

Figure 4.9 shows a velocity contour plot in the duct, and the analytical and numerical comparison is shown in Table 4.4. Similar to the case of insulated walls, these results show a velocity contour similar to what is expected in hydrodynamic flow due to the low magnetic field values investigated. Also, the numerical and analytical results show strong agreement which validates the use of ANSYS to model MHD duct flows.

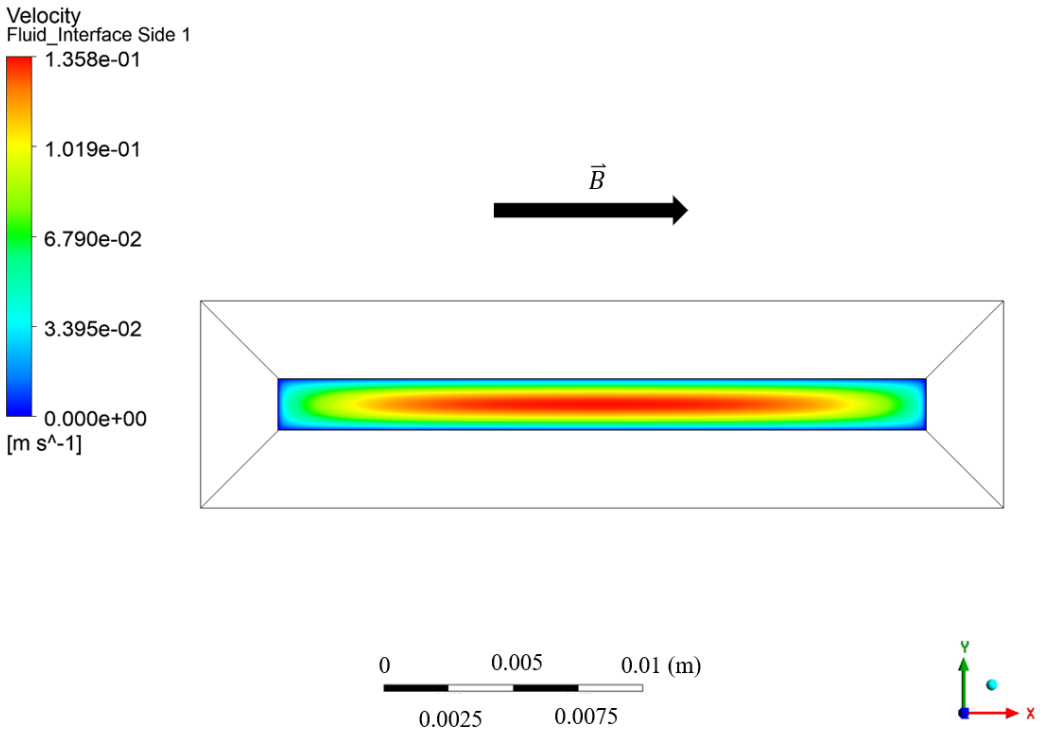


Figure 4.9: Velocity contour for the case of conducting Hartmann walls in the presence of transverse (x direction) magnetic field, where flow is in the z direction.

Table 4.4: Benchmarking Results for Duct Flow Through Conductive Hartmann Walls.

Hartmann Number	$\tilde{Q}_{analytical}$	$\tilde{Q}_{numerical}$	**Percent Difference**
76	0.00054955	0.00054624	0.61

4.2.1.3 2D Free Surface Flow with Transverse Magnetic Field

A simplified model of 2D duct flow was constructed by adding a free slip condition on the top, sidewall of the model derived in the previous section. The free slip boundary conditions means the derivative of the velocity component perpendicular to the wall must be zero, as shown in Equation 4.35.

$$\frac{\partial \vec{U}_z}{\partial \vec{n}} - 0 \tag{4.35}$$

Replacing the top duct wall with a free surface caused the electrical current moving through the fluid to return through the free surface boundary layer rather than the duct wall or sidewall boundary layer. This current return path experienced less drag than would be experienced at a duct wall interface. Hence, the flow rate was slighter faster for free surface flow compared to duct flows.

The analytical solution for free surface flow with a transverse magnetic field was derived by Shishko (43) as Equation 4.36. Note that the Shishko definition of dimensionless flow rate, $\tilde{Q}$, is different from the Hunt and Shercliff definition. For consistency, the original Shishko definition of $\tilde{Q}$ was multiplied by 16 to account for this difference (the Shercliff/Hunt definition of $\tilde{Q}$ can be found in Equation 4.20). The results of the 2D free surface flow numerical model compared to the Shishko solution are in Table 4.5, which shows a smaller numerical flow rate and greater percent difference from the analytical solution compared with the 2D duct flow cases. From Equation 4.36, $\tilde{Q}$ equals infinity when the Hartmann number is 0. This means this analytical solution is less accurate at lower Hartmann numbers, which explains the large differences between the analytical and numerical solutions. Another possible source for the large percent difference for this solution was the thin wall approximation imposed in the Shishko solution. This approximation assumed a constant electric potential in the walls, so the electric potential equations only needed to be solved for

Table 4.5: Benchmarking Results for Free Surface Flow Through Conductive Hartmann and Side Walls in the Presence of Transverse Magnetic Field

Hartmann Number	$\tilde{Q}_{analytical}$	$\tilde{Q}_{numerical}$	**Percent Difference**
76	0.00184	0.00144	21.9

the fluid (120). Though this approximation was not valid for the geometry explored in this thesis, the Shishko analytical solution provided a good estimation for MHD free surface fluid behaviour. Due to the large percent difference noted for this test case, an additional simulation was run on a square domain with sidewalls 100x smaller than the channel width. This alternate geometry aligned with the assumptions made by Shishko and produced a percent difference of less than 2%, suggesting much of the error on the simulation run on OLME geometry is due to the low aspect ratio. Figure 4.10 shows a velocity contour plot for this case, and Figures 4.11 and 4.12 show the induced current and MHD force vectors in the presence of this transverse magnetic field. The direction of the current vectors was as predicted in Figure 4.1, and the MHD force vectors show lower MHD drag present in the portions of the channel where the velocity remained high, as expected.

$$\tilde{Q}_w = \frac{4(1+\chi_1)}{Ha(1+\chi_1 Ha)}\left[\frac{h}{w} - \frac{1}{18}\left(\frac{1}{\sqrt{Ha}} + \frac{\chi_2}{1+\chi_2\sqrt{Ha}}\right) + \frac{4}{9}\frac{\chi_1\sqrt{Ha}}{1+\chi_1}\left(1 - \frac{1}{3}\frac{\chi_2\sqrt{Ha}}{1+\chi_2\sqrt{Ha}}\right)\right] \tag{4.36}$$

$$\chi_1 = \frac{2t\sigma_{solid}}{w\sigma_{fluid}} \tag{4.37}$$

$$\chi_2 = \frac{2(w+2t)\sigma_{solid}}{w\sigma_{fluid}} \tag{4.38}$$

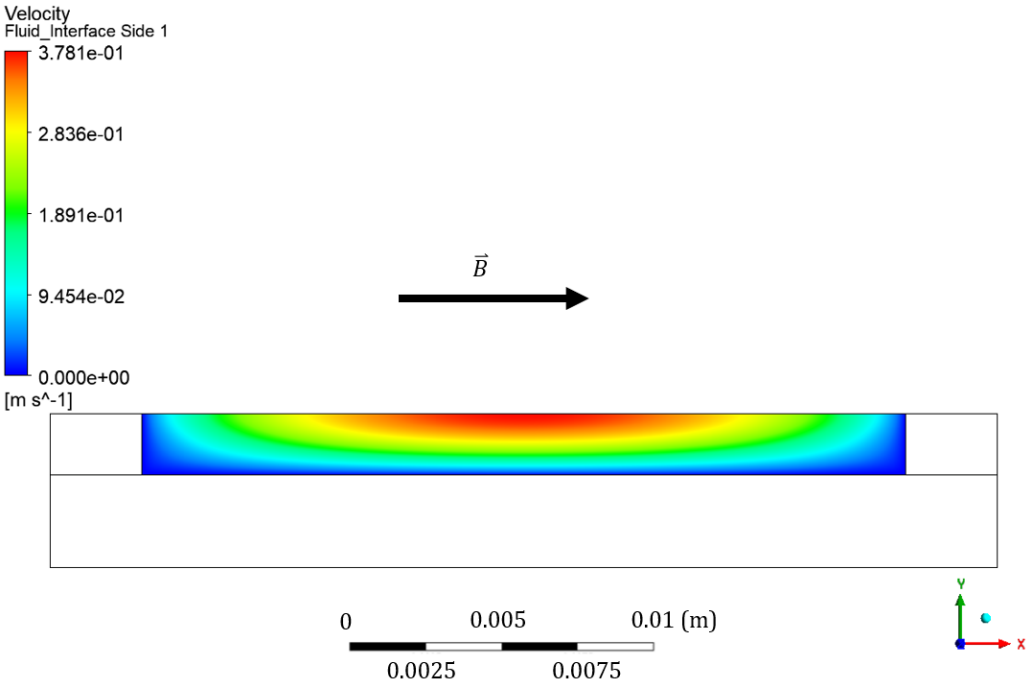


Figure 4.10: Velocity contour for the case of free surface flow in the presence of transverse (x direction) magnetic field, with flow in the z direction.

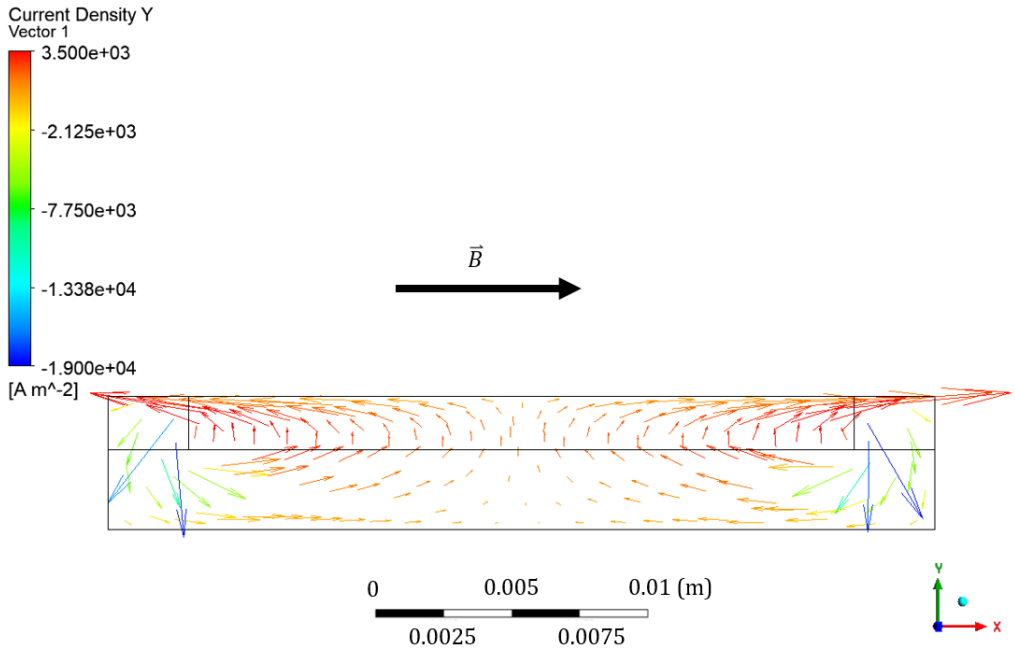


Figure 4.11: Current density vectors showing the direction and magnitude of the induced current. The colour map represents the component of the current density that is perpendicular to the magnetic field.

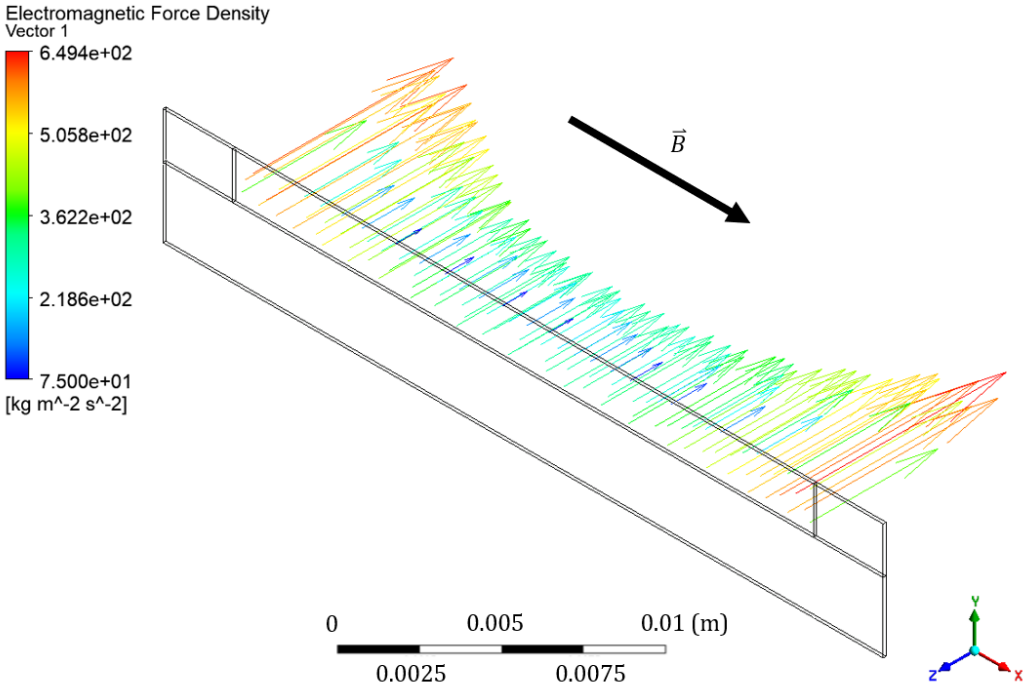


Figure 4.12: Force vectors showing the generated MHD drag force. The colour map represents the magnitude of the MHD drag force.

4.2.1.4 2D Free Surface Flow with Surface Normal Magnetic Field

An analytical estimation of free surface flow in the presence of a surface normal magnetic field and conductive walls was derived by Miyazaki in 1986 (42). At the free surface, the electric current gradient is zero, which also occurs along the centreline perpendicular to the magnetic field direction for duct flow. Accordingly, the dimensionless flow rate representative of free surface flow was estimated by solving for $\tilde{Q}$ on a domain where the duct height was double the expected free surface height. Then $\tilde{Q}$ for the condition of the free surface was taken as half of $\tilde{Q}$ for the condition of duct flow.

Miyazaki defined average velocity as Equation 4.39. Average velocity was converted to dimensionless flow rate using Equation 4.20.

$$U = \frac{dP}{dz}\frac{1}{k_p \sigma_f B^2} \tag{4.39}$$

$$k_p = \frac{c_w}{1 + \frac{h}{3a} + c_w} \tag{4.40}$$

The Hartmann number tested for this field orientation was one-tenth of that used in the

Table 4.6: Benchmarking Results for Free Surface Flow Through Conductive Hartmann and Side Walls in the Presence of vertical magnetic field

Hartmann Number	$\tilde{Q}_{analytical}$	$\tilde{Q}_{numerical}$	**Percent Difference**
12.16	5.76e-5	5.24e-5	9.06

transverse orientation because the characteristic length changed from being half of the fluid width (0.02 m) to half of the fluid height (0.002 m) while all other parameters of the Hartmann number were kept constant. Comparison of the numerical and analytical dimensionless flow rate values for surface normal magnetic field are shown in Table 4.6. Similar to the Shishko solution, the Miyazaki solution is also mainly valid for large Hartmann numbers, which is the likely cause of larger percent difference for this case. Figure 4.13 shows a velocity contour plot in the duct. High velocity jets were present adjacent to the shercliff layers, which were predicted by Hunt (41) and also witnessed in ANSYS CFX by Khodak (57). Figures 4.14 and 4.15 show the current and MHD force vectors, respectively. Comparing these plots with the respective plots for the transverse magnetic field illustrate why the surface normal field has the dominant impact on liquid metal flow. The MHD force generated by the surface normal field is greatest in the bulk flow region which is where most of the flow occurs. In the transverse field case, the strongest MHD force occurred in the boundary regions only, which limits the impact of MHD drag on overall fluid behaviour.

Looking at the direction of the current density vectors, for the surface normal case the high current density locations are primarily perpendicular to the magnetic field, so MHD drag effects are strong. On the other hand, the high current density locations on the transverse field plot are mainly parallel to the magnetic field, so MHD drag effects are minimal.

The velocity jets present in the surface normal case appear to be caused by lower current density near the side walls, so MHD drag effects are less in in that area which causes velocity spikes between the areas of higher current density and the no slip sidewalls.

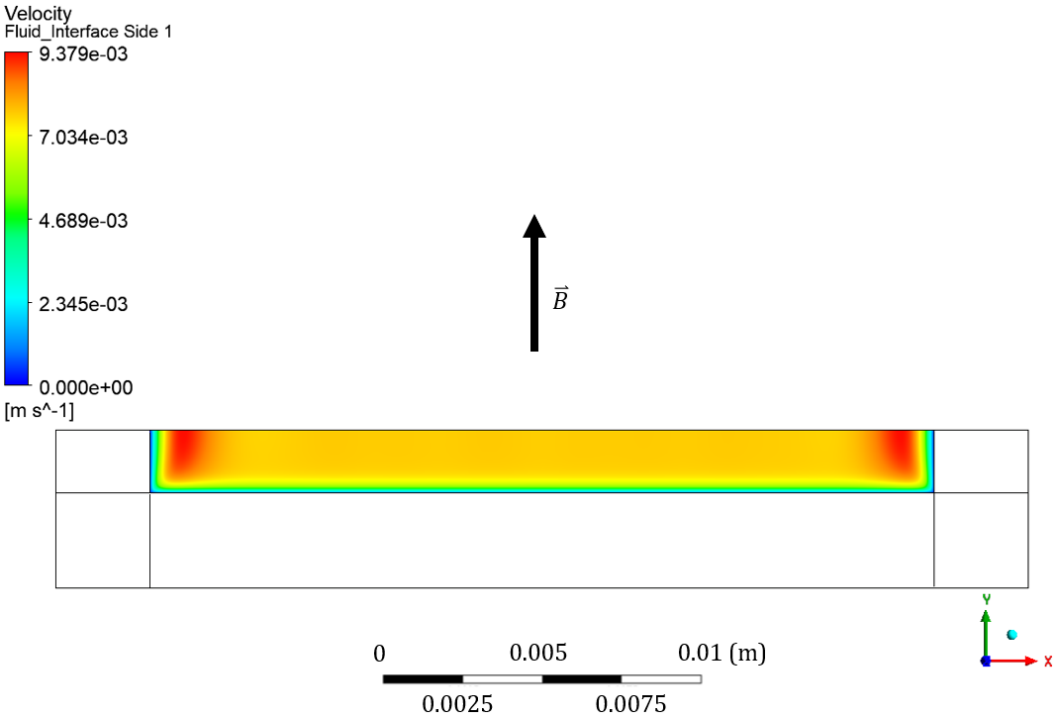


Figure 4.13: Velocity contour for the case of free surface flow in the presence of a surface normal (y direction) magnetic field, with flow in the z direction.

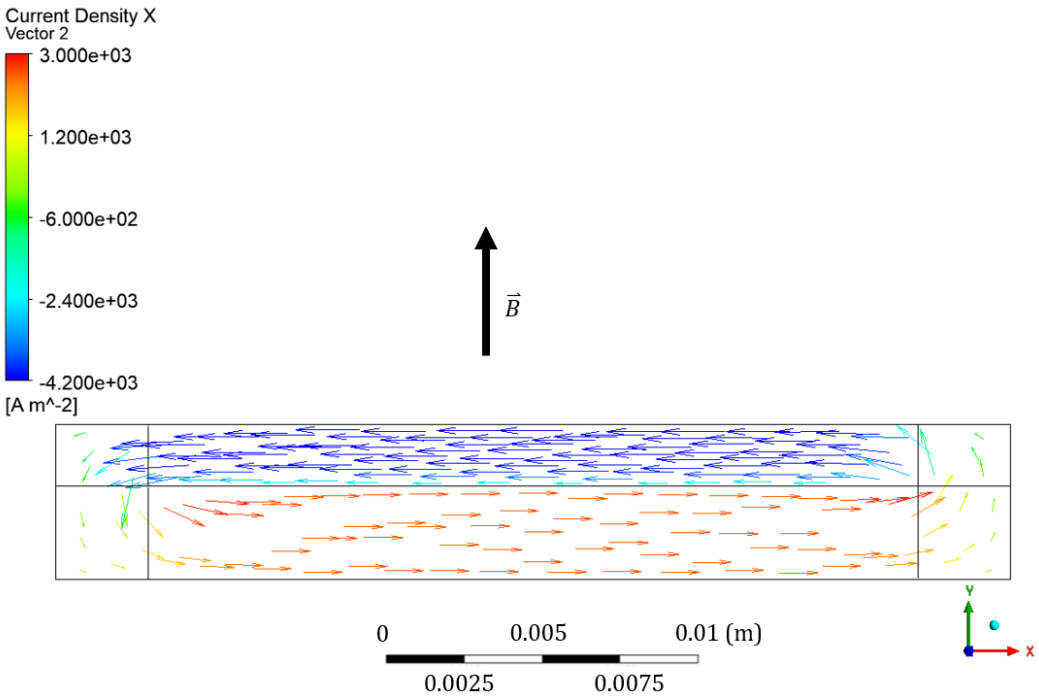


Figure 4.14: Current density vectors showing the direction and magnitude of the induced current. The colour map represents the component of the current density that is perpendicular to the magnetic field.

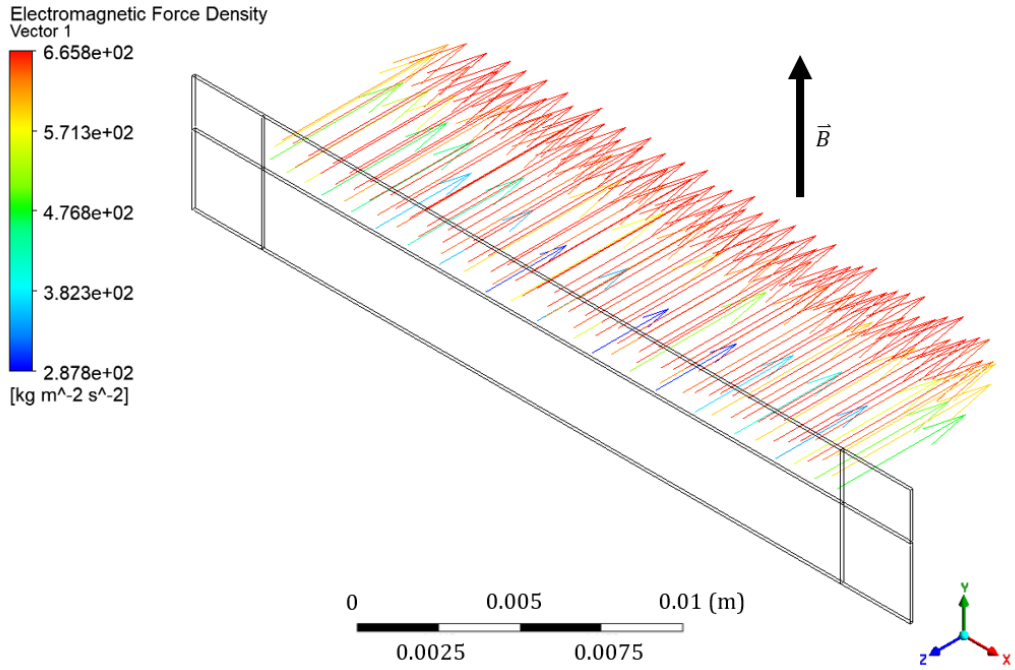


Figure 4.15: Force vectors showing the generated MHD drag force. The colour map represents the magnitude of the MHD drag force.

4.3 Benchmarking for Developing Flow MHD

Practically, fully developed flow is rarely realised in practice because changes in geometry, channel angle, surface roughness and other external factors lead to variations in the velocity and height of fluid flow in a channel. In the case of flow on an incline, fully developed flow can occur for long channel lengths were the entrance length is exceeded (121). A horizontal channel was used on the OLME, so the developing flow formulation was most appropriate for comparison to analytical and numerical results. In a fusion setting, the developing flow scheme is also most relevant due to constantly varying reactor conditions (magnetic field, current, temperature, etc.) that will impact fluid mechanics.

The following section builds off the validation of ANSYS CFX for modelling fully developed flow to assess the ability of this software to handle developing flow mechanics. The solver viability was determined by comparing the streamwise velocity profile down the channel length for both the numerical and analytical solutions.

4.3.1 Analytical Derivation of Developing Flow in a Flat Channel

A formulation for developing flow across a flat channel was recently derived by Sun *et. al.* in 2023 (45). The derivation is shown here and then altered to incorporate a 0.16 T surface normal field. A control volume of fluid with changing height y was considered, as shown in Figure 4.16.

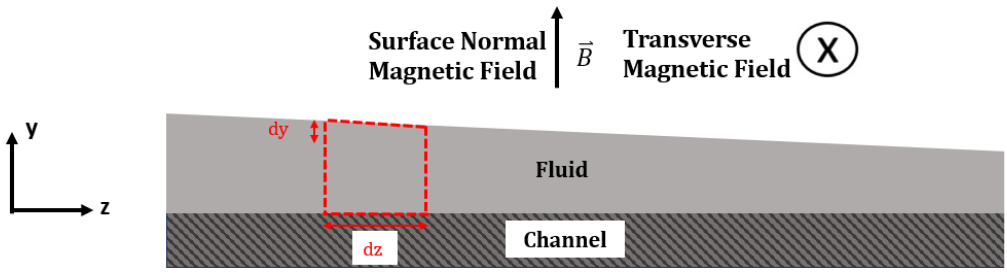


Figure 4.16: 2D schematic of developing flow down a channel, showing the control volume outlined in red.

Conservation of mass was represented by Equation 4.41, which became Equation 4.42 to describe this set up, where $A = wy$. In this thesis, y represents the fluid height. Cancelling like terms yielded Equation 4.43 which related the fluid height, y, to fluid velocity, U.

$$(\rho AU)_{in} - (\rho AU)_{out} = 0 \tag{4.41}$$

$$\rho w\left(y+\frac{dy}{2}\right)\left(U+\frac{dU}{2}\right) - \rho w\left(y-\frac{dy}{2}\right)\left(U-\frac{dU}{2}\right) = 0 \tag{4.42}$$

$$\frac{dy}{y} = -\frac{dU}{U} \tag{4.43}$$

Equation 4.44 was used to describe conservation of momentum. Here, $U = \frac{Q}{wy}$ and $F_f = \tau(w+2y)dz$. This equation simplified to Equation 4.46 for this set up, where τ is shear stress.

$$Q\rho(U_{out} - U_{in}) = P_{in} - P_{out} - F_f + F_{mag} \tag{4.44}$$

$$P_{in} - P_{out} = \iint_A \rho g y \, dy \, dw = \frac{1}{2}\rho g w y_{in}^2 - \frac{1}{2}\rho g w y_{out}^2 \tag{4.45}$$

$$\rho w(y+\frac{dy}{2})\left((U+\frac{dU}{2})^2 + g\frac{y+\frac{dy}{2}}{2}\right) - \rho w(y-\frac{dy}{2})\left((U-\frac{dU}{2})^2 + g\frac{y-\frac{dy}{2}}{2}\right) = -\tau(w+2y)dz + (j\times B)_z wy dz \tag{4.46}$$

For fully developed open channel flow, the left hand side of Equation 4.44 would equal zero, so the sum of the friction and MHD drag forces would equal zero. An empirical correlation for the pressure drop can be inserted into the momentum equation as shown in Equation 4.47, where λ is the friction coefficient. This simple correlation was used to simplify the developing flow derivation, and future work should investigate methods to model this momentum conservation more accurately for developing flow.

$$\frac{\lambda}{8}\rho U^2(w+2y) = -\tau(w+2y) + (j\times B)_z wy \tag{4.47}$$

The left hand sides of Equations 4.47 and 4.46 were set equal to each other to form Equation 4.48.

$$\rho w(y+\frac{dy}{2})\left((U+\frac{dU}{2})^2 + g\frac{y+\frac{dy}{2}}{2}\right) - \rho w(y-\frac{dy}{2})\left((U-\frac{dU}{2})^2 + g\frac{y-\frac{dy}{2}}{2})\right) = -\frac{\lambda}{8}\rho U^2(w+2y)dz \tag{4.48}$$

The left hand side of Equation 4.48 was simplified by expanding and cancelling like terms to yield Equation 4.49.

$$2\rho wyU\,dU + \rho wU^2 dy + \rho w\left(\frac{dU}{2}\right)^2 dy + \rho wgydy = -\frac{\lambda}{8}\rho U^2(w+2y)dz \tag{4.49}$$

Equation 4.43 was used to eliminate dU from Equation 4.49 to yield Equation 4.50, which simplifies to Equation 4.51.

$$-\rho wU^2 dy + \frac{\rho wU^2(dy)^3}{y^2} + \rho wgydy = -\frac{\lambda}{8}\rho U^2(w+2y)dz \tag{4.50}$$

$$wy\rho U^2 dy\left(\frac{-1}{y} + \frac{dy^2}{y^3} + \frac{g}{U^2}\right) = -\frac{\lambda}{8}\rho U^2(w+2y)dz \tag{4.51}$$

Higher order derivative terms were then removed to form Equation 4.52.

$$wy\rho U^2 dy\left(\frac{-1}{y}+\frac{g}{U^2}\right)=\frac{-\lambda}{8}\rho U^2(w+2y)dz \tag{4.52}$$

This was rearranged to Equation 4.53, where the right side of the equation was equivalent to the streamwise pressure gradient, $\frac{dP}{dz}$.

$$\rho U^2 dy\left(\frac{-1}{y}+\frac{g}{U^2}\right)=\frac{-\lambda}{8wy}\rho U^2(w+2y)dz=\frac{dP}{dz} \tag{4.53}$$

The volumetric flow rate, Q, was substituted for average velocity U, using Equation 4.54 to form Equation 4.55. MHD effects were then incorporated through existing fully developed analytical solutions for MHD pressure gradient.

$$U=\frac{Q}{wy} \tag{4.54}$$

$$\left(\frac{gw^2y^2}{Q^2}-\frac{1}{y}\right)dy=-\frac{w^2y^2}{\rho Q^2}\frac{dP}{dz}dz \tag{4.55}$$

A formulation for pressure drop in the presence of transverse magnetic field was determined by rearranging Shishko's formulation (Equation 4.36) to solve for pressure gradient using Equation 4.20. The resulting pressure drop formulation was substituted into Equation 4.55. After integration, the final Equation 4.56 was produced.

$$z=z_{out}-\frac{\rho wQ}{\mu D_1}\left(\left(\frac{gw^2(y^2-y_{out}^2)}{2Q^2}+\frac{1}{y}-\frac{1}{y_{out}}\right)+D_2\left(gw^3\frac{y-y_{out}}{Q^2}+\frac{w}{2y^2}-\frac{w}{2y_{out}^2}\right)\right) \tag{4.56}$$

Here, y_{out} was representing assuming a waterfall outlet condition, where fluid flows freely over the outlet edge, represented by Equation 4.57 (122), and D_1 and D_2 are constants represented by Equations 4.58 and 4.59 .

$$y_{out}=\left(\frac{Q^2}{gw^2}\right)^{1/3} \tag{4.57}$$

$$D_1 = 4Ha\frac{1+CHa}{1+C} \tag{4.58}$$

$$D_2 = -\frac{1}{18}\left(\frac{1}{\sqrt{Ha}}+\frac{C_w}{1+C_w\sqrt{Ha}}\right)+\frac{4}{9}+\frac{C_w\sqrt{Ha}}{1+C_w}\left(1-\frac{1}{3}\frac{C_w\sqrt{Ha}}{1+C_w\sqrt{Ha}}\right) \tag{4.59}$$

The formulation for developing flow in a surface normal magnetic field was determined by inserting Miyazaki's formulation for pressure gradient (from Equation 4.39) into Equation 4.55 to produce Equation 4.60.

$$z = z_{out} - D_3\left(D_4(\frac{y^3-y_{out}^3}{3}+\frac{y^4-y_{out}^4}{6w}+D_5\frac{y^2-y_{out}^2}{2})-ln(y/y_{out})-\frac{2(y-y_{out})}{3w}+\frac{D_5}{y}-\frac{D_5}{y_{out}}\right) \tag{4.60}$$

$$D_3 = \frac{\rho Q}{w\sigma_w t_w B^2} \tag{4.61}$$

$$D_4 = \frac{gw^2}{Q^2} \tag{4.62}$$

$$D_5 = \frac{\sigma_w t_w}{\sigma_f} \tag{4.63}$$

Sun also provides the solution for flow across a flat channel in the absence of magnetic field, shown in Equation 4.64. This equation was used in this thesis to determine height changes caused by MHD effects.

$$z = z_{out} - \frac{\rho Q}{6\mu}\left(\frac{1}{w+2y}-\frac{gw^2}{8Q^2}\left(\frac{w^3}{w+2y}+3w^2\ln(w+2y)-3w(w+2y)+\frac{(w+2y)^2}{2}\right)-\right.$$
$$\left.\frac{1}{w+2y_{out}}-\frac{gw^2}{8Q^2}\left(\frac{w^3}{w+2y_{out}}+3w^2\ln(w+2y_{out})-3w(w+2y_{out})+\frac{(w+2y_{out})^2}{2}\right)\right) \tag{4.64}$$

The experiments described in the next chapter involve surface normal field only, so the rest of this chapter describes progress in developing a relevant 3D, numerical model of developing flow in surface normal conditions using ANSYS CFX.

4.3.1.1 Numerical Modelling of Developing 3D Free Surface Flow on a Flat channel

A 3D model of free surface, developing flow was developed in ANSYS CFX using the channel geometry presented in Chapter 3. The ANSYS CFX free surface flow modelling guide provided general modelling guidance (113). ANSYS utilises a volume of fluid surface tracking method where the volume fraction of two immiscible fluids is determined across the domain using one conservation of momentum equation to jointly describe both fluids. The free surface was assumed to be where the volume fraction equaled 0.5. This numerical model was run at magnetic field values of 0.075 T, 0.113 T, and 0.16 T, and flow rates of 0.0318 kg/s, 0.0424 kg/s, and 0.053 kg/s. These values correspond to parameters tested on the OLME. The boundary conditions described for the 2D simulations earlier in this chapter were maintained. The electric potential was 0 at all boundaries. At the inlet, a mass flow rate was imposed, and the outlet was modelled as an opening at atmospheric pressure, to represent the waterfall assumption. The free surface was also modelled as an opening with an initial gauge pressure of 0 Pa.

True free surface simulations often struggle to converge due to spurious surface waves, so a transient model was created and run until the the free surface height plateaued. Firstly, the model was run without magnetic field until the free surface height converged. Convergence was assumed when the average height along the channel length varied by less than 0.00001 m between iterations. This solution was then used as the initial condition for consequent simulations run with magnetic field.

Various meshes were studied to determine the optimal for these 3D simulations. Five meshes were investigated, as shown in Figure 4.17 where fluid height along the channel centreline is plotted for all five meshes. The initial mesh used all tetrahedral elements. Four additional meshes were then created using hexahedral elements in the fluid domain and tetrahedral elements in the solid domain. The hexahedral meshes included inflation boundaries that allowed additional refinement near the boundary layers. Comparing results from the coarsest hexahedral mesh with 291,255 elements to the tetrahedral mesh with 572,549 results showed that fewer elements were required for a hexahedral mesh with inflation layers than a tetrahedral mesh to achieve the desired results. This was mainly due

to the incorporation of inflation layers that allowed for fine resolution in the boundary layers and more course resolution outside of these regions. The optimal mesh chosen had 3,769,787 elements, as doubling the number of elements led to less than a 1% difference in fluid height. This optimal mesh used 100 divisions along the fluid height and 68 elements along the fluid width, with a bias factor of 10 oriented to allow for smaller elements on the boundary layers.

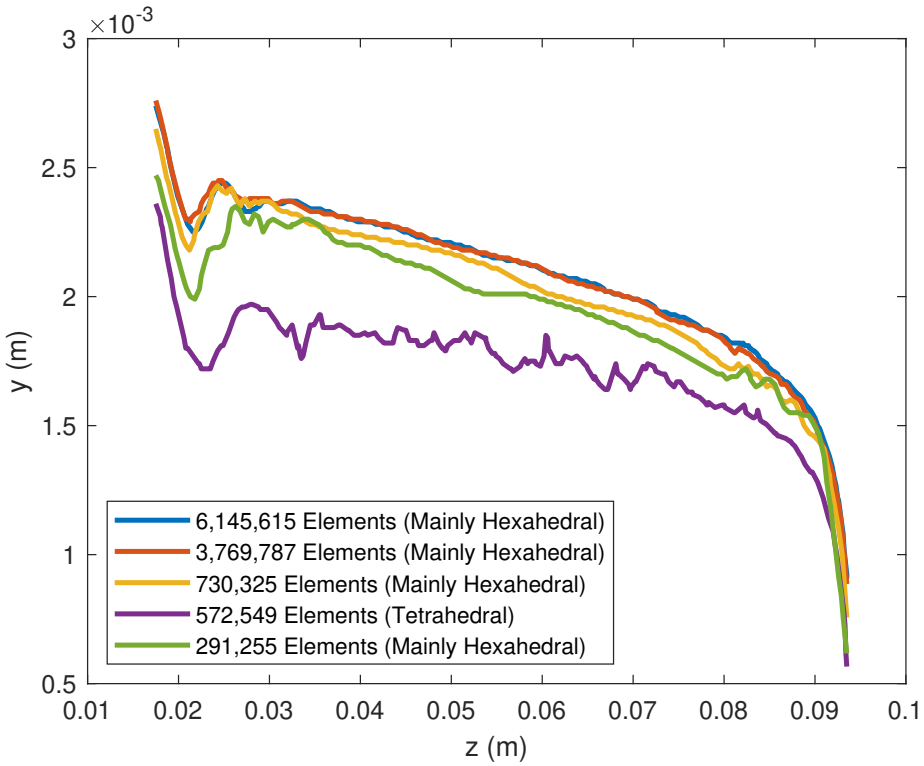


Figure 4.17: Mesh sensitivity analysis performed for a 3D simulation of liquid metal flow in ANSYS CFX. Liquid metal free surface height along the centreline of the channel was compared for various meshes. One mesh was made with all tetrahedral elements, and the other four were made using hexahedral elements on the fluid domain and tetrahedral elements on the solid domain, as well as inflation layers near the boundary region.

To explore the phenomena revealed by the numerical simulations, several figures are presented for the representative case of B = 0.16 T and a flow rate of 0.053 kg/s. The current density streamlines are plotted in Figure 4.18 to confirm that the surface normal magnetic field was generating an induced current that travelled through the fluid channel walls as predicted from Figure 4.1. The transverse velocity contour halfway along the channel is shown in Figure 4.19, showing velocity jets on the walls parallel to the surface normal magnetic field and a constant velocity profile in the centre. These velocity jets were

predicted analytically by Hunt (41) and are caused by the distribution of the induced current (123). These jets cause instabilities in the fluid, which likely accounts for the waves on the velocity contour free surface. The constant central velocity was confirmed by Figure 4.20, which shows a top view of the liquid metal free surface, where a relatively constant velocity profile occurred in the centre of the channel.

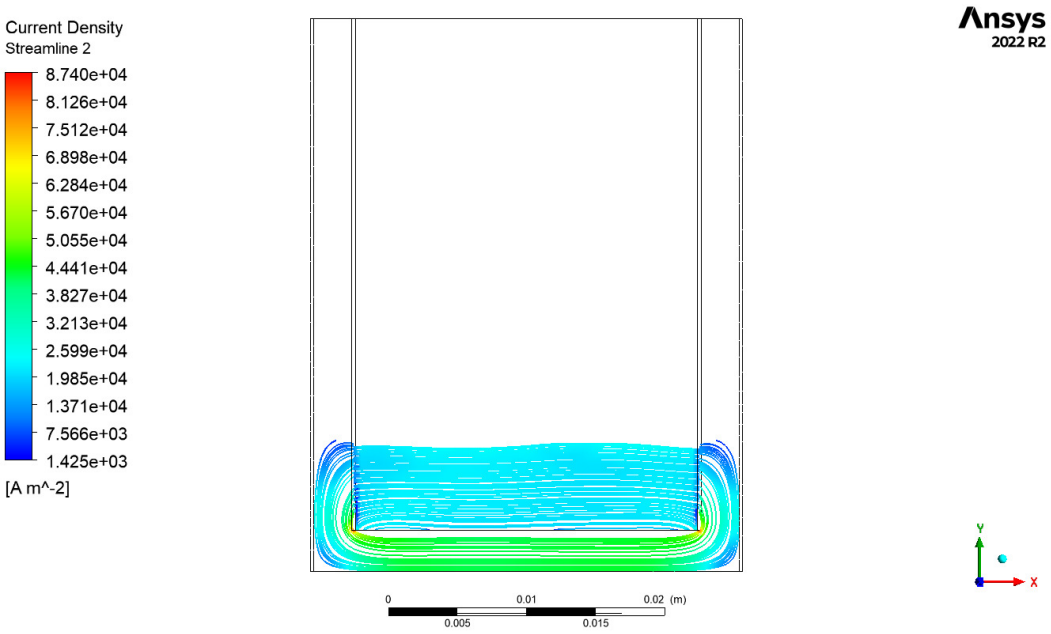


Figure 4.18: Current density streamlines for the case of B = 0.16 T and a flow rate of 0.053 kg/s showing a recirculating induced current.

Figure 4.21 provides a streamwise velocity contour along the channel centreline, showing a gradually decreasing liquid metal height along the channel length. The outlet shows very large fluid velocities that are not realistic, which suggests additional mesh refinement should be completed in this region in future simulations to better capture the dynamics in the outlet region.

The streamwise fluid height along the length of the channel is shown in Figures 4.22, 4.23, and 4.24, compared with analytical estimations. Firstly, the 0 T case, which was solved using Equation 4.64, appeared to be a flat line when compared with the magnetic field range tested on the OLME. However, upon comparison with smaller magnetic field values in Figure 4.25 it was clear that the curvature of 0 T hydrodynamic streamwise profile was similar to the profiles present for the magnetohydrodynamic cases. Also, for very low values of magnetic field the magnetohydrodynamic equation produced streamwise height

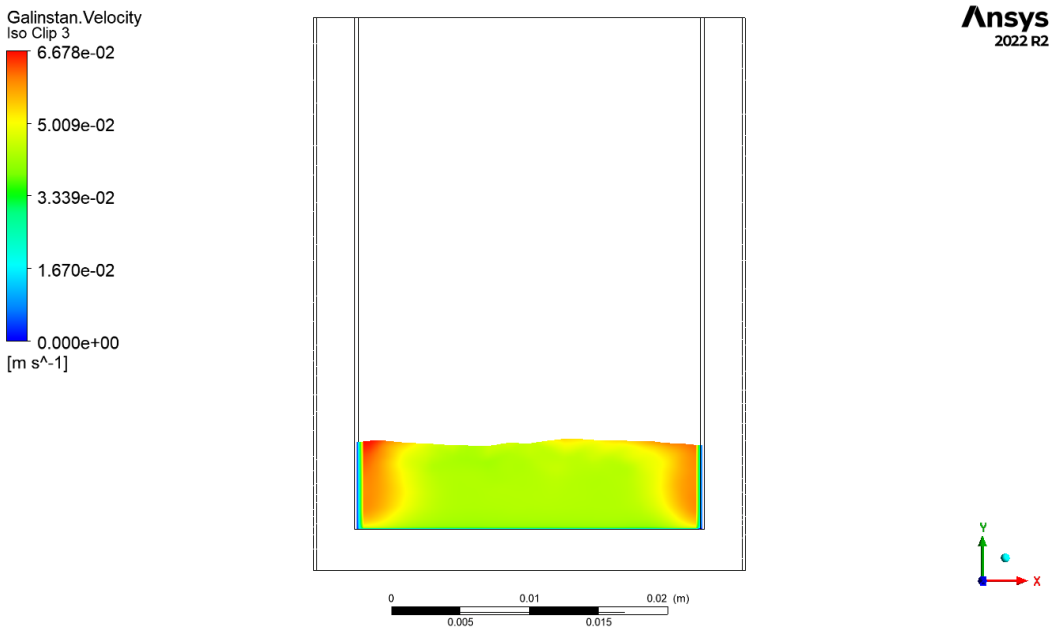


Figure 4.19: Transverse velocity profile for the case of B = 0.16 T and a 0.053 kg/s flow rate, showing high velocity jet formation along the walls parallel to the surface normal magnetic field.

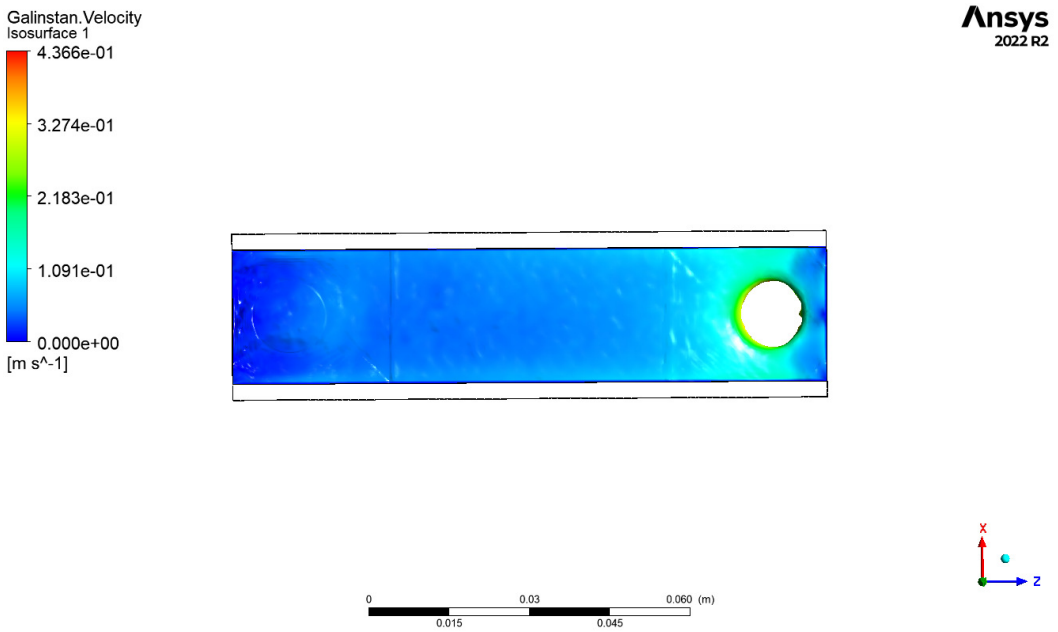


Figure 4.20: Velocity contour plot on the free surface, for the 3D ANSYS model of developing flow across a channel for a flow rate of 0.053 kg/s and magnetic field of 0.16 T. Flow is from left to right, along to z axis, and the magnetic field is surface normal (y direction).

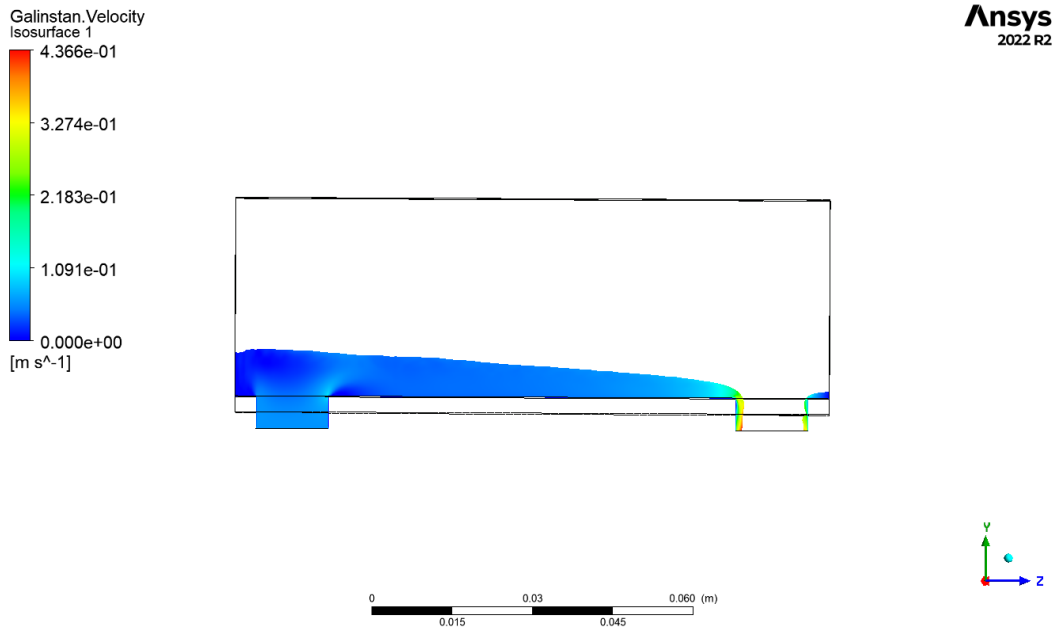


Figure 4.21: Streamwise velocity contour plot along the channel centreline for a flow rate of 0.053 kg/s and magnetic field of 0.16 T. Flow is from left to right, along to z axis, and the magnetic field is surface normal (y direction).

profiles lower than what was predicted hydrodynamically, which is unrealistic. This trend of magnetohydrodynamic equations losing accuracy approaching 0 T was discussed in (39, 41) and can be attributed to increased analytical complexity when the MHD behaviour does not dominate over the hydrodynamic behaviour. MHD equations typically have increased convergence at larger Hartmann number values where MHD behaviour dominates. So when dealing with low Hartmann number flows, higher height profile produced between the MHD and hydrodynamic equation should be assumed.

In general, the trend of decreasing liquid metal height along the channel was realised both numerically and analytically. Looking at the case of 0 T magnetic field, the numerical solution produced higher height values for a given flow rate than the analytical solution, which translated to smaller average numerical velocity values assuming conservation of mass. The differences suggest that there is some 3D behaviour of the liquid metal flow that was not fully captured in the 2D analytical model, such as MHD pileup near the inlet, edge effects, and inlet/outlet frictional losses. Also, in the derivation of the analytical solution, the Miyazaki solution for MHD pressure drop in fully developed flow was incorporated into the final developing flow equation to account for MHD effects. This caused an

overestimation of fluid velocity (and MHD height change) analytically because fully developed flows occur when the fluid velocity has reached its maximum. This explains why most of the analytical cases tested showed higher MHD height change values than their numerical counterparts. MHD effects are directly proportional to fluid velocity, so the difference in height between flow with magnetic field and flow without magnetic field was smaller for the numerical solutions. This can be visualised by comparing, for example, the average fluid height at B = 0 T to the average fluid height at B = 0.075 T. Plots of average height values along the channel are presented later in this chapter.

The rapid decrease in fluid height near the outlet was present in both models, and for a given magnetic field and flow rate, the slope of the resultant fluid height profile along the channel length was similar in the numerical and analytical cases. The numerical model was 3D and the analytical model was 2D, so the waterfall outlet condition utilised in the analytical model did not fully represent the geometry of 3D numerical model as a true waterfall did not occur at the outlet. The circular shape of the fluid outlet meant the fluid in reality did not drop off as a waterfall, but instead funneled into the outlet hole which contributed to reducing the numerical fluid velocities.

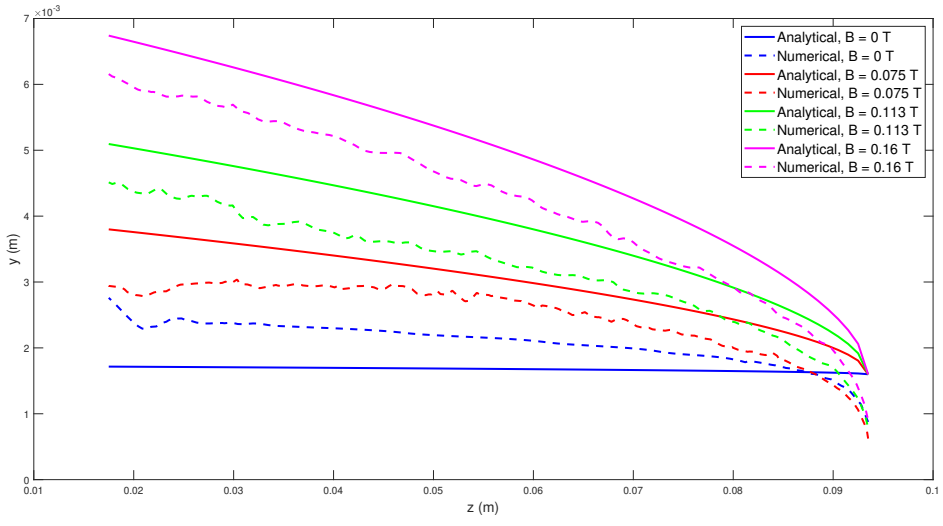


Figure 4.22: Fluid height along the channel length for a flow rate of 0.0318 kg/s at various values of magnetic field.

To compare the analytical and numerical solutions, measurements of the centreline free surface height before and after the addition of the magnetic field are compared between

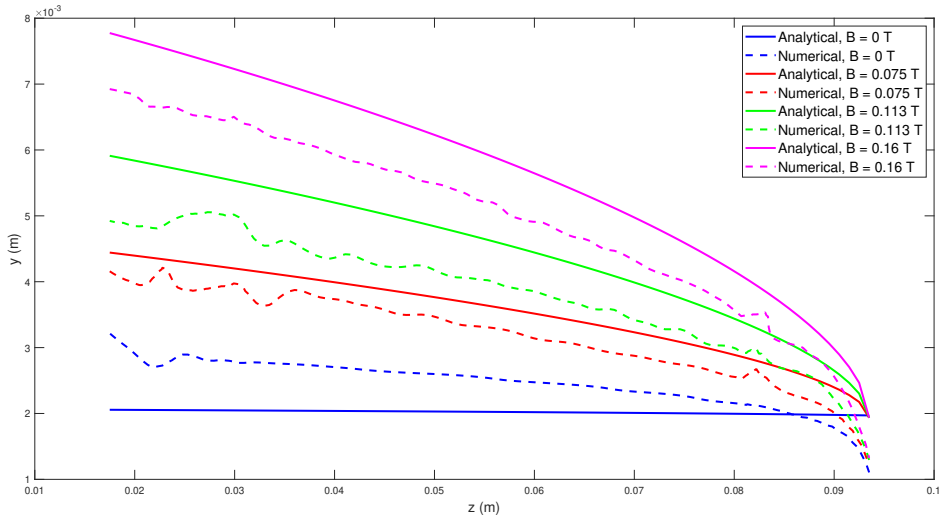


Figure 4.23: Fluid height along the channel length for a flow rate of 0.0424 kg/s at various values of magnetic field.

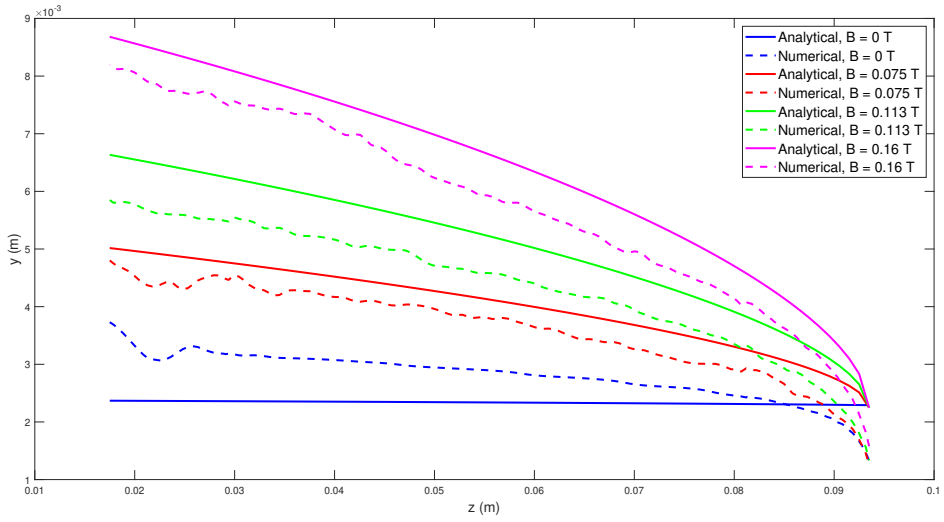


Figure 4.24: Fluid height along the channel length for a flow rate of 0.053 kg/s at various values of magnetic field.

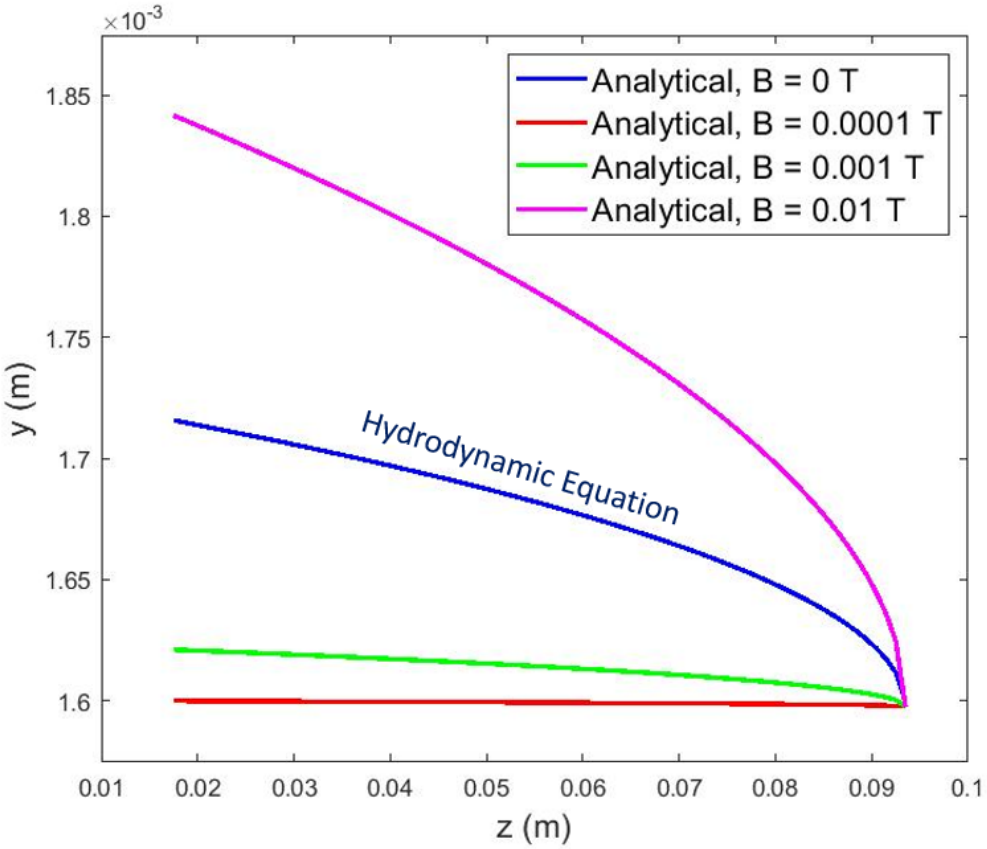


Figure 4.25: Fluid height along the channel length for a flow rate of 0.0318 kg/s at lower values of magnetic field. The B = 0 T case is plotted using the hydrodynamic equation and plotted in blue. The remaining cases are plotted using the surface normal solution derived in this chapter.

z=0.039 m and z=0.065 m measured from the inlet. Numerically, there was a less than 1% difference between the centreline fluid height and the average fluid height across the channel width, so the centreline fluid height was used here. This measurement line represents the location of the experimental data collected, which is further elaborated on in the Chapter 5. To summarise the range of numerical and analytical solutions gathered, the height change Δh, given by Equation 4.68, is plotted against Hartmann number in Figure 4.27 and Stuart number is Figure 4.28. The Stuart number, N, represents the ratio of electromagnetic to inertial forces (see Equation 4.67). The ratio of inertial to viscous forces was represented as the Reynolds Number (see Equation 4.65), Re, where hydraulic diameter, R_h, was the characteristic length represented by Equation 4.66. The height change for each case was determined using Equation 4.68, where h_0 was initial height and h_B was fluid height in the presence of magnetic field. The Reynolds and Hartmann numbers are both dependant on fluid height, so the numerical and analytical solutions have different values for these dimensionless parameters.

$$Re = \frac{QR_h}{\nu} \tag{4.65}$$

$$R_h = \frac{wh}{w+2h} \tag{4.66}$$

$$N = \frac{Ha^2}{Re} \tag{4.67}$$

$$\Delta h = h_B - h_0 \tag{4.68}$$

Figure 4.27 shows increasing height change with increasing Hartmann number for both the analytical and numerical solutions, as expected. Looking at the data for each flow rate individually shows similar slope values between the numerical and analytical results, which suggests both models agree on the effect of increasing Hartmann number on the resultant height change. As the Hartmann number approaches 0, the height change should also

approach 0 as MHD drag was the cause of the height changes studied in this thesis. Interestingly, the numerical height change more closes approaches 0 as the Hartmann number approaches 0, compared with the analytical results. This suggests that the numerical solution was more accurate in describing MHD behaviour. The analytical solution overpredicts the expected height change likely because the MHD effects were incorporated into this solution using the Miyazaki pressure drop formulation which assumes fully developed flow. In the case of fully developed flow, a larger velocity would be present (and larger MHD drag) than the developing flow case presented in the thesis, which explains the analytical overprediction of MHD height change.

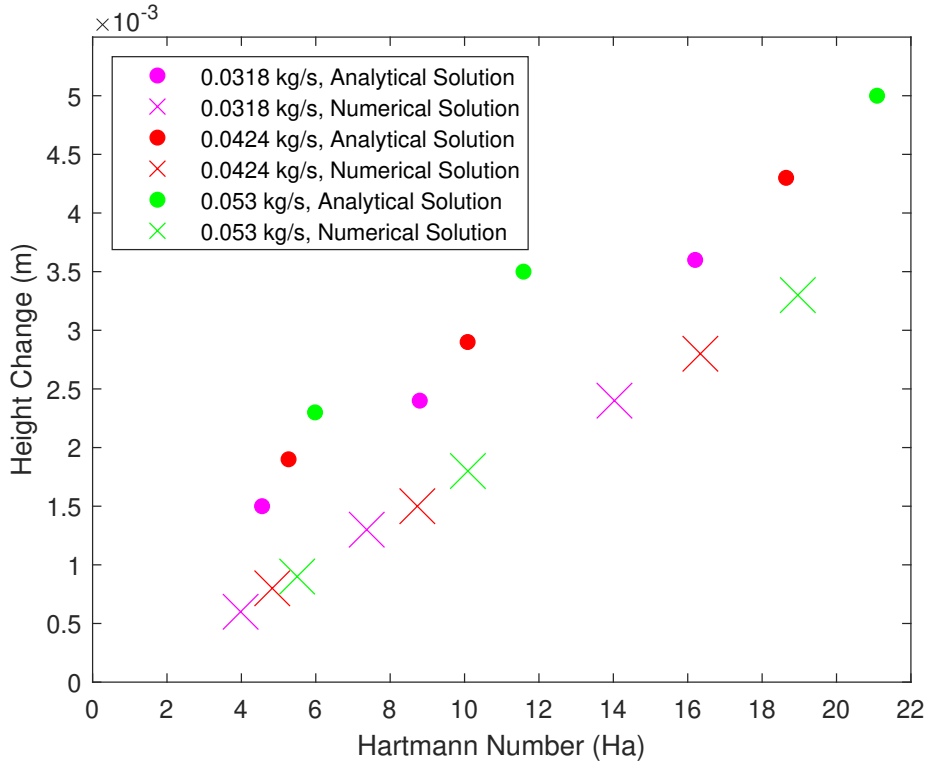


Figure 4.26: Fluid height change plotted against the Hartmann number for numerical and analytical solutions.

The height change is plotted against the Stuart number is Figure 4.28. Though the results are non linear, a general increase in height change with increase in N and Ha is shown from these figures, as expected. A quadratic relationship between Stuart number and Height change can be assumed from the results in this figure, though more data points would be required to define the correlation. This aligns with the quadractic relationship between

height change and Stuart number determined experimentally for liquid metal flows in a transverse field, presented by Yang (82).

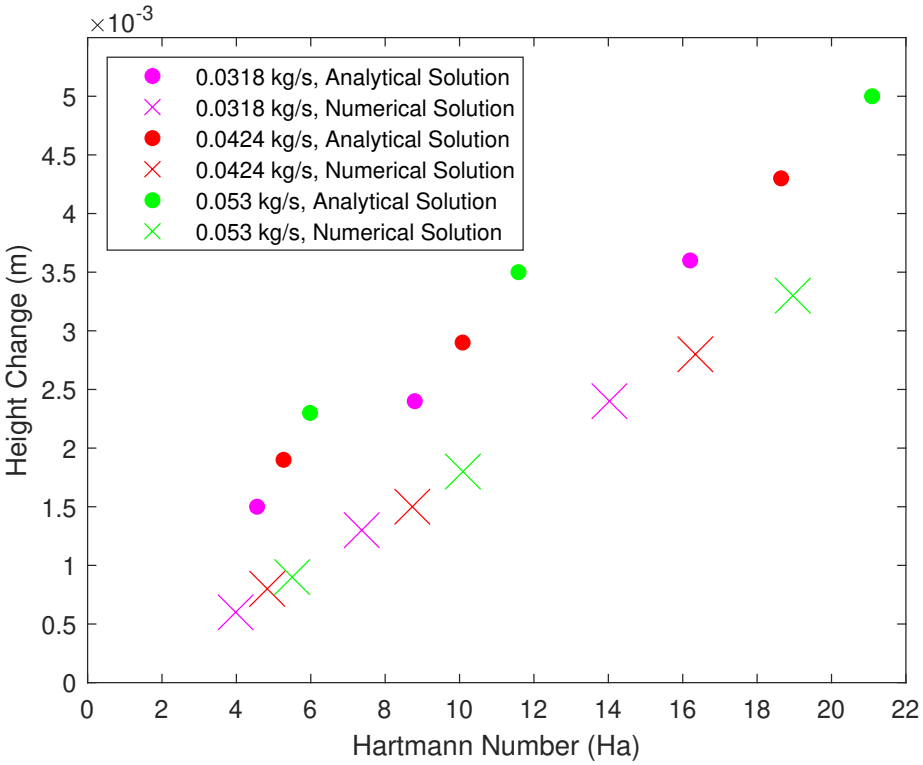


Figure 4.27: Fluid height change plotted against the Hartmann number for numerical and analytical solutions.

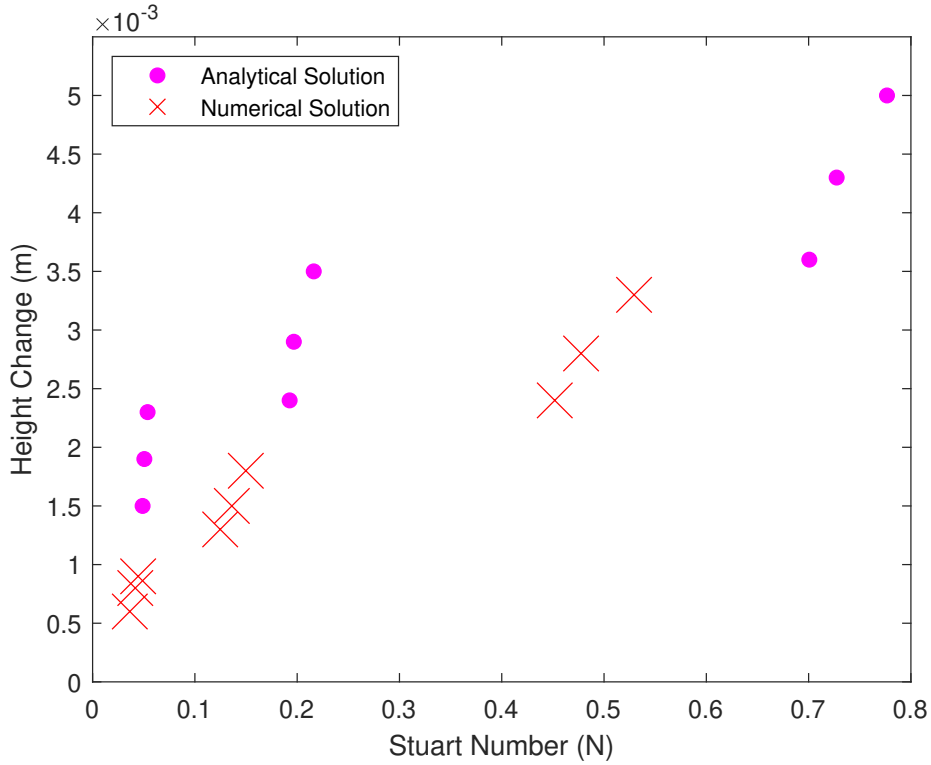


Figure 4.28: Fluid height change plotted against the Stuart Number for numerical and analytical solutions.

4.4 Method for Experimental Validation

Ultimately, this numerical model was developed to simulate the phenomena occurring on the Oxford Liquid Metal Experiment (OLME). This modelling work will be particularly useful for extrapolating results to higher Hartmann numbers, such as those experienced in magnetic confinement fusion, where designing an experiment to capture relevant data would be difficult and expensive. Visual access to plasma facing components is restricted in magnetic confinement fusion experiments, and, more generally, in scenarios with large magnetic fields that can impact the operation of data capture equipment. Hence, it is vital to have numerical models available, that are validated with experimental data, to develop estimations of liquid metal flow parameters at fusion relevant conditions.

The remaining chapters of this thesis detail the development of the OLME to quantify the behaviour of liquid metal flows under the influence of magnetic fields. Ultimately, the experimental data captured was compared with analytical and numerical results to provide a novel validation of the ANSYS CFX MHD solver to experimental data for low aspect ratio

flows.

There is a wealth of exciting numerical work remaining to produce increasingly relevant models for future PFC design iterations. The systematic incorporation of thermal effects would significantly enhance the usefulness of this model as the effects of TEMHD and incident high heat flux plasma strikes could be accounted for. More readily, the expansion of this work to incorporate flow on an incline would be invaluable.

4.5 Summary

The key takeaways from this chapter are the following:

1. A numerical model of fully developed 2D Duct flow at a low aspect ratio flow was created in ANSYS and validated against analytical solutions for insulating walls, conductive Hartmann walls, and all conductive walls with pseudo free surface in the presence of a transverse and surface normal magnetic fields. This validated the use of the commercial software ANSYS CFX to model MHD flow.

2. An analytical solution for developing flow across a flat plat with surface normal magnetic fields was derived.

3. A 3D numerical model of free surface, developing flow across a flat channel was created and compared to the analytical solution showing a qualitative agreement in expected trends.

Chapter 5

Experimental Measure of Surface Normal Field Effects

This chapter details experimental data collected on the OLME measuring free surface height changes in response to a surface normal magnetic field, and compares these results to the analytical and numerical results presented in Chapter 3. The chapter ends with a discussion of challenges faced when experimentally studying liquid metal flows. Various alternative channel designs are explored and contact angle measurements are produced on a variety of surface roughnesses.

5.1 Data Collection Methodology

In this work, the experimental data collection focused on measuring the impact of a surface normal magnetic field on free surface liquid metal height for a flat channel. An overview of the experimental data collection procedure is as follows:

1. Turn on the argon cover gas and allow the storage tank and channel to reach a slight overpressure (1-2 psi).

2. Flow liquid metal from the storage tank to the channel using the gear pump.

3. Turn on the laser triangulation system and measure the liquid metal height over 10 seconds, while the magnetic field is off.

4. For the next 10-20 seconds, keep the laser triangulation system on and turn on the magnetic field. The liquid metal height should increase due to MHD drag.

5. For the final 10 seconds, turn off the magnetic field while continuing to measure the liquid metal height.

Figure 3.12 shows the location of the laser line where height measurements were taken. Each trial produced a set of laser profiles that were ultimately arranged into a 3D array listing fluid height, position along the laser line, and time using a custom Excel macro and a MATLAB code.

A laser profile was taken of the channel surface before the introduction of liquid metal to serve as a calibration point to base liquid metal height measurements from. This measurement was subtracted from the liquid metal height readings to provide a calibrated liquid metal height value. Average values of the fluid height along the laser line were saved for every timestamp and plotted to generate a visual map of average fluid height over time in response to the magnet shutting on and off (see Figure 5.1). Initially, data was collected for both the transverse and surface normal magnetic field orientations. The comparative results shown in Figure 5.1 show a 0.46 mm difference in height change between the two orientations. As expected, the height changes in the transverse magnetic field orientation were indiscernible. A surface normal magnetic field has a greater effect on liquid metal flow than a transverse field, as stated in the literature review, and this was clearly shown in the data collected. Hence, the remainder of data collection focused on the measurement of surface normal field effects on a flat plate. A slight plate angle was enforced for these initial trials to increase measurable MHD effects, but it was later determined that flow on an incline often detached from the sidewalls to form jets down the plate. This made estimated MHD effects difficult as depth changes were linked to how well the liquid metal wet the entire channel. To avoid this, the remainder of the experimental data presented in this thesis were performed on a flat plate.

In addition to plots of average height over time, 3D plots were also generated showing the height along the laser measurement line at each timestamp. A sample of this plot is shown in Figure 5.2.

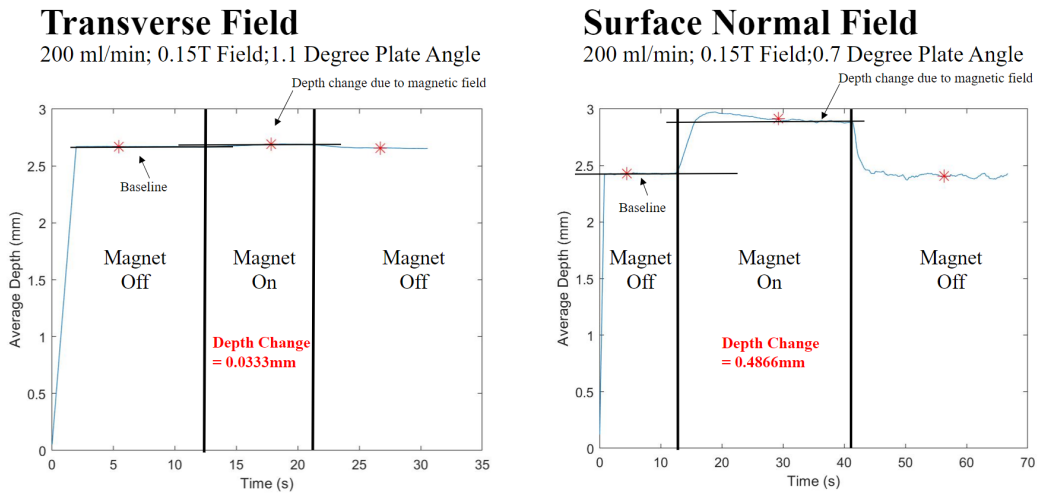


Figure 5.1: Comparison plot of average liquid metal height before and after introduction of a magnetic field, for transverse vs. surface normal magnetic field, showing a significantly larger height change in the surface normal magnetic field.

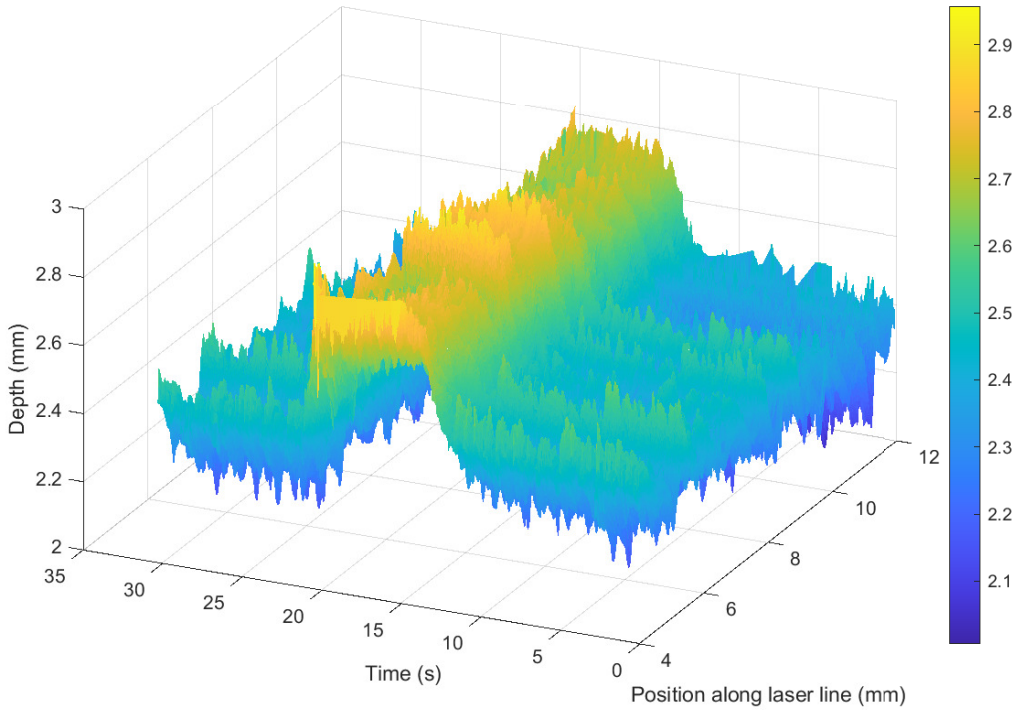


Figure 5.2: 3D Plot of liquid metal height profiles collected over time, in the presence of a surface normal magnetic field. The magnetic field was turned on at 12 seconds and turned off at 20 seconds.

5.2 Summary of Experimental Findings

The experimental data collected was compared to the analytical and numerical models of developing flow described in Chapter 4. A total of 27 experiments were performed. Three magnetic field values (0.075 T, 0.113 T, and 0.16 T) and three mass flow rates (0.0318 kg/s, 0.0424 kg/s, and 0.053 kg/s) were studied, and each combination was repeated three times. The fluid height values were determined along the channel centreline between 0.039 m and 0.065 m from the channel inlet, corresponding to the location of the laser triangulation system line. These models were first run without magnetic field for each of the three flow rates tested on the OLME to determine an initial average height value, h_0. Then these models were run with magnetic field to determine the average height due to MHD drag, h_B. The the difference between these two height changes was represented as, Δh.

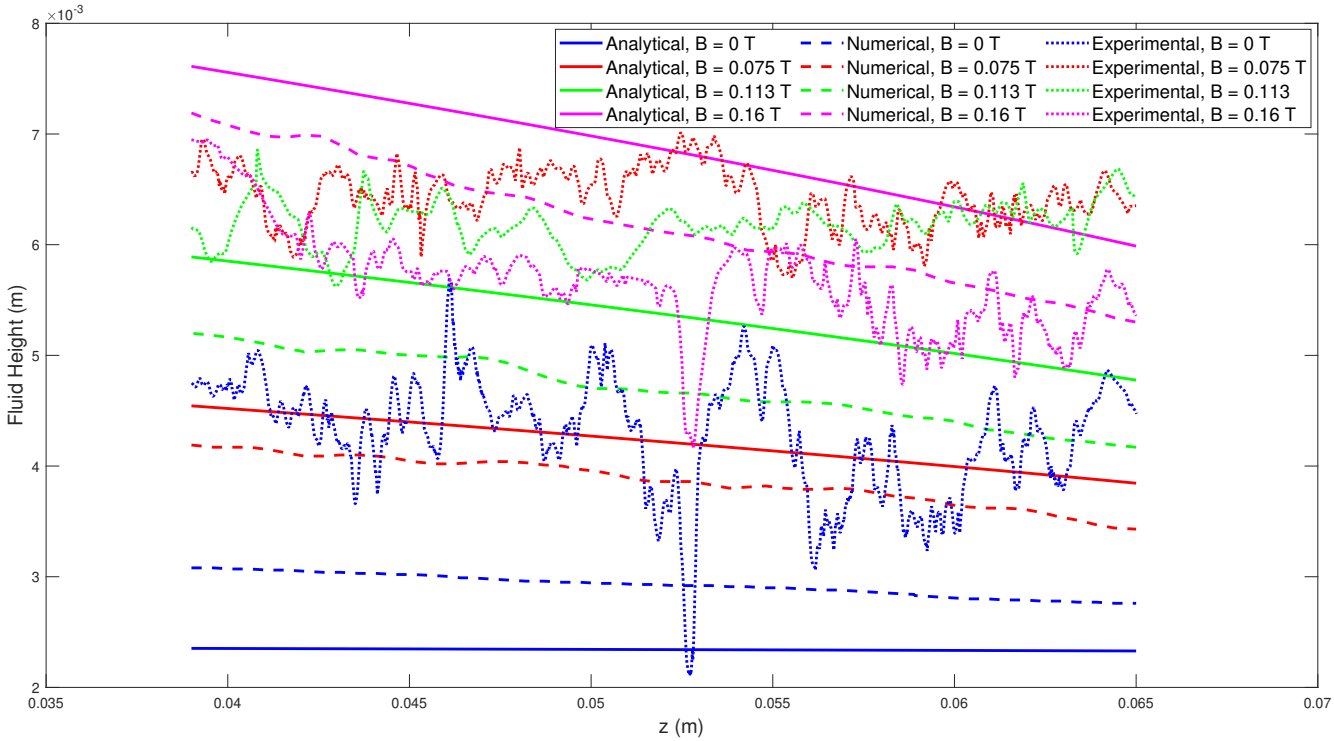


Figure 5.3: Streamwise fluid height across the channel for the analytical, numerical, and experimental cases. This data was collected at an inlet flow rate of 0.053 kg/s and at various magnetic field values between 0 T and 0.16 T.

Figure 5.3 shows a sample of the experimental data collected compared with analytical and numerical predictions for the 0.053 kg/s case. The experimental liquid metal height was

significantly higher than both the numerical and analytical results, which suggested a slower experimental flow velocity and less MHD drag. This was evident from the proximity of the B = 0 T experimental height line to the B = 0.16 T experimental height line, compared to the same lines in the numerical and analytical cases. The experimental data was presented showing the average height value over around 100 timesteps in an effort to smooth the signal. However, significant scatter in the data remained, suggesting that the laser system captured spurious reflections on the liquid metal surface. Although the streamwise height profile cannot be adequately discerned due to signal noise, the average height value measured along the laser line can be used to compare experimental trends with numerical and analytical predictions.

Looking at Figure 5.3, the experimental height does not appear to increase monotonically with increasing magnetic field as expected from the numerical and analytical data. This was due to the variable initial height values observed, the causes of which are further elaborated on at the end of this chapter. For the experimental data plotted in this figure, the initial height for the B = 0.075 T case was 0.0015 m larger than the initial height for the B = 0.16 T case, which contributed to the B = 0.075 T case showing a larger fluid height when the magnetic field was switched on. However, the height change witnessed for the B = 0.075 T case was smaller than the B = 0.16 T case, as predicted analytically. This is visible in Figure 5.4, where the change in height for each experimental trial is shown and an increase in height change with increasing magnetic field is clearly visible. To reduce the impact of the initial height reading on the experimental data analysis, several plots showing the average height change Δh are presented here to better discern the trends within the experimental results.

Figure 5.5 shows the analytical, numerical, and experimental values for height change, Δh, at various values for each of the Hartmann numbers and flow rates tested. This figure shows some agreement between the experimental, analytical, and numerical results for the trend of increasing height change in response to increasing surface normal magnetic field, particularly at higher Hartmann numbers. The initial height produced by each method is shown in Table 5.1, where an average value is shown for the experimental trials. The experimental initial height values were roughly double the numerical and analytical predictions,

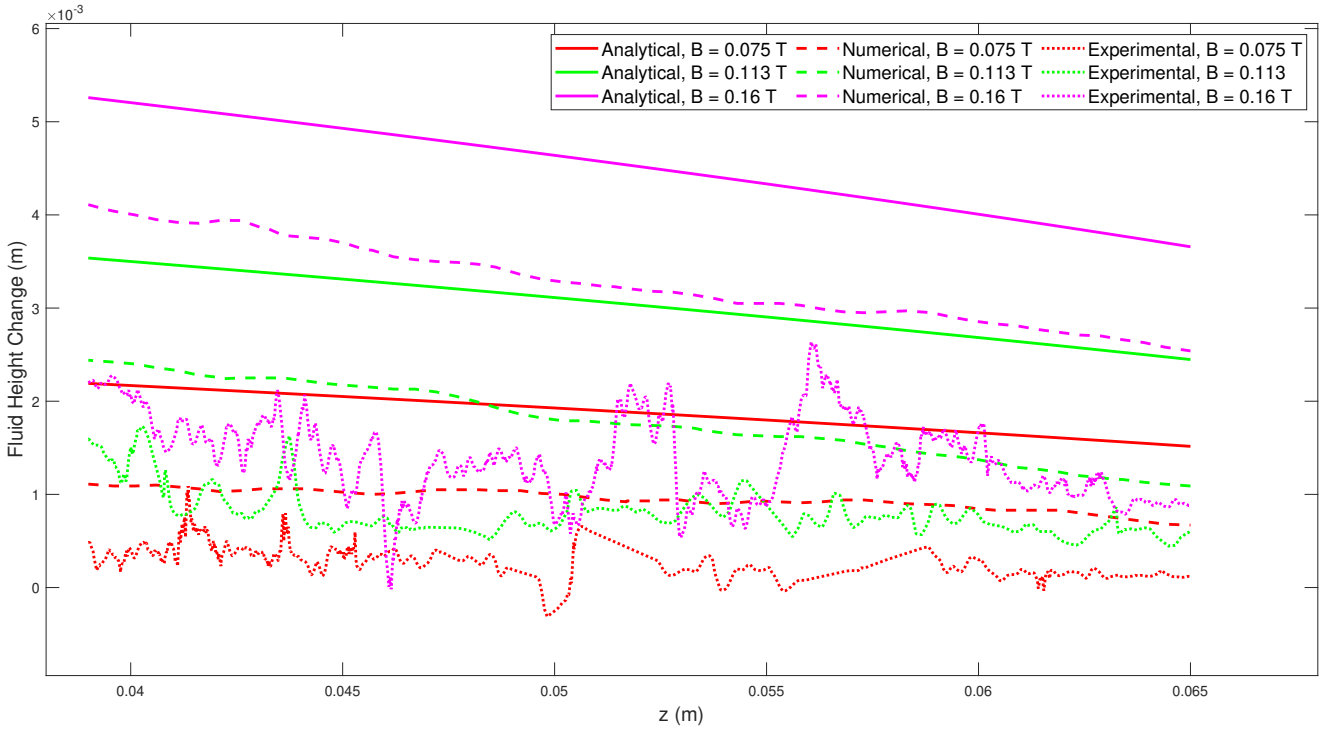


Figure 5.4: Streamwise fluid height change across the channel for the analytical, numerical, and experimental cases. This data was collected at an inlet flow rate of 0.053 kg/s.

Table 5.1: Comparison of analytical, numerical, and experimental initial height values for developing, free surface flow with surface normal magnetic field

Flow Rate (kg/s)	$h_{0,analytical}$ **(m)**	$h_{0,numerical}$ **(m)**	$h_{0,experimental}$ **(m)**
0.0318	0.0017	0.0023	0.0040
0.0424	0.0018	0.0026598	0.0048
0.053	0.0019	0.002913	0.0054

which translated to slower flowing films in the experimental case, and explains why the experimental height change values were lower than the numerical and analytical results. The MHD drag force is directly proportional to the fluid velocity, so a slower film will experience less MHD drag. It is also worth noting that the experimental magnetic field varied for the B = 0.16 T trials due to ohmic heating of the electromagnet coils which led to a reduced magnetic field if the magnet was not fully cooled.

A study performed by Yang (82) using a transverse field noted a critical Hartmann number above which the height change increases monotonically. According to Yang, the critical point was at Hartmann number 20 for a 1° channel in a transverse field. As explained in Chapter 2, the surface normal magnetic field should have the dominant effect on liquid metal

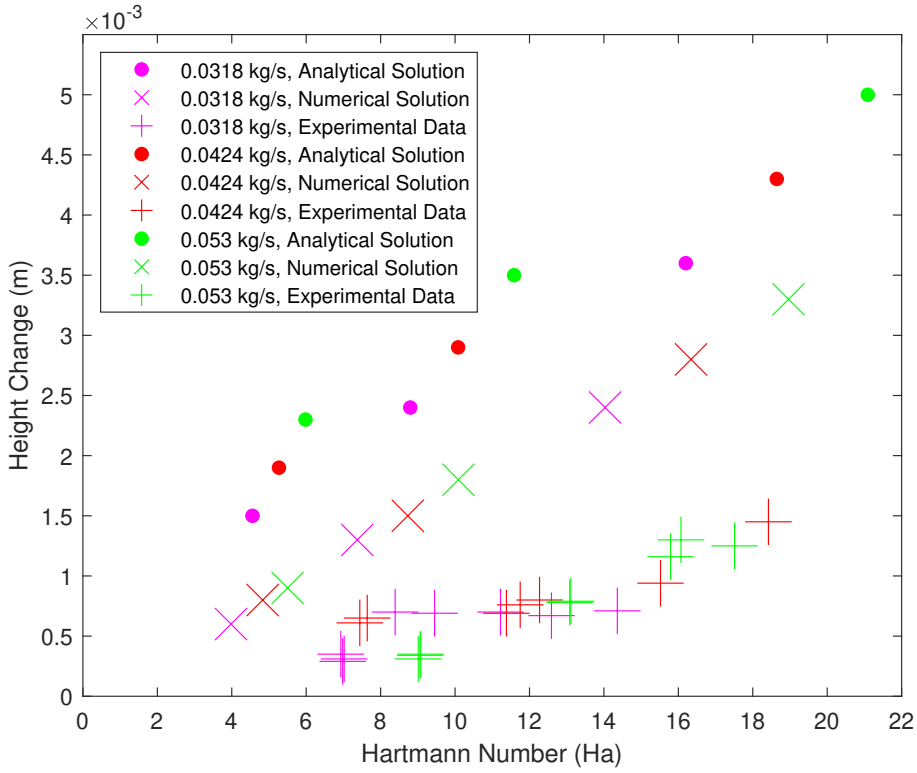


Figure 5.5: Comparison plot of analytical, numerical and experimental data height change values at various Hartmann Numbers collected at all three flow rate (0.0318 kg/s, 0.0424 kg/s, and 0.053 kg/s).

flow, so this critical Hartmann number should be lower for this present work as a surface normal field was used. From Figure 5.5, a monotonic height change increase was witnessed for Hartmann Number above 14 for this case of surface normal magnetic field and flow across a flat channel.

Figures 5.6, 5.7, and 5.8 show separate plots of height change compared with Hartmann number for the three flow rates studied. These plots indicate that Hartmann effects become monotonic experimentally above a flow rate of 0.0424 kg/s. Below this flow rate, the magnetic field had an indistinguishable effect on liquid metal height, which suggests MHD effects were dominated by hydrodynamic drag effects at these low velocities.

Finally, the Stuart number was plotted against height change in Figure 5.9. A slight, nonlinear increase in experimental height change occurred with increasing Stuart number. In the Yang (82) study conducted with a transverse magnetic field, a critical Stuart number of 0.1 was determined, above which height change appeared to increase quadratically and below

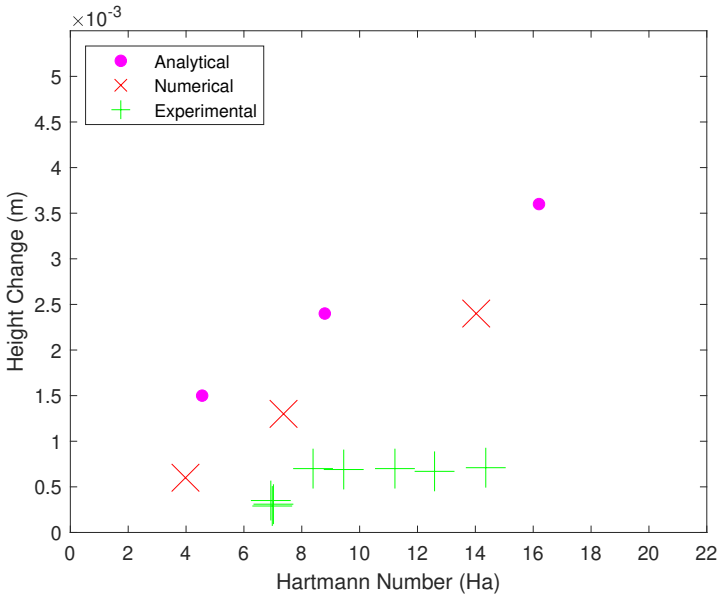


Figure 5.6: Comparison plot of analytical, numerical and experimental data height change values at various Hartmann Numbers collected for an inlet flow rate 0.0318 kg/s.

which there was little impact of increasing Stuart number on height change. From the data presented here, a slight increase is experimentally witnessed as Stuart Number increases, but additional data points would be required at higher Stuart numbers to determine this experimental critical Stuart number for the case of a surface normal magnetic field. The next section delves into various suggested improvements to the experimental set up to improve accuracy and remove variance between trials.

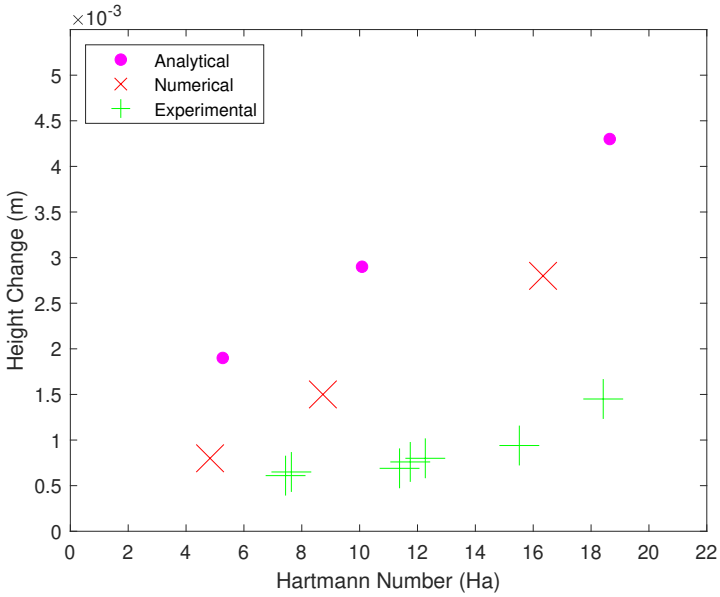


Figure 5.7: Comparison plot of analytical, numerical and experimental data height change values at various Hartmann Numbers collected for an inlet flow rate of 0.0424 kg/s.

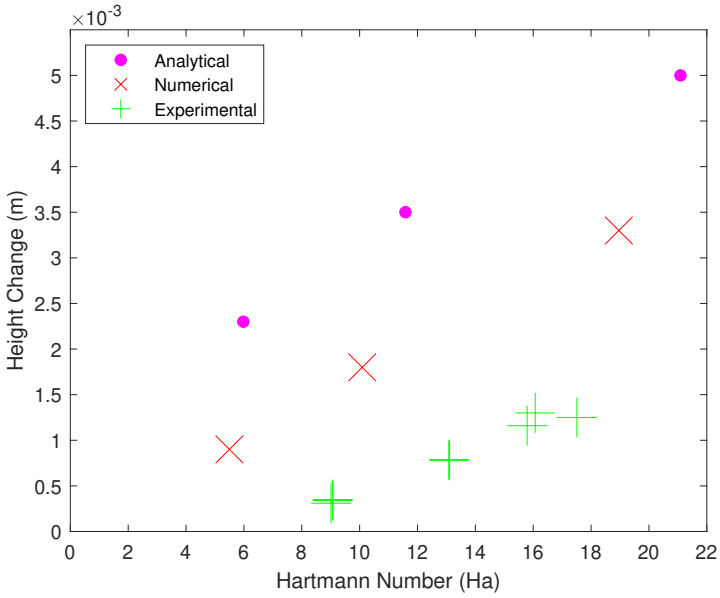


Figure 5.8: Comparison plot of analytical, numerical and experimental data height change values at various Hartmann Numbers collected for an inlet flow rate of 0.053 kg/s.

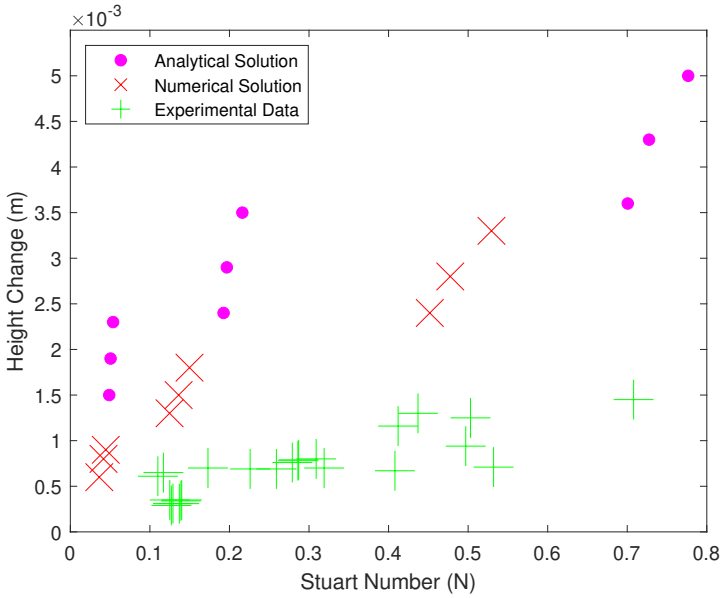


Figure 5.9: Comparison plot of analytical, numerical and experimental data height change values at various Hartmann Numbers collected for an inlet flow rate of 0.053 kg/s.

5.3 Areas for Improvement

The main challenge faced by the OLME was lack of reproducibility in the liquid metal flow parameters. Even without magnetic field, there were unexplained variations in fluid height between trials. The author has reasoned four possible sources of these errors and synthesised potential solutions to be assessed as future work.

1. Galinstan oxidation build up
2. Pressure gradients
3. Experimental scale
4. Nonuniform surface wetting due to high surface tension

Galinstan Oxidation build up

When Galinstan is exposed to air, it oxidises to form a gallium oxide layer on the free surface. This can be detrimental to a gear pump as the oxides can get trapped in the gears of the pump which leads to reduced pumping output. It is unsustainable to attempt to clean the pump after every trial, and the best long term solution is to replace the gear pump with an electromagnetic pump. However, no commercial electromagnetic pump was available at the small flow rate scale used for this experiment because these pumps are typically used at a much larger scale to transfer large amounts of water or other fluids. Development of an electromagnetic pump is beyond the scope of this project, but would serve as an invaluable addition to the experimental set up to nullify the effects of oxidation on the fluid loop operation.

In addition to gallium oxide affecting the pumping ability of the galinstan, this gallium oxide film is stagnant and possesses significantly lower electrical conductivity than galinstan (124). The presence of this stagnant oxidation layer build up can increase the liquid metal thickness and cause fluid velocity at the free surface to tend towards zero rather than reaching a maximum there. This oxidation layer also likely increases the surface tension, which can contribute to liquid metal detaching from the sidewalls which causes an increase in measured height. The presence of an oxide layer serves as an electrically insulated boundary at the

free surface and also reduces the electrical conductivity of the fluid over time, thus leading to lower height change readings as observed in this thesis (124, 125).

The induced MHD currents will not pass through this oxidation layer, but instead the currents will pass through the adjacent galinstan. In this case, the free surface velocity is reduced due to the presence of this stagnant oxidation layer, under the no slip boundary assumption, which reduces the magnitude of induced MHD current.

An attempt to measure the electrical conductivity of the galinstan was made using an ohmmeter. However, as the measurements were made in air, the ohmmeter must come in contact with the oxide layer (on the free surface) before reaching the bulk fluid. This caused the probe to immediately develop a gallium oxide coating that prevent accurate measurement of the bulk fluid electrical conductivity. Gallium oxide has a significantly lower electrical conductivity than galinstan, so artificially low measurements of electrical conductivity were made using this method.

Measurement of MHD current generation would be an excellent next step to troubleshoot the results of this experiment. The principles of MHD flow depend on the formation of induced electrical currents in the liquid metal channel. To the author's knowledge, no experiment has quantitatively measured these induced currents in free surface flow. Developing a method to measure these induced currents might provide an alternative route to monitoring liquid metal flow parameters, in addition to providing insight on the magnitude of MHD current generation in the system. Future work should include measurement of the electrical conductivity of the galinstan over time to better understand how oxidation effects impacts the fluid and electrical behaviour in the bulk fluid domain and at the free surface.

Pressure Gradients

Another potential cause of the variations in liquid metal height was caused by the use of flexible tubing. The height and positioning of the tubing can cause small variations in the pressure gradients in the system. As fluid flows through the system, the tubing sometimes shifts in response to fluid build up in different parts of the system or changes in fluid velocity. Utilising non flexible piping would alleviate these pressure differences, but also inevitably reduce ease in iteration of the experimental set up. For this reason, the use of non flexible

tubing is suggested for future stages of the experimental set up, when the relative locations of the storage tank, pump, and channel are definitively determined.

The experimental fluid flow rate was determined by the rate set on the gear pump, which only provides an estimated flow output and does not account for the several sources of additional drag between the pump and test section. In addition to utilising non flexible tubing, future experiments should also include an electromagnetic flowmeter near the test section.

Experimental Scale

The OLME is a relatively small scale liquid metal experiment. The scale of the experiment was set based on the quantity of liquid metal available for use. Access to larger quantities of liquid metal will allow for a longer channel to be used in these experiments, where a fully developed, steady state flow could potentially be realised. This would make comparisons to literature and numerical simulations easier, but would be a significant and costly upgrade to the OLME. Use of larger scale flows would potentially reduce the challenges with flow height inconsistencies if variations in flow height are much smaller than the average flow height. Additionally, noise from the laser system would be less detrimental to data collection as the relative value of these noise signals would be small compared with the fluid thickness. Lastly, small vibrations in the system were monitored during magnet turn on and shut off, which caused small height shifts in the liquid metal due to channel shifting. This shift was removed in post processing but in the case of the transverse magnetic field these shifts were often the same magnitude as the expected MHD height changes, which made discernment of the experimental data less reliable particularly in the transverse field configuration. Increasing the scale of this experiment could produce more consistent height readings and should be pursued in the future; however, the cost implications are not insignificant and must be accounted for.

Nonuniform Surface Wetting and Surface Tension

Galinstan tends not to wet most materials, which leads to uneven flow spreading and dryout that is difficult to predict or prevent. Galinstan's high surface tension significantly contributes to the lack of adequate wetting. The presence of fully wetted versus partially wetted flow inevitably alters the fluid height values, which can affect the reproducibility

of data collection, especially at large channel angles. Additionally, when the liquid metal does not spread evenly across the surface, it becomes difficult to estimate fluid velocity from height measurements as the exact flow width is unknown. The inconsistency of the liquid metal wetting the channel walls also influenced the fluid height readings, as walls that were better wet formed a convex meniscus which reduced the centreline liquid metal height measurement (see Figure 5.21). Surface wetting was deemed a very significant challenge for liquid metal PFCs, and the next section describes contact angle measurements performed to better understand how galinstan surface wetting could be improved.

5.4 Challenges for Liquid Metal Flows

Surface wetting and flow spreading are key challenges for liquid metal flows. Lack of proper wetting can lead to the degradation of the underlying substrate material. For a flowing liquid metal PFC to operate under steady state fusion conditions, the liquid metal must reliably coat the entire PFC to prevent the plasma from directly striking the underlying solid substrate and mechanically compromising the substrate's structural integrity. A key example of the surface wetting issue was demonstrated at EAST in Hefei, China (126). A flowing liquid lithium limiter was placed radially in the EAST Tokamak. The lithium flows in streams down the channel surface, rather than evenly spreading, thus exposing the underlying solid substrate to incident plasma fluxes, as show in Figure 5.10 and 5.11. This phenomenon is also witnessed on the OLME with galinstan.

Due to their high surface tension and large contact angles, liquid metals typically do not wet surfaces uniformly. Full wetting implies complete mechanical, thermal and electrical contact between the liquid metal and substrate material. Without a sufficient electrical contact, there is no path for induced currents in the liquid metal to return through the side walls. For a flowing liquid metal plasma facing component to operate under steady state fusion conditions, the liquid metal must reliably coat the entire PFC to prevent the plasma from directly striking the underlying solid substrate and mechanically compromising the substrate's structural integrity. The concept of a flowing PFC relies on the liquid metal reliably coating the substrate material, so surface wetting and flow spreading are key priorities. This section

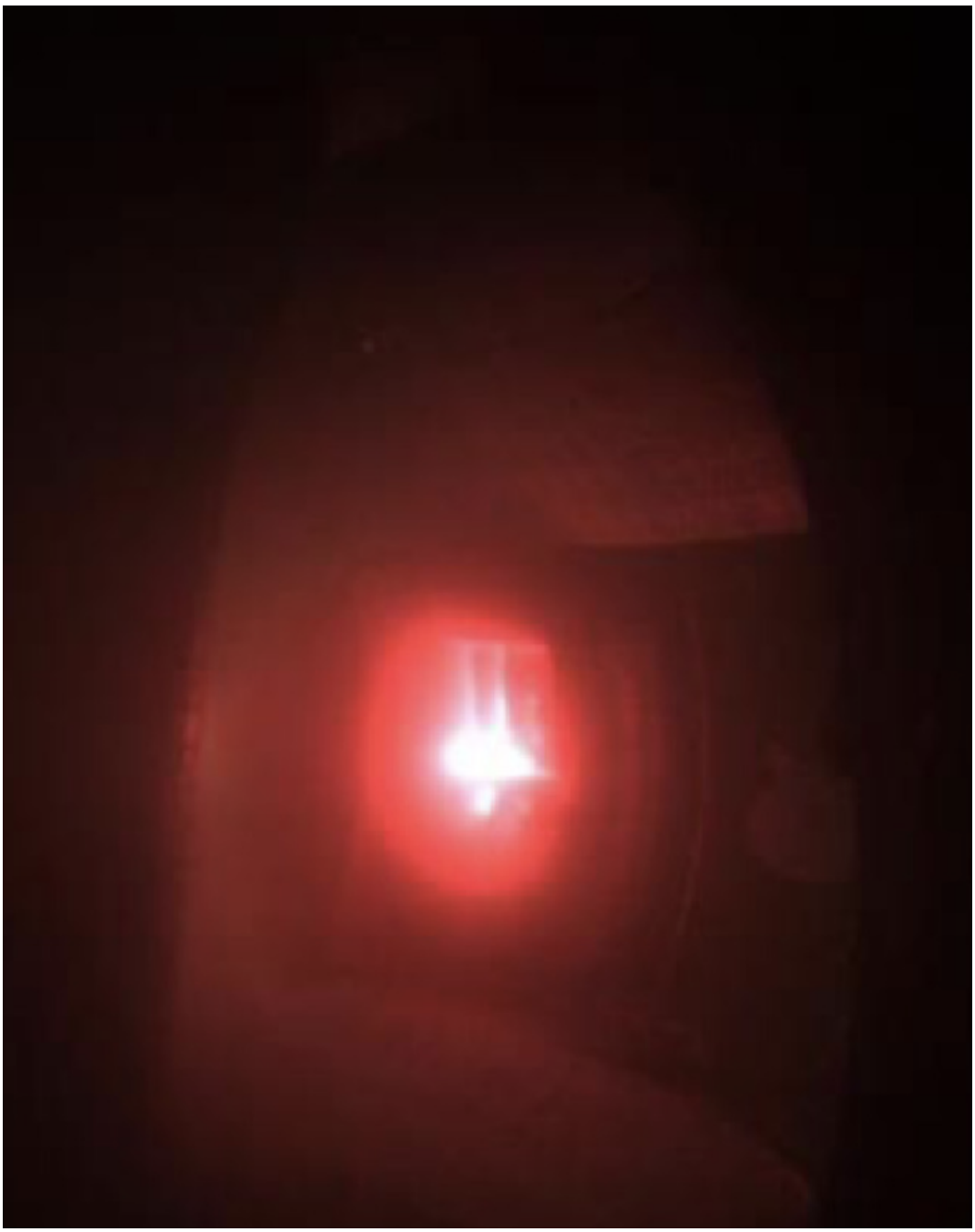


Figure 5.10: Image of the flowing liquid lithium limiter in the EAST tokamak, showing lithium flowing in streams down the limiter. Image from (127).



Figure 5.11: Image (from (127) of the liquid lithium limiter in air after the experiments conducted at EAST, showing in red outline the areas where lithium did not wet.

explores several techniques to improve liquid metal wetting, including surface roughness and channel design modifications.

5.4.1 Alternative Channel Designs

This section details iterations of the inlet, flow area and outlet designs to improve flow spreading. In this thesis, a 25 mm wide trench was used which attempts to avoid issues of wetting due to surface tension. However, during the channel design iteration process some work was completed to explore methods to improve liquid metal wetting across flat channel surfaces. The findings from that work are presented here.

Two larger channels were constructed, with dimensions similar to that of a divertor tile on the ST 40 tokamak. These channels were designed and built for exploring methods to optimise liquid metal wetting. The two additional channels differed only in the main flow area width: one was 18 cm wide and the other was 10 cm wide. The 10 cm wide channel was manufactured later to promote more even flow spreading. The updated channels were

composed of four separate pieces: the base channel, channel insert, plastic lid and inlet cover. The channel insert was the section that liquid metal will flow over. To allow ease in design iteration, this channel insert was mechanically separate from the rest of the channel so that different inlet designs, outlet designs, and surface roughnesses can be tested without replacing the entire channel.

Inlet and Outlet Region Iterations

The inlet and outlet designs are crucial in setting up conditions for galinstan to evenly flow across and drain from the channel. In the initial channel design, galinstan pooled in the outlet region due to inadequate draining. For the updated channel design, the outlet region had been redesigned from the original slot design to a sloped funnel design. The outlet region shape was modified from rectangular to triangular, and a 1.5 mm decrease in elevation was created from the main flow area to the outlet hole to add momentum to assist in fluid drainage. This allowed galinstan to better funnel into the outlet from the main flow area and quickly drain from the outlet hole. Also, the outlet hole was made larger than the inlet hole to prevent accumulation of liquid metal on the channel surface. For the 18 cm wide flow area channel, the inlet hole is 1/4" bsp and the outlet is 3/8" bsp. For the 10 cm wide flow area channel, the inlet hole was 1/2" bsp and the outlet hole was 3/4" bsp. This design was effective in adequately draining galinstan from the channel.

The inlet region was designed similar to the outlet region. There is a 1.5 mm increase in elevation from the inlet hole to the main flow area to slow the flow as it enters the channel region and allow for more flow spreading. To further enhance flow spreading, the utilisation of striations and posts to promote more uniform mixing of the galinstan was explored using the original channel design.

The use of posts or striations on the channel surface was of particular interest because of the TEMHD effect which can be used to drive liquid metal flow through trenches in the presence of a temperature gradient along the channel height (108). To better understand the effects of posts or striations on liquid metal flow without the presence of TEMHD, the use of striations and posts in the inlet region was tested using the updated channel design. A striated inlet design was tested for the 180 mm flow area channel, and a posted inlet design

was tested for the 100 mm flow area channel. The striated inlet had 17, 1 mm tall evenly spaced striations, and the inlet design with posts had 2 mm x 2 mm posts that were 1 mm tall. To encourage flow spreading, the channels created by the striations were gradually split in half as the galinstan flows from the inlet region to the main flow area. Similarly, the posts were arranged in a staggered array to promote more flow mixing. Side-by-side comparisons of the two channels are shown in Figure 5.12.

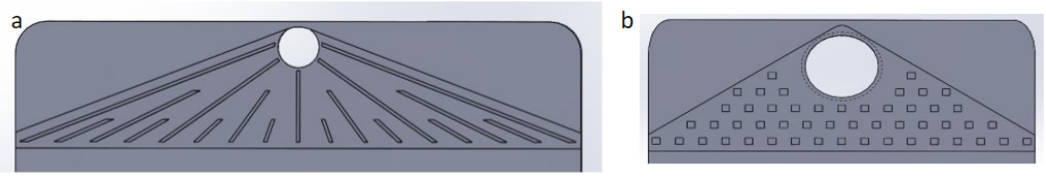


Figure 5.12: Side by side comparison of the **a)** striated inlet design used on the 180 mm flow area width channel and **b)** staggered post inlet design used on the 100 mm flow area width channel.

For these experiments, galinstan was pumped at 300 ml/min and the channels were placed at a 4° angle. The inlet hole in Figure 5.12 b was double the size of that in a, but literature suggests that the inlet width has negligible effect on the resultant stream width (128). Regardless, comparisons of flow stream width were taken cautiously, and suggested that use of the staggered posts increased resultant flow stream width. Comparison of downstream flow behaviour clearly shows that the presence of staggered posts in the inlet region produces more uniformly spread downstream flow than the striated inlet design. This was likely due to the posts aiding in reducing the upstream pressure gradients and transient perturbations that can cause reduced wetting. From Figure 5.13, which shows galinstan flowing down the striated versus posted inlet channels, it was clear that the presence of the posts produced more uniformly spread downstream flow compared to the striations. The cause of this improved downstream behaviour can be linked to contact line theory- the presence of staggered posts assisted in equalising any miniscule pressure gradients that exist upstream in the galinstan loop, thus preventing downstream de-wetting.

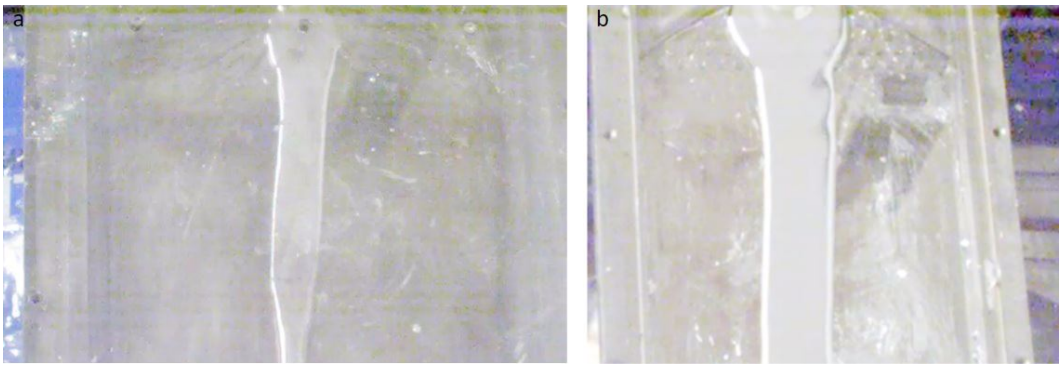


Figure 5.13: Galinstan at 300 ml/min flowing down a) the 180 mm wide channel with striated inlet and b) the 100 mm wide channel with inlet posts, both at a 4°angle.

The striations did spread the liquid metal out slightly from the inlet hole, but the liquid metal still did not evenly fill the inlet region. The liquid metal preferentially followed some striated channels rather than others, which meant some parts of the inlet were well wetted and others were dry. While the striations provide solid guidelines to direct the liquid metal flow, these rigid lines prevented further mixing of the flow. For the posts, the galinstan did mix more randomly, but preferential flow channels were still developed. Overall, the inlet structure appeared to have a minimal impact on the resultant flow patterns for galinstan. Accordingly, a completely flat channel, void of posts or striations, was used at OLME to collect data.

Inlet Cover (Flow Spreader)

A flow spreader was include in this channel design to sandwich the entire inlet region. This spreader extended for 1 cm of the main channel flow region (see Figure 5.14). There was a 2mm gap between channel surface and the flow spreader. This 2mm gap forced the liquid metal to spread more fully.

A comparison of galinstan flow at several angles ranging from 0° to 7° was conducted to understand the impact of this flow spreader on galinstan film development. In each trial, galinstan was pumped at 300 ml/min and exposed to ambient air. For a horizontal channel, galinstan spread evenly so the effect of the inlet flow spreader were negligible. However, even slight (0.15°) increases in channel angle caused galinstan to flow in a narrow stream down the channel. When the inlet flow spreader was in place, several streams occur rather than just one (see Figure 5.15). This behaviour was reproducible at all tested channel angles

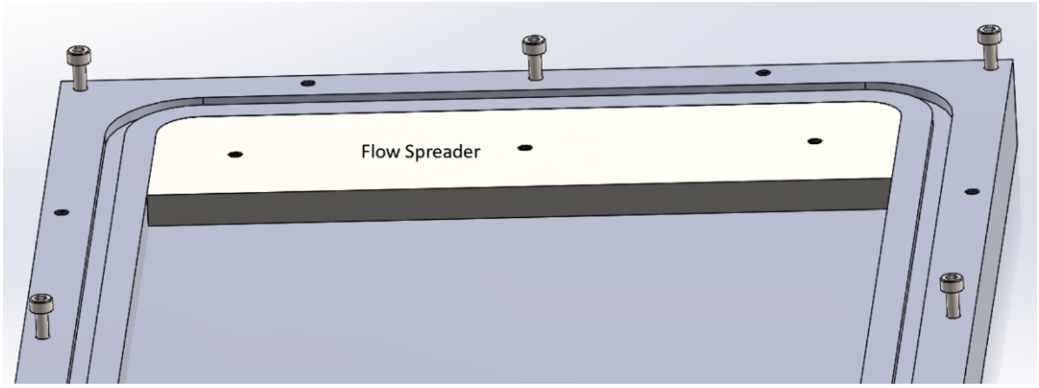


Figure 5.14: View of the updated galinstan flow spreader, with a 2mm gap between the flow spreader's lower edge and the surface of the main flow area

above 0°. As expected, the inlet cover did spread the galinstan flow out more due to the added downward pressure on the fluid that causes enhanced spreading. However, the flow still did not spread evenly in the inlet region, which results in galinstan streams down the channel. Additional mechanisms in the inlet region are required to better distribute the galinstan flow in the inlet region to force galinstan to flow evenly.

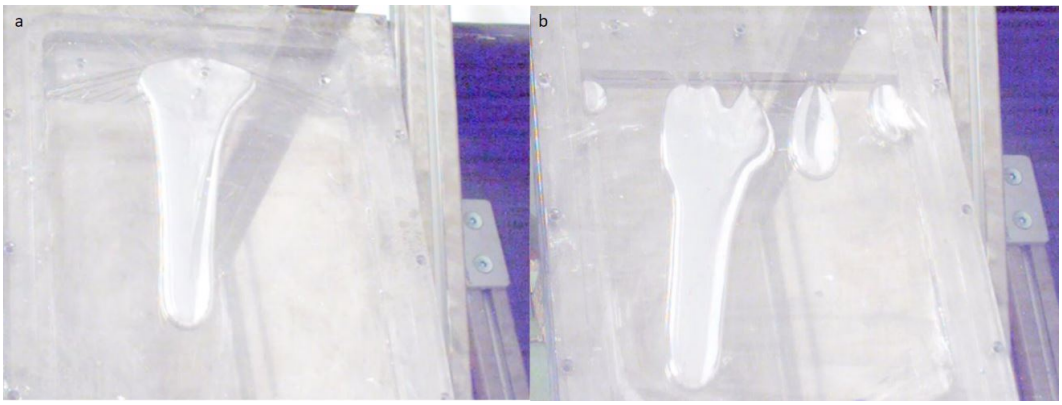


Figure 5.15: Comparison of a) galinstan flow without the inlet cover and b) galinstan flow with the inlet cover, both at 7°.

From this survey, the key findings were:

1. Increasing channel angle decreases flow spreading up to 7°, after which channel angle effects plateaued

2. The presence of posts in the flow development region prevented downstream de-wetting.

3. A larger outlet hole than inlet hole promoted suitable draining.

4. The presence of a flow spreader produced more spread out galinstan films (though not evenly).

5.4.2 Contact Angle Theory and Measurements

A major challenge in liquid metal hydrodynamics is inadequate surface wetting. Liquid metals are high energy liquids due to strong metallic bonding that causes liquid metals to experience large intermolecular forces (129). This results in high surface tensions for liquid metals and low surface wetting. The remainder of this section details efforts to improve the uniform wetting of flowing liquid metal.

5.4.3 Contact Angle Measurements

Contact Angle Theory

The tendency of a liquid to wet a surface can be quantified by the contact angle. This measurement varies based on several factors such as the surface chemical composition and roughness. Contact angles below 90° signify wetting of the surface, and contact angles above 90° are described as non-wetting. In nonwetting fluids, the magnitude of the fluid's intermolecular, cohesive forces outweigh the adhesive forces between the liquid metal and solid substrate. This leads to the fluid molecules preferentially attracting to each other rather than to the substrate.

Contact Angle Measurements

Due to the lack of data existing measuring the contact angle of galinstan on various surface roughnesses, these measurements were made at the OLME. Various surface roughnesses were tested at OLME to understand the effect of surface roughness on galinstan wetting behaviour. A simplified procedure for measuring the contact angle adapted from (130) was used to measure contact angles in this study. Three 316-stainless steel channels were manufactured by Get It Made[1] with surface roughness: 0.05 micron roughness average (Ra), 0.53 micron Ra and 1.27 micron Ra, as seen in Figure 5.16. The stainless steel channels were

[1] Getitmade is a machining specialist based in London, UK

viewed horizontally by a 5.3 Megapixel (2592x2048) DFK 33UP5000 complementary metal oxide semiconductor (CMOS) camera equipped with an 8 mm focal length lens. An ultraviolet (UV) torch placed behind a plastic translucent sheet was used to create roughly uniform background lighting for the experiment. Ambient light was switched off and droplets were placed on the surface using a 1ml syringe equipped with a 12.7 mm needle. Drops were made 60 mm away from the camera lens.

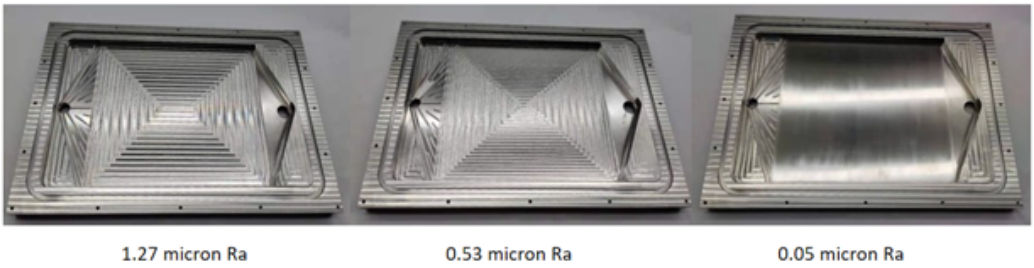


Figure 5.16: Image of three channel inserts made of 316 stainless steel with 1.27, 0.53, and 0.05 micron average surface roughness

Contact angle was determined using a simplified contact angle equation (Equation 5.1) with parameters described in Figure 5.17, as suggested by (131). These contact angle measurements were confirmed using the Image J[2] contact angle plug in (132). Droplet width and height was measured from CMOS image data using IC Measure software. An example of the data collected is shown in Figure 5.18. Results are shown in Table 5.2.

Table 5.2: Results from Contact Angle Measurements

Surface Roughness (Microns)	**Contact Angle (Degrees)**
0.05	118
0.53	134
1.27	146

$$\theta = 2\arctan\frac{2H}{D} \tag{5.1}$$

Gallium oxides form on the surface of galinstan when exposed to air and tend to coat the outside surface of the galinstan body. Oxidized galinstan will appear to have a lower contact angle than non-oxidized galinstan, due to the presence of this coating, as shown in Figure

[2]ImageJ is an open-source, java based programme used for image processing developed by Wayne Rasband.

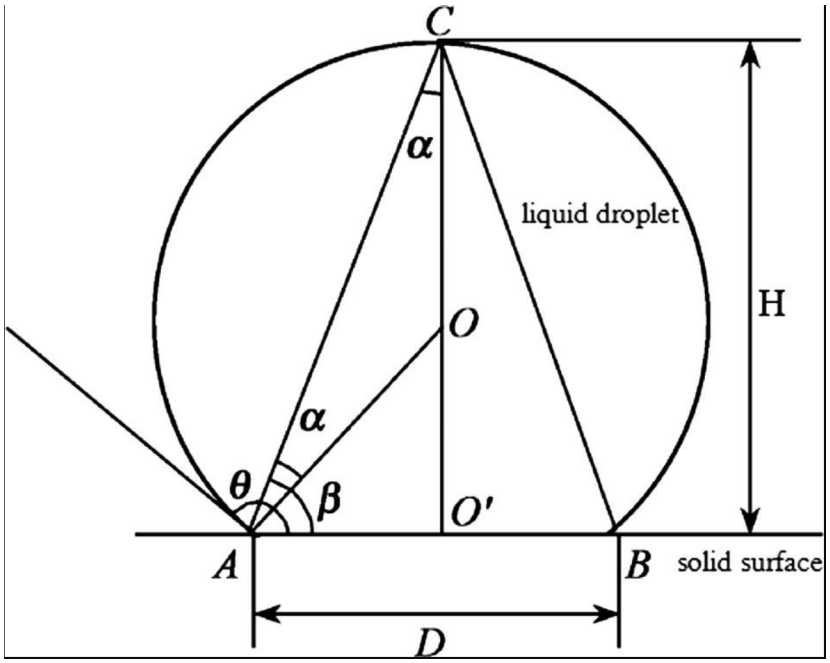


Figure 5.17: Contact angle measurement parameters for a droplet of gallium (131)

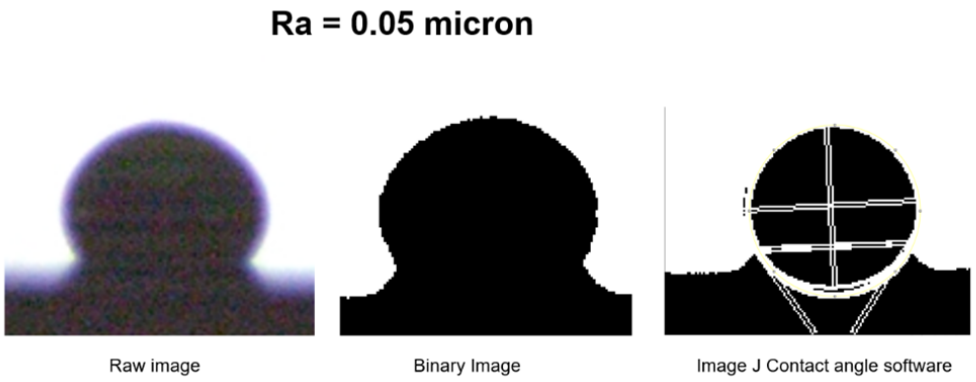


Figure 5.18: Example of contact angle measurement of liquid galinstan on a 0.05 micron average surface roughness stainless steel channel.

5.19. Experiments were performed in air for simplicity, as the exact contact angle was not of interest- solely the relationship between surface roughness and contact angle.

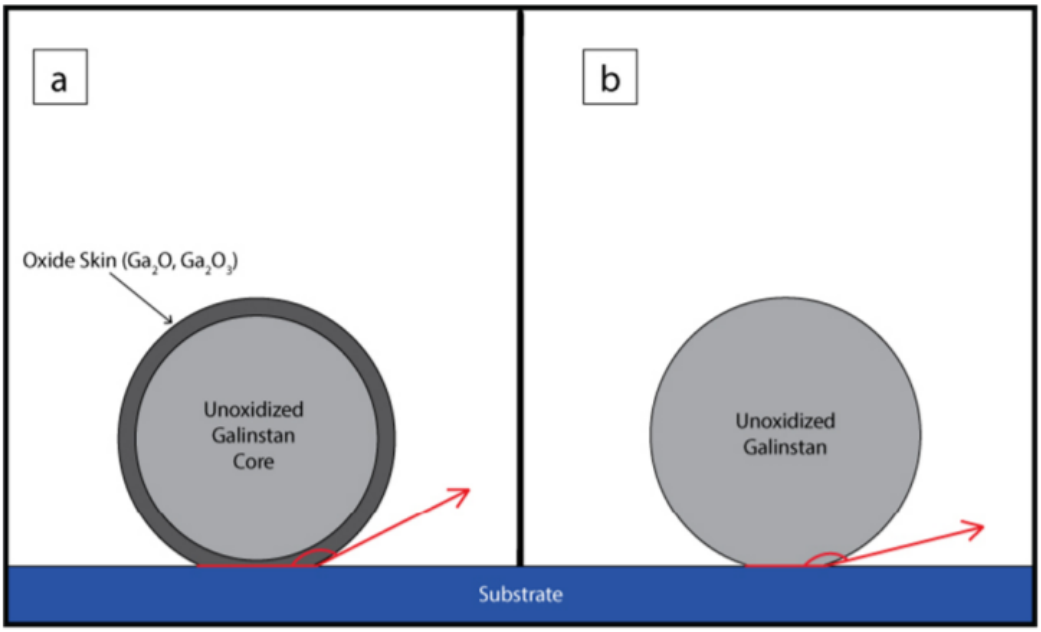


Figure 5.19: Sketch of oxidised (a) and unoxidised (b) galinstan on a substrate material (133)

The contact angle decreased with a decreasing surface roughness, which suggested that substrate surface roughness should be minimised to enhance liquid metal wetting. A comparison of the contact angles found in this study (galinstan in air on stainless steel) to other gallium based contact angles measurements with metals is shown on Figure 5.20. From this figure, it was clear that galinstan was non-wetting on purely metallic surfaces. The results collected from this experiment showed higher contact angles than similar measurements performed by other authors, possibly due to the cleaning solution used to wipe the stainless steel surface between each trial increasing the surface energy of the stainless steel.

The use of chemical surface treatment has also been shown to reduce the contact angle further and allow for full channel wetting (131, 135). Accordingly, the stainless steel surfaces were treated in a 0.5M hydrochloric acid bath for 24 hours to support more uniform stainless steel wetting. This led to even galinstan wetting of a wide channel, rather than rivulet flow down the channel. Additionally, the meniscus formed at the wall changed from convex to concave, which suggested that the galinstan was better wetting the sidewalls as well (see Figure 5.21).

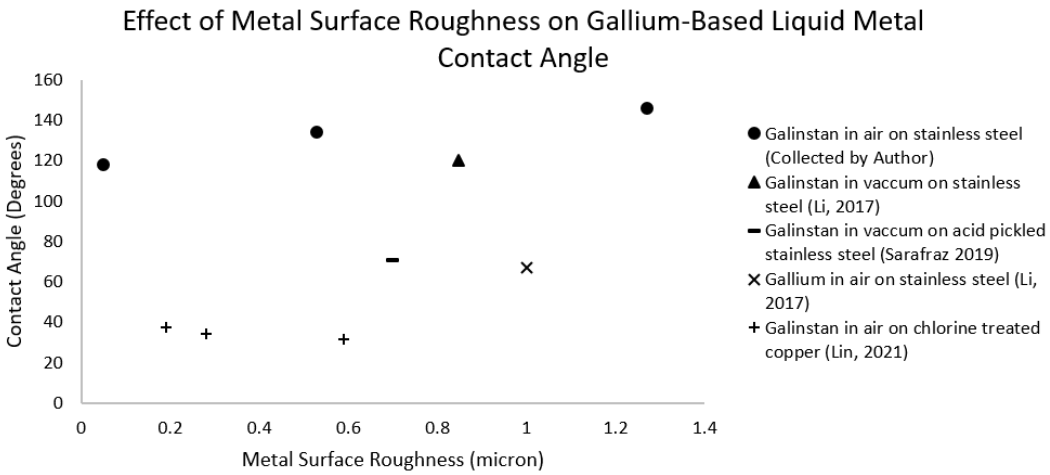


Figure 5.20: Comparison plot of gallium based liquid metal contact angles on various metals. Data collected at OTI is represented by the black circles, all other data is sourced from literature review (131, 133, 134, 135).

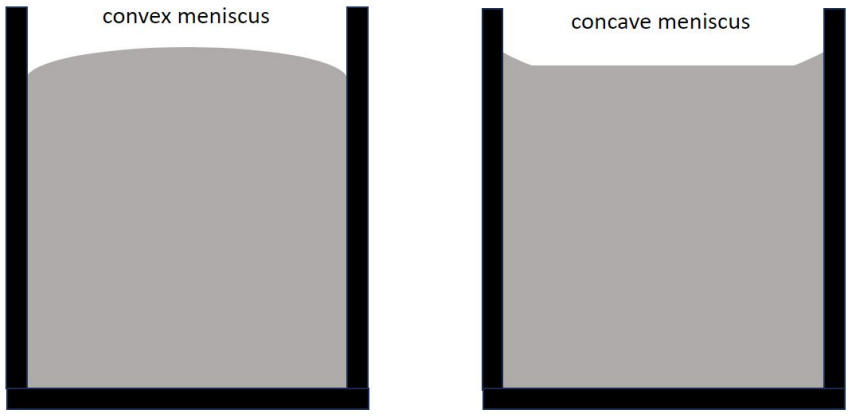


Figure 5.21: Visualisation of convex vs. concave meniscus

It is important to note that in the context of a fusion reactor, liquid lithium would be the likely candidate for a flowing liquid metal system. Lithium also exhibits a high contact angle on metallic surfaces (130° contact angle at 230°C) (136). Wetting behaviour has been shown for liquid lithium systems heated above 315°C for a stainless steel substrate with surface roughness of 0.028 micron (108). It is unknown if this same phenomena occurs for galinstan. A slight dependence of gallium contact angle on temperature is suggested by (135), but no temperature dependence is noted by (133) for galinstan on stainless steel up to 300°C. A study of galinstan contact angle dependence on temperatures above 300°C is a potential area for future work. Overall, the results from this section confirm that surface roughness should be kept at a minimum to promote more uniform spreading of liquid metal flow.

5.4.4 Dynamic Surface Wetting

Chapter 5 presents static contact angle measurements made on the OLME. In addition to the static contact angle, the dynamic surface wetting of flowing liquid galinstan on three stainless steel surfaces was also explored and is presented in this section. In a tokamak, a variety of flow angles could be present. For example, the JET divertor is composed of channels placed at a variety of angles (see Figure 5.22). Therefore, the effects of channel angle on flow must be well understood.

A series of experiments are performed to investigate the effects of channel angle and surface roughness on resultant stream width. Five channel angles: 1.95, 4.5, 7.15, 9.85, and 12.5 are tested. In these experiments, galinstan is pumped down the stainless steel channel at 300 ml/min in an inert argon environment at each angle and with each of the three surface roughness channels. Stream width measurements are made using the IC measure software and a camera. The degree of channel cleaning between each trial can have significant impacts on the resultant flow patterns for successive trials (138), so the substrate was wiped clean with a cloth between trials.

Qualitative comparisons (see Figure 5.23) of galinstan flow at different surface roughnesses clearly shows the trend of reducing flow stream width with increasing surface rough-

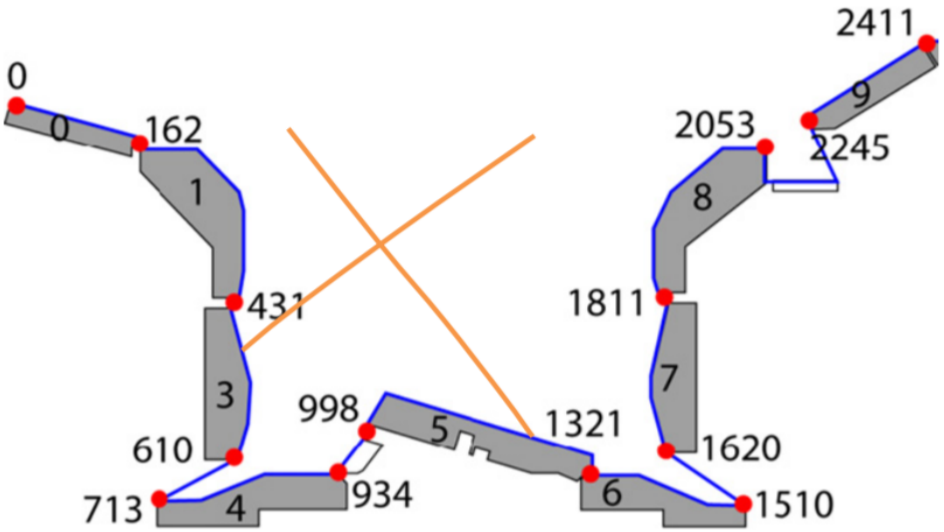


Figure 5.22: Schematic of the divertor design and strike point position for the JET tokamak, from (137).

ness. This further supports the claim that the surface roughness should be minimised to promote flow spreading.

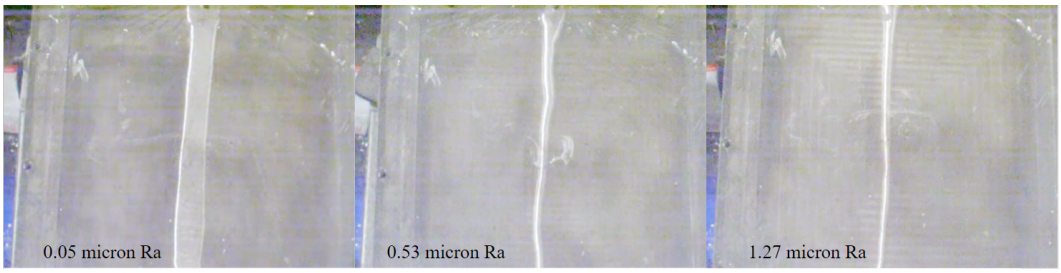


Figure 5.23: Galinstan streams flowing down stainless steel channels at a variety of surface roughness at channel angle 7°.

Qauntitative comparisons of flow stream width as a function of channel angle and surface roughness are shown in Figure 5.24. The results show a general decrease in resultant stream width with channel angle increase. Above 7°, this effect appeared to plateau suggesting a balancing of gravitational and surface tension forces.

Gravity is a key factor in studies of flow down an incline plane. In the case of a fully horizontal channel, gravity acts normal to the channel surface and causes the liquid to spread evenly across the substrate surface. This was confirmed experimentally. Even slight (0.15°) channel angles led to galinstan flowing in streams rather than uniformly. This is visualised in Figure 5.25, where galinstan was flowing across a horizontal channel versus a 1° channel

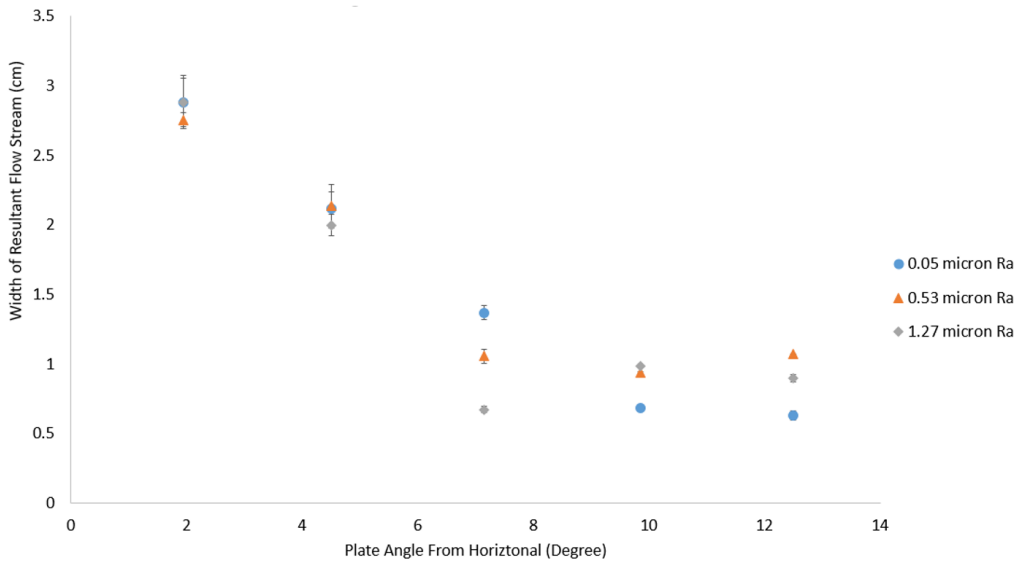


Figure 5.24: Galinstan streams flowing down stainless steel channels at a variety of surface roughness. Results from a fully horizontal channel are not shown, as this case led to full wetting at all surface roughnesses.

angle, both using the 0.05 micron surface roughness channel. At non-horizontal angles, gravity both spread and accelerated the fluid film, leading to a reduction in stream width.

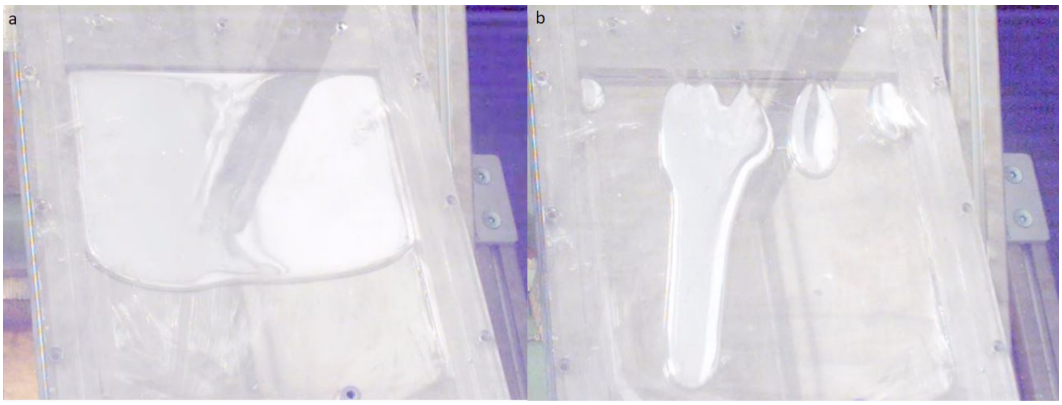


Figure 5.25: Galinstan flowing from the inlet hole down **a)** a flat channel and **b)** a channel at 1°, both at 0.05 micron surface roughness.

Additionally, as the channel angle increased, the surface roughness had a more dominant effect on the spreading of the liquid metal. Further investigation of this pattern is warranted.

In addition to surface roughness, surface material and geometric surface structure can be modified to alter the contact angle (133). For example, copper has the highest surface energy of all the metals, so contact angles on copper surfaces are expected to be less than those on stainless steel. At UIUC, techniques such as argon plasma cleaning, laser channel texturing,

and the use of mesh-like structures have been shown to improve lithium wetting (83, 139).

In the scenario where the channel is fully wetted with liquid metal prior to starting the pump, the liquid metal tends to uniformly cover the channel surface. Accordingly, determining methods to adequately and sustainably pre-wet the substrate surface would be very useful to ensure liquid metal spreading.

5.5 Summary

This chapter presented a novel quantitative comparison of experimental, analytical and numerical MHD height changes across a flat channel in the presence of a surface normal magnetic field. The MHD height change due to surface normal magnetic field was quantitatively measured experimentally for the first time, and compared with transverse field effects to confirm that the surface normal field has the dominant effect. In general, the trends of increasing MHD height change with increasing Hartmann number predicted from analytical and numerical solutions were confirmed, particularly for higher Hartmann number cases. Also, a critical Hartmann Number of 14 was determined, above which the MHD height change was monotonic. The chapter also included a summary of areas for improvement for the OLME, including contact angle measurements for galinstan which were compared to values from the literature. Several iterations of channel designs showed that reducing surface roughness improves galinstan wetting on stainless steel, and inlet design has only marginal impact on fully developed liquid metal flow patterns. Overall, this chapter served to provide an experimental backing to the theoretical phenomena predicted for liquid metal flows utilising the new OLME facility and provided novel experimental quantitative measurements of the effect of a surface normal magnetic field on liquid metal height.

Chapter 6

SUMMARY AND CONCLUSION

The work presented in this thesis describes the construction of a new experimental facility added to the blossoming liquid metal PFC landscape. The concept and design rationales were stated alongside the practical construction mechanisms. The goal of building the OLME was to develop a robust and safely operated experiment where the impacts of magnetic field magnitude and orientation could be exhaustively studied. In this thesis, the impacts of liquid metal flow rate and magnetic field strength were of significant interest and were presented experimentally, analytically, and numerically for the case of surface normal magnetic field.

It was of great importance to the author to accompany this new experimental facility with an accessible numerical model. This model provides a cheap and efficient route to optimise various experimental factors. The process of numerical model development was described in detail, and the numerical model was validated against both established and new analytical solutions. A strategic scaling up in model complexity ensured that the physics of the solver was well understood and troubleshoot before adding additional factors to the model. The results of this model were compared to experimental data collected on the OLME and showed agreement in trends. The key conclusions from this chapter are further elaborated in the next section.

6.1 Summary of Major Themes and Assessment of Aims

6.1.1 OLME Development

A novel experimental facility, the OLME was designed and built to quantitatively measure the effect of surface normal magnetic field and flow rate on free surface liquid metal height. This experiment consisted of liquid galinstan flowing through a gear pump onto a copper channel. The electromagnet was custom built in collaboration with Woodruff Scientific to allow for visual access to the liquid metal free surface in both the transverse and surface normal magnetic fields. The magnetic field profile was modelled using finite element modelling and experimental operation was in agreement with this model. Additionally, a robust safety system was built and implemented to allow for fail safe operation of the equipment. A Labview programme was written to ease the operation of the OLME.

It is of notice that the OLME was designed to allow for testing of various field strengths and orientations that have not yet been explored fully, such as a gradient magnetic field resembling of the 1/r field in a tokamak. Additionally, the impact of channel angle remains areas of future research. To understand the coupled influence of channel angle, flow rate, and magnetic field on liquid metal flow, further experimentation is recommended to generate a useful correlation.

6.1.2 Analytical and Numerical Modelling of OLME Experimental Set Up

ANSYS CFX[1], a commercial CFD programme, was used to create a model of liquid metal flow on the OLME. Firstly, this software was validated for low aspect ratio geometry, fully developed 2D duct flow against established analytical solutions. The simple 2D model of fully developed, MHD duct flow with insulated walls showed excellent agreement with the Hunt analytical solution (41). The expanded model including conductive Hartmann walls also showed excellent agreement with the relevant Hunt analytical solution. Next, the model was expanded to incorporate a pseudo free surface with transverse and surface normal fields,

[1] www.ansys.com

showing reasonable agreement with Shishko and Miyazaki, respectively, (42, 43). The increased error was attributed to the use of analytical solutions that assumed thin walls, though thick walls were present in this study, and the use of a low aspect ratio geometry. Finally, a 3D model was generated to allow for a true free surface, and developing flow was modelled using a transient solver. An analytical solution for free surface, developing flow reported by Sun was expanded upon to account for surface normal magnetic field effects (45). This 3D numerical model was compared with the newly developed analytical solution and showed reasonable agreement despite several simplifications assumed in the analytical solution explained in Chapter 4. Comparing numerical and analytical depth change as a function of Hartmann number showed that the numerical solution more accurately predicted MHD behaviour as the numerical results more closely approach 0 depth change at Hartmann number = 0. The analytical solution likely overestimates MHD behaviour because MHD effects were incorporated using a pressure drop formula that assumes fully developed rather than developing flow.

Overall, this modelling work significantly increases the usefulness of the OLME by providing an easy route for scaling experimental results to fusion relevant conditions and modelling parameters difficult to achieve experimentally.

6.1.3 Analytical, Numerical, and Experimental Result Comparison

Experimental measurements of liquid metal height change in response to surface normal magnetic field at various flow rates were collected and compared with analytical and numerical predictions. An agreement in the trend of increasing height change for increasing Hartmann number was shown amongst all three methods, suggesting the analytical and numerical modelling captured most of the underlying physics. A critical Hartmann number of 14 was determined, above which a monotonic increase in liquid metal height due to a surface normal magnetic field was determined. Differences in the magnitude of the experimental height changes were proposed to be due to galinstan and copper oxidation, unaccounted for pressure gradients along the liquid metal loop, galinstan's high surface tension, and the small scale of the experiment. This study provided the first quantitative measurement of surface

normal magnetic field impact on liquid metal height, and confirmed analytical predictions that the surface normal field has the dominant effect on liquid metal height change.

To better understand surface wetting dynamics, contact angle measurements were made on channels with various measured surface roughness values and compared with similar measurements from the literature. The impact of inclining the channel was also explored, showing a tendency for rivulet formation as the channel angle increased until a plateau was reached at 7°. Alternative channel designs were explored, including various inlet and outlet designs to promote flow spreading. As the OLME is a new facility, some work remains in improving the experimental design as well as the numerical model to better represent experimental conditions. This thesis presents only the very beginning of possible experimental data collection on the OLME.

The field of liquid metal PFCs remains an exciting one because there is much more remaining to actualise this concept. The next chapter includes recommendations for future work.

Chapter 7

RECOMMENDATIONS

This thesis presents a synchronous analytical, numerical and experimental study of MHD effects on liquid metal flow, and an unprecedented quantitative study of surface normal field effects on liquid metal Flow. However, the work presented here is only the cusp of what is achievable on the OLME. This chapter highlights key suggestions for future experiments to perform on the OLME to further explore the impacts of magnetic field on liquid metal flow and feasibility of liquid metals for future PFCs. This is followed by suggestions to improve the analytical and numerical models to better simulate experimental behaviour. This serves as a roadmap guiding future research efforts.

7.1 Suggested Improvements to the OLME

1. Investigate alternative methods of measuring depth that are more compatible with measuring liquid metal surfaces and produce less noise.

2. Build an electromagnetic pump and electromagnetic flowmeter. Gear pumps require constant maintenance when using with liquid metal that has some amount of oxidation which leads to clogging. An electromagnetic pump and accompanying flowmeter will improve the fluid flow rate estimations and reduce system maintenance caused by galinstan oxidation.

3. Explore methods to measure induced current generation. Experimental measurement

of induced current will assist in calibrating the numerical model to account for the impact of oxidation on the OLME.

4. Incorporate a method to track fluid velocity alongside fluid height. A method of tracking fluid velocity using frozen gallium particles was preliminary studied at OTI and is detailed future work in Chapter 3.

7.2 Suggested Future Experiments

7.2.1 MHD Experiments

1. Develop an empirical correlation for fluid height as a function of flow rate, channel angle, and magnetic field. The determination of this correlation is beyond the scope of this thesis due to the limited Hartmann and Reynolds numbers tested, but such relationship would likely take the form of Equation 7.1, adapted from suggested groupings in (82).

2. Investigate the impact of transverse field on liquid metal height, using higher flow rates to increase the MHD height change to a measurable value.

3. Investigate the impact of 1/r field on liquid metal height.

4. Exploring transient magnetic field effects to model ramp up/down of magnets in a fusion device.

$$\varepsilon = f(Re, Ha, \alpha) \tag{7.1}$$

7.3 Suggested Improvement for the Analytical and Numerical Models

1. Derive a formula for MHD pressure drop that is specific for the case of developing flow, and integrate this into the analytical solution for developing flow in the presence

of a surface normal field that was presented in this thesis.

2. Derive an analytical solution for developing free surface flow on an incline in the presence of surface normal magnetic field and an generate accompanying numerical solution.

3. Incorporate oxidation effects (stagnant free surface, reduced electrical conductivity) to better estimate fluid flow across the channel.

4. Test numerical model at fusion relevant Hartmann numbers

References

[1] ODDS Cf. Transforming our world: the 2030 Agenda for Sustainable Development. *United Nations: New York, NY, USA*, 2015.

[2] Remus Prăvălie and Georgeta Bandoc. Nuclear energy: Between global electricity demand, worldwide decarbonisation imperativeness, and planetary environmental implications. *Journal of environmental management*, 209:81–92, 2018.

[3] Samuele Meschini, Francesco Laviano, Federico Ledda, Davide Pettinari, Raffella Testoni, Daniele Torsello, and Bruno Panella. Review of commercial nuclear fusion projects. *Frontiers in Energy Research*, 11:1157394, 2023.

[4] Abbas Azarpour, Suardi Suhaimi, Gholamreza Zahedi, and Alireza Bahadori. A review on the drawbacks of renewable energy as a promising energy source of the future. *Arabian Journal for Science and Engineering*, 38:317–328, 2013.

[5] Louis K Mansur, AF Rowcliffe, RK Nanstad, SJ Zinkle, WR Corwin, and RE Stoller. Materials needs for fusion, Generation IV fission reactors and spallation neutron sources–similarities and differences. *Journal of Nuclear Materials*, 329:166–172, 2004.

[6] JPHE Ongena and G Van Oost. Energy for future centuries: prospects for fusion power as a future energy source. *Fusion Science and Technology*, 61(2T):3–16, 2012.

[7] Samuele Meschini. Sustainability of compact, high magnetic field fusion reactors: environment, society, and economy. *Fresnius Environmental Bulletin*, 30(6):5974–5984, 2021.

[8] John Wesson and David J Campbell. *Tokamaks*, volume 149. Oxford university press, 2011.

[9] J Ongena, R Koch, R Wolf, and H Zohm. Magnetic-confinement fusion. *Nature Physics*, 12(5):398–410, 2016.

[10] Yuhong Xu. A general comparison between tokamak and stellarator plasmas. *Matter and Radiation at Extremes*, 1(4):192–200, 2016.

[11] Shutaro Takeda and Richard Pearson. Nuclear fusion power plants. *Power Plants in the Industry*, 2018.

[12] Shunjie Li, H Jiang, Zhigang Ren, and C Xu. Optimal tracking for a divergent-type parabolic pde system in current profile control. In *Abstract and Applied Analysis*, volume 2014, page 940965. Wiley Online Library, 2014.

[13] M Huguet. The iter magnet system. *Fusion Engineering and Design*, 36(1):23–32, 1997.

[14] Davin Lunz. *Dynamics and stability of a thin liquid lithium flow within a tokamak divertor*. PhD thesis, University of Oxford, 2019.

[15] *World Survey of Fusion Devices 2022*. Non-serial Publications. International Atomic Energy Agency, Vienna, 2023. ISBN 978-92-0-143422-7. URL https://www.iaea.org/publications/15253/world-survey-of-fusion-devices-2022.

[16] Francesco Romanelli, P Barabaschi, D Borba, G Federici, L Horton, R Neu, D Stork, H Zohm, et al. Fusion Electricity: A roadmap to the realization of fusion energy. 2012.

[17] Y Zhai, A Otto, and M Zarnstorff. Low cost, simpler HTS cable conductors for fusion energy systems. In *IOP Conference Series: Materials Science and Engineering*, volume 1241, page 012023. IOP Publishing, 2022.

[18] S McNamara, O Asunta, J Bland, PF Buxton, C Colgan, A Dnestrovskii, M Gemmell, M Gryaznevich, D Hoffman, F Janky, et al. Achievement of ion temperatures in excess of 100 million degrees Kelvin in the compact high-field spherical tokamak ST40. *Nuclear fusion*, 63(5):054002, 2023.

[19] Binfu Gao, Rui Ding, Hai Xie, Long Zeng, Ling Zhang, Baoguo Wang, Changjun Li, Dahuan Zhu, Rong Yan, and Junling Chen. Plasma-facing components damage and its effects on plasma performance in EAST tokamak. *Fusion Engineering and Design*, 156:111616, 2020.

[20] John Wesson and David J Campbell. *Tokamaks*. Oxford university press, 2005.

[21] Thomas Eich, AW Leonard, RA Pitts, W Fundamenski, Robert James Goldston, TK Gray, A Herrmann, A Kirk, A Kallenbach, O Kardaun, et al. Scaling of the tokamak near the scrape-off layer H-mode power width and implications for ITER. *Nuclear fusion*, 53(9):093031, 2013.

[22] JW Coenen, S Antusch, M Aumann, Wolfgang Biel, J Du, J Engels, S Heuer, A Houben, T Hoeschen, B Jasper, et al. Materials for DEMO and reactor applications—boundary conditions and new concepts. *Physica Scripta*, 2016(T167):014002, 2015.

[23] MA Abdou, A Ying, N Morley, K Gulec, S Smolentsev, M Kotschenreuther, S Malang, S Zinkle, T Rognlien, P Fogarty, et al. On the exploration of innovative concepts for fusion chamber technology. *Fusion Engineering and Design*, 54(2): 181–247, 2001.

[24] H Bolt, V Barabash, W Krauss, J Linke, R Neu, S Suzuki, N Yoshida, ASDEX Upgrade Team, et al. Materials for the plasma-facing components of fusion reactors. *Journal of nuclear materials*, 329:66–73, 2004.

[25] Jochen Linke, Juan Du, Thorsten Loewenhoff, Gerald Pintsuk, Benjamin Spilker, Isabel Steudel, and Marius Wirtz. Challenges for plasma-facing components in nuclear fusion. *Matter and Radiation at Extremes*, 4(5), 2019.

[26] CE Kessel, D Andruczyk, JP Blanchard, T Bohm, A Davis, K Hollis, PW Humrickhouse, M Hvasta, M Jaworski, J Jun, et al. Critical exploration of liquid metal plasma-facing components in a fusion nuclear science facility. *Fusion Science and Technology*, 75(8):886–917, 2019.

[27] Rion A Causey. Hydrogen isotope retention and recycling in fusion reactor plasma-facing components. *Journal of Nuclear Materials*, 300(2-3):91–117, 2002.

[28] Daniel Andruczyk, Andrew Shone, Zachariah Koyn, and Jean Paul Allain. First lithium experiments in hidra and evidence of helium retention during quasi-steady-state stellarator plasma operations. *Plasma Physics and Controlled Fusion*, 64(8):085011, 2022.

[29] Andrew Shone, Rabel Rizkallah, Daniel O'Dea, Brandon Kamiyama, and Daniel Andruczyk. In-operando lithium evaporation inducing helium retention in long-pulse hidra helium plasmas. *Journal of Fusion Energy*, 42(2):43, 2023.

[30] JS Hu, GZ Zuo, J Ren, QX Yang, ZX Chen, H Xu, LE Zakharov, R Maingi, C Gentile, XC Meng, et al. First results of the use of a continuously flowing lithium limiter in high performance discharges in the EAST device. *Nuclear Fusion*, 56(4):046011, 2016.

[31] RW Moir. Liquid first walls for magnetic fusion energy configurations. *Nuclear Fusion*, 37(4):557, 1997.

[32] John Arthur Shercliff. Textbook of magnetohydrodynamics. 1965.

[33] Shuzo Oshima, Ryuichiro Yamane, Yoshihiro Mochimaru, and Kouzo Sudo. Investigation of film flow of a conducting fluid in a transverse magnetic field: 2nd report, rivulet in a non-uniform magnetic field. *Bulletin of JSME*, 29(253):2078–2085, 1986.

[34] Din-Yu Hsieh. Stability of a conducting fluid flowing down an inclined plane in a magnetic field. *The Physics of Fluids*, 8(10):1785–1791, 1965.

[35] Yu P Ladikov. Flow stability of a conducting liquid flowing down an inclined plane in the presence of a magnetic field. *Fluid Dynamics*, 1(1):1–4, 1966.

[36] Y Hirooka, G Mazzitelli, S Mirnov, M Ono, M Shimada, and FL Tabares. A review of the present status and future prospects of the application of liquid metals for plasma-facing components in magnetic fusion devices. *Fusion Science and Technology*, 68 (3):477–483, 2015.

[37] Muhammad Bilal, Kamran Ahmad, Muhammad Taimoor Saleem, Saira Gulfam, and Zahoor Ahmad. Recent progress, liquid metal use as plasma facing component and vapor shielding of high heat flux. *Reviews of Modern Plasma Physics*, 6(1):9, 2022.

[38] Davin Lunz. On thermal axisymmetric liquid-metal divertors. *Fusion Engineering and Design*, 158:111661, 2020.

[39] JA Shercliff. Steady motion of conducting fluids in pipes under transverse magnetic fields. In *Mathematical Proceedings of the Cambridge Philosophical Society*, volume 49, pages 136–144. Cambridge University Press, 1953.

[40] Chieh C Chang and Thomas S Lundgren. Duct flow in magnetohydrodynamics. *Zeitschrift für angewandte Mathematik und Physik ZAMP*, 12:100–114, 1961.

[41] JCR Hunt. Magnetohydrodynamic flow in rectangular ducts. *Journal of fluid mechanics*, 21(4):577–590, 1965.

[42] Keiji Miyazaki, Shoji Inoue, Nobuo Yamaoka, Tomomitsu Horiba, and Kazushige Yokomizo. Magneto-hydro-dynamic pressure drop of lithium flow in rectangular ducts. *Fusion technology*, 10(3P2A):830–836, 1986.

[43] A Ya Shishko. A theoretical investigation of steady-state film flows in a coplanar magnetic field. *Magnetohydrodynamics*, 28(2):170–182, 1993.

[44] E Platacis, A Flerov, A Klukin, S Ivanov, A Sobolevs, A Shishko, L Zaharov, and M Gryaznevich. Gravitational flow of a thin film of liquid metal in a strong magnetic field. *Fusion Engineering and Design*, 89(12):2937–2945, 2014.

[45] Zhen Sun, Jabir Al-Salami, Andrei Khodak, Francisco Javier Saenz Castro, Brian Wynne, Rajesh Maingi, Kazuaki Hanada, Changhong Hu, and Egemen Kolemen. Magnetohydrodynamics in free surface liquid metal flow relevant to plasma facing components. *Nuclear Fusion*, 2023.

[46] NB Morley, S Smolentsev, R Munipalli, M-J Ni, D Gao, and M Abdou. Progress on the modeling of liquid metal, free surface, MHD flows for fusion liquid walls. *Fusion Engineering and Design*, 72(1-3):3–34, 2004.

[47] Ahmed Hassanein. Modeling hydrogen and helium entrapment in flowing liquid metal surfaces as plasma-facing components in fusion devices. *Journal of nuclear materials*, 302(1):41–48, 2002.

[48] E Mas de Les Valls and L Batet. OpenFOAM capabilities for MHD simulation under nuclear fusion technology conditions. In *OpenFOAM workshop Milan*, pages 10–11, 2008.

[49] Tao Zhou, Zhiyi Yang, Mingjiu Ni, and Hongli Chen. Code development and validation for analyzing liquid metal MHD flow in rectangular ducts. *Fusion Engineering and design*, 85(10-12):1736–1741, 2010.

[50] Valdis Bojarevics, Alan A Roy, and Koulis Pericleous. Magnetic levitation of large liquid volume. *Magnetohydrodynamics*, 46(4):317–329, 2010.

[51] Seol Ha Kim, Moo Hwan Kim, Dong Won Lee, and Chiwoong Choi. Code validation and development for MHD analysis of liquid metal flow in Korean TBM. *Fusion Engineering and Design*, 87(7-8):951–955, 2012.

[52] PK Swain, P Satyamurthy, R Bhattacharyay, A Patel, A Shishko, E Platacis, A Ziks, S Ivanov, and AV Despande. 3D MHD lead–lithium liquid metal flow analysis and experiments in a test-section of multiple rectangular bends at moderate to high Hartmann numbers. *Fusion Engineering and Design*, 88(11):2848–2859, 2013.

[53] A Patel, R Bhattacharyay, R Srinivasan, E Rajendrakumar, P Bhuyan, P Satyamurthy, P Swain, and KS Goswami. 3D thermo-fluid MHD simulation of single straight channel flow in LLCB TBM. *Fusion Engineering and Design*, 87(5-6):498–502, 2012.

[54] Sergejs Spitans, Andris Jakovics, Egbert Baake, and Bernard Nacke. Numerical modeling of free surface dynamics of melt in an alternate electromagnetic field: Part I. Implementation and verification of model. *Metallurgical and Materials Transactions B*, 44:593–605, 2013.

[55] X Miao, D Lucas, Z Ren, S Eckert, and G Gerbeth. Numerical modeling of bubble-driven liquid metal flows with external static magnetic field. *International Journal of Multiphase Flow*, 48:32–45, 2013.

[56] Jingchao Feng, Hongli Chen, Qingyun He, and Minyou Ye. Further validation of liquid metal MHD code for unstructured grid based on OpenFOAM. *Fusion Engineering and Design*, 100:260–264, 2015.

[57] Andrei Khodak. Adaptation of general purpose CFD code for fusion MHD applications. In *2015 IEEE 26th Symposium on Fusion Engineering (SOFE)*, pages 1–5. IEEE, 2015.

[58] Andrei Khodak, Peter Titus, Thomas Brown, and Jonathan Klabacha. Numerical model of dual-coolant lead–lithium (DCLL) blanket. *Fusion Engineering and Design*, 137:124–129, 2018.

[59] Yi Yan, S Smolentsev, and M Abdou. Validation of COMSOL Multiphysics® for magnetohydrodynamics (MHD) flows in fusion applications. In *Proceedings of the COMSOL Conference, Boston, MA, USA*, volume 5, 2017.

[60] Shangjing Yang and Chang Nyung Kim. Magnetohydrodynamic flows in u-shaped ducts under a uniform transverse magnetic field. *Fusion Engineering and Design*, 121:87–99, 2017.

[61] S Sahu and R Bhattacharyay. Validation of COMSOL code for analyzing liquid metal magnetohydrodynamic flow. *Fusion Engineering and Design*, 127:151–159, 2018.

[62] Matthew Michael Szott. *Advanced geometries for dryout mitigation in TEMHD-driven liquid lithium systems*. PhD thesis, University of Illinois at Urbana-Champaign, 2020.

[63] Andrei Khodak. Numerical analysis of 2-D and 3-D MHD flows relevant to fusion applications. *IEEE Transactions on Plasma Science*, 45(9):2561–2565, 2017.

[64] Andrei Khodak, Fan Yang, and Howard A Stone. Free-Surface Liquid Lithium Flow Modeling and Stability Analysis for Fusion Applications. *Journal of Fusion Energy*, 39(6):455–461, 2020.

[65] A Khodak, C Kessel, and M Tillack. Design and analysis of the liquid metal free-surface divertor cooling system. *Fusion Science and Technology*, 75(8):930–938, 2019.

[66] M Szott, S Stemmley, C Moynihan, A De Castro, and DN Ruzic. Structured large-pore foams improve thermal performance of LiMIT-style liquid lithium PFC. *Nuclear Fusion*, 62(1):016018, 2021.

[67] Jacob AR Wright. A review of late-stage tungsten fuzz growth. *Tungsten*, 4(3):184–193, 2022.

[68] Mark R Gilbert, Jean-Christophe Sublet, and Robin A Forrest. *Handbook of activation, transmutation, and radiation damage properties of the elements simulated using FISPACT-II & TENDL-2014; Magnetic Fusion Plants*. Culham Centre for Fusion Energy, 2015.

[69] MR Gilbert, J-Ch Sublet, and SL Dudarev. Spatial heterogeneity of tungsten transmutation in a fusion device. *Nuclear Fusion*, 57(4):044002, 2017.

[70] Ch Linsmeier, M Rieth, J Aktaa, T Chikada, A Hoffmann, J Hoffmann, A Houben, H Kurishita, X Jin, M Li, et al. Development of advanced high heat flux and plasma-facing materials. *Nuclear Fusion*, 57(9):092007, 2017.

[71] Takeshi Hirai, S Panayotis, V Barabash, C Amzallag, F Escourbiac, A Durocher, M Merola, J Linke, Th Loewenhoff, G Pintsuk, et al. Use of tungsten material for the ITER divertor. *Nuclear Materials and Energy*, 9:616–622, 2016.

[72] JD Strachan, M Bitter, A T_ Ramsey, MC Zarnstorff, V Arunasalam, MG Bell, NL Bretz, R Budny, CE Bush, SL Davis, et al. High-temperature plasmas in a tokamak fusion test reactor. *Physical review letters*, 58(10):1004, 1987.

[73] RE Nygren and FL Tabarés. Liquid surfaces for fusion plasma facing components—A critical review. Part I: Physics and PSI. *Nuclear Materials and Energy*, 9:6–21, 2016.

[74] R Majeski. Liquid metal walls, lithium, and low recycling boundary conditions in tokamaks. In *AIP Conference Proceedings*, volume 1237, pages 122–137. American Institute of Physics, 2010.

[75] HW Kugel, JP Allain, MG Bell, RE Bell, A Diallo, R Ellis, SP Gerhardt, B Heim, MA Jaworski, R Kaita, et al. NSTX plasma operation with a liquid lithium divertor. *Fusion Engineering and Design*, 87(10):1724–1731, 2012.

[76] Robert Kaita, Laura Berzak, Dennis Boyle, Timothy Gray, Erik Granstedt, Gregory Hammett, Craig M Jacobson, Andrew Jones, Thomas Kozub, Henry Kugel, et al. Experiments with liquid metal walls: Status of the lithium tokamak experiment. *Fusion Engineering and Design*, 85(6):874–881, 2010.

[77] AY Ying, MA Abdou, N Morley, T Sketchley, R Woolley, J Burris, R Kaita, P Fogarty, H Huang, X Lao, et al. Exploratory studies of flowing liquid metal divertor options for fusion-relevant magnetic fields in the MTOR facility. *Fusion Engineering and Design*, 72(1-3):35–62, 2004.

[78] M Narula, A Ying, and MA Abdou. A study of liquid metal film flow, under fusion relevant magnetic fields. *Fusion Science and Technology*, 47(3):564–568, 2005.

[79] Michael George Hvasta, Egemen Kolemen, AE Fisher, and Hantao Ji. Demonstrating electromagnetic control of free-surface, liquid-metal flows relevant to fusion reactors. *Nuclear Fusion*, 58(1):016022, 2017.

[80] MG Hvasta, Egemen Kolemen, and A Fisher. Application of IR imaging for free-surface velocity measurement in liquid-metal systems. *Review of Scientific Instruments*, 88(1):013501, 2017.

[81] Juan-Cheng Yang, Tian-Yu Qi, Dong-Wei Ren, Bai-Qi Liu, and Ming-Jiu Ni. Rearrangement of liquid metal surface waves by a uniform transverse magnetic field. *Experiments in Fluids*, 59(11):1–16, 2018.

[82] J-C Yang, T-Y Qi, D-W Ren, M-J Ni, B-Q Liu, J-S Hu, and J-G Li. Magnetohydrodynamic effects on liquid metal film flowing along an inclined plate relating to plasma facing components. *Nuclear Fusion*, 60(8):086003, 2020.

[83] S Hammouti, B Holybee, M Christenson, M Szott, K Kalathiparambil, S Stemmley, B Jurczyk, and DN Ruzic. Wetting of liquid lithium on fusion-relevant materials microtextured by femtosecond laser exposure. *Journal of Nuclear Materials*, 508: 237–248, 2018.

[84] DN Ruzic, M Szott, C Sandoval, M Christenson, P Fiflis, S Hammouti, K Kalathiparambil, I Shchelkanov, D Andruczyk, R Stubbers, et al. Flowing liquid lithium plasma-facing components–Physics, technology and system analysis of the LiMIT system. *Nuclear Materials and Energy*, 12:1324–1329, 2017.

[85] M Nieto, DN Ruzic, W Olczak, and R Stubbers. Measurement of implanted helium particle transport by a flowing liquid lithium film. *Journal of nuclear materials*, 350 (2):101–112, 2006.

[86] D Andruczyk, R Rizkallah, D O'Dea, A Shone, S Smith, B Kamiyama, R Maingi, CE Kessel, S Smolentsev, TW Morgan, et al. Overview of Liquid-Metal PFC R&D at the University of Illinois Urbana-Champaign. *Fusion Science and Technology*, pages 1–14, 2023.

[87] Robert Kaita. Fusion applications for lithium: wall conditioning in magnetic confinement devices. *Plasma Physics and Controlled Fusion*, 61(11):113001, 2019.

[88] M Szott and DN Ruzic. 2-D moving mesh modeling of lithium dryout in open surface liquid metal flow applications. *Fusion Engineering and Design*, 154:111512, 2020.

[89] A Ibarra, F Arbeiter, D Bernardi, M Cappelli, A Garcia, R Heidinger, W Krolas, U Fischer, F Martin-Fuertes, G Micciché, et al. The IFMIF-DONES project: preliminary engineering design. *Nuclear Fusion*, 58(10):105002, 2018.

[90] D Bernardi, A Ibarra, F Arbeiter, F Arranz, M Cappelli, P Cara, J Castellanos, H Dzitko, A García, J Gutiérrez, et al. The IFMIF-DONES project: design status and main achievements within the EUROfusion FP8 work programme. *Journal of Fusion Energy*, 41(2):24, 2022.

[91] Egemen Kolemen, M Hvasta, R Majeski, R Maingi, A Brooks, and T Kozub. Design of the flowing liquid torus (flit). *Nuclear Materials and Energy*, 19:524–530, 2019.

[92] Robert James Goldston, Rachel Myers, and Jacob Schwartz. The lithium vapor box divertor. *Physica Scripta*, 2016(T167):014017, 2016.

[93] Jacob A Schwartz, Eric D Emdee, Robert James Goldston, and MA Jaworski. Physics design for a lithium vapor box divertor experiment on magnum PSI. *Nuclear Materials and Energy*, 18:350–355, 2019.

[94] TW Morgan, P Rindt, GG Van Eden, V Kvon, MA Jaworksi, and NJ Lopes Cardozo. Liquid metals as a divertor plasma-facing material explored using the Pilot-PSI and Magnum-PSI linear devices. *Plasma Physics and Controlled Fusion*, 60(1):014025, 2017.

[95] SI Krasheninnikov, LE Zakharov, and GV Pereverzev. On lithium walls and the performance of magnetic fusion devices. *Physics of Plasmas*, 10(5):1678–1682, 2003.

[96] Tingyi Liu, Prosenjit Sen, and Chang-Jin Kim. Characterization of nontoxic liquid-metal alloy galinstan for applications in microdevices. *Journal of Microelectromechanical Systems*, 21(2):443–450, 2011.

[97] G Cunningham. High performance plasma vertical position control system for upgraded MAST. *Fusion Engineering and Design*, 88(12):3238–3247, 2013.

[98] David Meeker. Finite element method magnetics. *FEMM*, 4(32):162, 2010.

[99] James D Widmer, Christopher M Spargo, Glynn J Atkinson, and Barrie C Mecrow. Solar plane propulsion motors with precompressed aluminum stator windings. *IEEE Transactions on Energy Conversion*, 29(3):681–688, 2014.

[100] Leif Siesing, Avo Reinap, and Mats Andersson. Thermal properties on high fill factor electrical windings: Infiltrated vs non infiltrated. In *2014 International Conference on Electrical Machines (ICEM)*, pages 2218–2223. IEEE, 2014.

[101] International Commission on Non-Ionizing Radiation Protection et al. Guidelines for limiting exposure to electric fields induced by movement of the human body in a static magnetic field and by time-varying magnetic fields below 1 Hz. *Health physics*, 106 (3):418–425, 2014.

[102] David Grainger et al. Safety guidelines for magnetic resonance imaging equipment in clinical use. *Published by the Medicines and Healthcare Products Regulatory Agency*, pages 1–85, 2014.

[103] TA Shedd and TA Newell. An automated optical liquid film thickness measurement method, Air Conditioning and Refrigeration Center, University of Illinois, Urbana-Champaign, USA. Technical report, ACRC TR-134, 1997.

[104] Arpita Dawda and Minh Nguyen. Comparison of Red versus Blue Laser Light for Accurate 3D Measurement of Highly Specular Surfaces in Ambient Lighting Conditions. In *International Symposium on Geometry and Vision*, pages 300–312. Springer, 2021.

[105] Kai Zhang, Tian Wei, and Hui Hu. An experimental investigation on the surface water transport process over an airfoil by using a digital image projection technique. *Experiments in Fluids*, 56(9):1–16, 2015.

[106] Timothy Allen Shedd and TA Newell. Automated optical liquid film thickness measurement method. *Review of Scientific Instruments*, 69(12):4205–4213, 1998.

[107] MA Jaworski, SP Gerhardt, NB Morley, T Abrams, R Kaita, J Kallman, H Kugel, R Majeski, and DN Ruzic. Macroscopic motion of liquid metal plasma facing components in a diverted plasma. *Journal of nuclear materials*, 415(1):S985–S988, 2011.

[108] Matthew Michael Szott. Flow control and associated technologies to advance the application of TEMHD-driven liquid lithium in fusion devices. 2016.

[109] JA Shercliff. Thermoelectric magnetohydrodynamics. *Journal of fluid mechanics*, 91 (2):231–251, 1979.

[110] Z Lei, D Raebiger, S Eckert, and K Eckert. Liquid metal based magnetic cooling: velocity measurements. *Magnetohydrodynamics*, 53(2):403–410, 2017.

[111] MD Nornberg, H Ji, JL Peterson, and JR Rhoads. A liquid metal flume for free surface magnetohydrodynamic experiments. *Review of Scientific Instruments*, 79(9):094501, 2008.

[112] DN Ruzic, W Xu, D Andruczyk, and MA Jaworski. Lithium–metal infused trenches (LiMIT) for heat removal in fusion devices. *Nuclear Fusion*, 51(10):102002, 2011.

[113] ANSYS CFX-Solver. Modelling guide. 2022.

[114] S Smolentsev, Santiago Badia, R Bhattacharyay, L Bühler, L Chen, Q Huang, H-G Jin, D Krasnov, D-W Lee, E Mas De Les Valls, et al. An approach to verification and validation of MHD codes for fusion applications. *Fusion Engineering and Design*, 100:65–72, 2015.

[115] Dmitry Krasnov, Oleg Zikanov, and Thomas Boeck. Numerical study of magneto-hydrodynamic duct flow at high Reynolds and Hartmann numbers. *Journal of Fluid Mechanics*, 704:421–446, 2012.

[116] Sergey Smolentsev, Tyler Rhodes, Yuchen Jiang, Peter Huang, and Charles Kessel. Status and progress of liquid metal thermofluids modeling for the US fusion nuclear science facility. *Fusion Science and Technology*, 77(7-8):745–760, 2021.

[117] ANSYS CFX-Solver. Theory guide. 2022.

[118] Ming-Jiu Ni, Ramakanth Munipalli, Neil B Morley, Peter Huang, and Mohamed A Abdou. A current density conservative scheme for incompressible MHD flows at a low magnetic Reynolds number. Part I: On a rectangular collocated grid system. *Journal of Computational Physics*, 227(1):174–204, 2007.

[119] Andrei Khodak. unpublished work submitted to fusion and engineering design. unpublished work submitted to Fusion and Engineering Design.

[120] C Mistrangelo, L Bühler, S Smolentsev, V Klüber, I Maione, and J Aubert. MHD flow in liquid metal blankets: Major design issues, MHD guidelines and numerical analysis. *Fusion Engineering and Design*, 173:112795, 2021.

[121] BS Massey. Mechanics of Fluids 4th Edition. *The English Language Book Society*, 1980.

[122] Ven Te Chow. Open-channel hydraulics: New York. *US Army Corps of Engineers, Hydrologic Engineering*, 1959.

[123] D Krasnov, Thomas Boeck, L Braiden, Sergej Molokov, and Leo Bühler. *Numerical simulations of MHD flow transition in ducts with conducting Hartmann walls: Limtech Project A3 D4 (TUI)*, volume 7713. KIT Scientific Publishing, 2016.

[124] Maximilian Fleischer and Hans Meixner. Gallium oxide thin films: a new material for high-temperature oxygen sensors. *Sensors and Actuators B: Chemical*, 4(3-4): 437–441, 1991.

[125] Dawei Wang, Xiaohong Wang, and Wei Rao. Precise regulation of Ga-based liquid metal oxidation. *Accounts of Materials Research*, 2(11):1093–1103, 2021.

[126] XiaoLin Yuan, Yue Chen, JianSheng Hu, JianGang Li, GuiZhong Zuo, Jun Ren, Yue Zhou, ChangZheng Li, Zheng Sun, Wei Xu, et al. Development and implementation of flowing liquid lithium limiter control system for EAST. *Fusion Engineering and Design*, 112:332–337, 2016.

[127] JS Hu, GZ Zuo, R Maingi, Z Sun, K Tritz, W Xu, QX Yang, D Andruczyk, M Huang, XC Meng, et al. Experiments of continuously and stably flowing lithium limiter in east towards a solution for the power exhaust of future fusion devices. *Nuclear Materials and Energy*, 18:99–104, 2019.

[128] Rajesh K Singh, Janine E Galvin, and Xin Sun. Three-dimensional simulation of rivulet and film flows over an inclined plate: Effects of solvent properties and contact angle. *Chemical Engineering Science*, 142:244–257, 2016.

[129] A Bondi. The Spreading of Liquid Metals on Solid Surfaces. Surface Chemistry of High-Energy Substances. *Chemical Reviews*, 52(2):417–458, 1953.

[130] Guillaume Lamour, Ahmed Hamraoui, Andrii Buvailo, Yangjun Xing, Sean Keuleyan, Vivek Prakash, Ali Eftekhari-Bafrooei, and Eric Borguet. Contact angle measurements using a simplified experimental setup. *Journal of chemical education*, 87 (12):1403–1407, 2010.

[131] Zhiwei Li, Ji Li, Xingping Li, and Ming-Jiu Ni. Free surface flow and heat transfer characteristics of liquid metal Galinstan at low flow velocity. *Experimental Thermal and Fluid Science*, 82:240–248, 2017.

[132] Tiago Ferreira and Wayne Rasband. ImageJ user guide. *ImageJ/Fiji*, 1:155–161, 2012.

[133] Ethan Allan Davis. On The Wetting States of Low Melting Point Metal Galinstan and Wetting Characteristics of 3-Dimensional Nanostructured Fractal Surfaces. 2017.

[134] Weiguang Lin, Wangkang Qiu, Yisimayili Tuersun, Xu Huang, and Sheng Chu. Ultrastrong Spontaneous Surface Wetting of Room Temperature Liquid Metal on Treated Metal Surface. *Advanced Materials Interfaces*, 8(18):2100819, 2021.

[135] MM Sarafraz and M Arjomandi. Contact angle and heat transfer characteristics of a gravity-driven film flow of a particulate liquid metal on smooth and rough surfaces. *Applied Thermal Engineering*, 149:602–612, 2019.

[136] Jiangyan Wang, Hansen Wang, Jin Xie, Ankun Yang, Allen Pei, Chun-Lan Wu, Feifei Shi, Yayuan Liu, Dingchang Lin, Yongji Gong, et al. Fundamental study on the wetting property of liquid lithium. *Energy Storage Materials*, 14:345–350, 2018.

[137] M Mayer, S Krat, W Van Renterghem, A Baron-Wiechec, S Brezinsek, Igor Bykov, P Coad, Yu Gasparyan, K Heinola, J Likonen, et al. Erosion and deposition in the JET divertor during the first ILW campaign. *Physica Scripta*, 2016(T167):014051, 2016.

[138] Igor Veretennikov, Alexandra Indeikina, and Hsueh-Chia Chang. Front dynamics and fingering of a driven contact line. *Journal of Fluid Mechanics*, 373:81–110, 1998.

[139] P Fiflis, A Press, W Xu, Daniel Andruczyk, Davide Curreli, and David N Ruzic. Wetting properties of liquid lithium on select fusion relevant surfaces. *Fusion Engineering and Design*, 89(12):2827–2832, 2014.

[140] Yang Yu, Qian Wang, Liting Yi, and Jing Liu. Channelless Fabrication for Large-S cale Preparation of Room Temperature Liquid Metal Droplets. *Advanced Engineering Materials*, 16(2):255–262, 2014.

[141] Amanda Koh, Wonseok Hwang, Peter Y Zavalij, Seth Chun, Geoffrey Slipher, and Randy Mrozek. Solidification and melting phase change behavior of eutectic gallium-indium-tin. *Materialia*, 8:100512, 2019.

Appendix A

Data Processing MATLAB File

```
clc
clear
close all

TotalRuns= 1010; %Change for each trial
LaserFreq=25;  %samples/sec
filename= 'Aug8_2023_streamwise_Cu_Ha3_Re2_Flat_V1_'; %Change for each trial
LowerRange = 338; %Change for each trial
HigherRange = 346; %Change for each trial
bounds = -20:0.001:30;  %Change for each trial


% save flat plate data
Data = readtable('Aug7_2023_EmptyFlatPlateV4_00001.xlsx','ReadVariableNames',false );
Data.Properties.VariableNames = ["StreamwiseLocation","Height"];
idx = Data.Height >= LowerRange & Data.Height<= HigherRange;
FlatPlate(:,1) = Data(idx,1);
FlatPlate(:,2) = Data(idx,2);


%

%Data smoothing
% FlatPlate.Var2=smooth(FlatPlate.Transverse1,FlatPlate.Var2,0.01,'rloess');
% LMLevel.Var2=smooth(LMLevel.Transverse2,LMLevel.Var2,0.01,'rloess');
%
[~, ind] = unique(FlatPlate.StreamwiseLocation); % ind = index of first occurrence of
interpolation1 = interp1(FlatPlate.StreamwiseLocation(ind),FlatPlate.Var2(ind),bounds,


%Create a table for the full data setdataset
dataset = array2table(zeros(0,3));
dataset.Properties.VariableNames = ["Time","StreamwiseLocation","Height"]; %Add column


    for k = 1:TotalRuns

     % Retrieves the relevant excel file
     filenum = num2str(k,'%05.f'); %Defines file number in format 00001, etc
```

```
41      filetype = '.xlsx'; %Defines file type
42      Fullfilename= strcat(filename,filenum, filetype); %Defines full file name
43
44
45      %Saves the data to a temporary table
46      LMData = readtable(Fullfilename,'ReadVariableNames',false);
47      LMData.Properties.VariableNames = ["StreamwiseLocation","Height"];
48
49
50      %FilterNoise and save only those filtered points
51      idx = LMData.Height >= LowerRange & LMData.Height <= HigherRange;
52      LMData =  LMData(idx,:);
53
54
55
56
57
58  %make interpolation
59  [~, ind] = unique(LMData.StreamwiseLocation); % ind = index of first occurrence of a
60  % W= LMData.StreamwiseLocation(ind);
61  % D= LMData.Height(ind);
62  W = table2array(LMData(ind,1));
63  D = table2array(LMData(ind,2));
64  interpolation2 = interp1(W,D,bounds,'linear','extrap');
65
66  %Calculate true height
67  difference = interpolation2-interpolation1;
68
69
70  difference = array2table(difference');
71  difference.Properties.VariableNames = ["Height"];
72  bounds = array2table(bounds');
73  bounds.Properties.VariableNames = ["StreamwiseLocation"];
74
75   %Saves the timestep value for this round
76      NumberValues = length(interpolation1);  %Count number of new entries to the overa
77      Time= table((k)*(1/LaserFreq)*ones(NumberValues,1));
78      Time.Properties.VariableNames = ["Time"];
79
80
81
82
83  %Save data in overall dataset
84      dataset = [dataset; bounds difference Time]; %Adds data to overall table
85
86
87
88     bounds = table2array(bounds); %ditto
89      interpolation2 = interpolation2';
90      bounds = bounds';
91     end
92  bounds = bounds';
93  difference = table2array(difference);
94  figure()
95  hold on
96  plot(bounds, difference)
97  xlabel("x (mm)")
98  ylabel("Depth (mm)")
```

```
99  hold off
100
101 % figure()
102 % hold on
103 % plot(bounds, interpolation1, bounds, interpolation2)
104 % xlabel("x (mm)")
105 % ylabel("Depth (mm)")
106 % hold off
107
108 figure()
109
110 %% Generate a 3D plot of the depth profiles over time
111
112 %Non uniform data interpolation to generate a grid
113 MinTransverse = min(dataset{:,2});
114 MaxTransverse = max(dataset{:,2});
115 MinTime = min(dataset{:,1});
116 MaxTime = max(dataset{:,1});
117 [TimeBounds,TransverseBounds] = meshgrid(MinTime:.02:MaxTime, MinTransverse:.02:MaxTra
118 DepthGrid = griddata(dataset.Time, dataset.StreamwiseLocation, dataset.Height, TimeBou
119
120
121
122
123 %Plot the surface map of transverse depth over time
124 mesh(TransverseBounds,TimeBounds,DepthGrid)
125 hold on
126 %plot3(fdataset.fdataset2, fdataset.fdataset1, fdataset.fdataset3,'.')
127
128 xlabel('Position along laser line (mm)')
129 ylabel('Time (s)')
130 zlabel('Depth (mm)')
131
132 hold off
133
134 %% Generate a plot of average depth over all timesteps
135 hold on
136 means = varfun(@mean,dataset,"InputVariables","Height", "GroupingVariables","Time"); %
137 WindowSize = 20; %Moving average filter window size, adjust as needed
138 coeff = (1/WindowSize)*ones(1,WindowSize);
139 filteredDepth = filter(coeff, 1, means.mean_Height); %Moving average noise filter (fil
140
141 figure() %Prevents Matlab from overwriting the initial plot
142 plot(means.Time, filteredDepth)
143 xlabel('Time (s)')
144 ylabel('Average Depth (mm)')
145
146 hold off
```

Appendix B

Particle Tracking Velocity Method

The work included in this section was completed in collaboration with an undergraduate intern, James Leader, in the summer of 2021.

The tracking of frozen galinstan particles partly suspended in liquid galinstan could provide useful measures of bulk liquid metal flow. Such a particle would move with the galinstan flow due to density similarity, but would be visible from the free surface. The magnitude of the particle would need to be large enough to submerge sufficiently with the bulk fluid whilst remaining partially unsubmerged. As the projected liquid metal films were on the order of mm, a 2 mm frozen galinstan particle was viewed as an ideal size to test.

These particles must possess a low enough temperature to allow for their integration into the flowing liquid metal film for long enough for measurements to be made. The particle must also melt before reaching the pump to avoid pump failure. To investigate the optimal particle temperature and initial diameter, an analytical model of a solid, spherical particle submberged in stationary medium was developed.

Galinstan Particle Melting Model

A mathematical model was developed to estimate the melting time for a solid, spherical particle submerged in a stationary medium. To simplify the model, the temperature distribution within the particle as it melts was ignored, so particle temperature was modelled as a uniform, lumped property for the entire sphere. A diagram of the model geometry is found in Figure B.1 and the key parameter symbols are defined in Table B.1.

The melting of a particle can be described in two stages:

1. Stage 1: The warming stage, where the particle warmed to the melting point and no changes in particle volume were assumed. The rate of increase of particle internal energy was equated to the instantaneous heat flux across the particle boundary.

2. Stage 2: The melting stage, where the particle volume reduced as the particle continued to increase in temperature. The heat flux required for phase change was equated to the heat flux across the (shrinking) particle boundary at constant particle temperature.

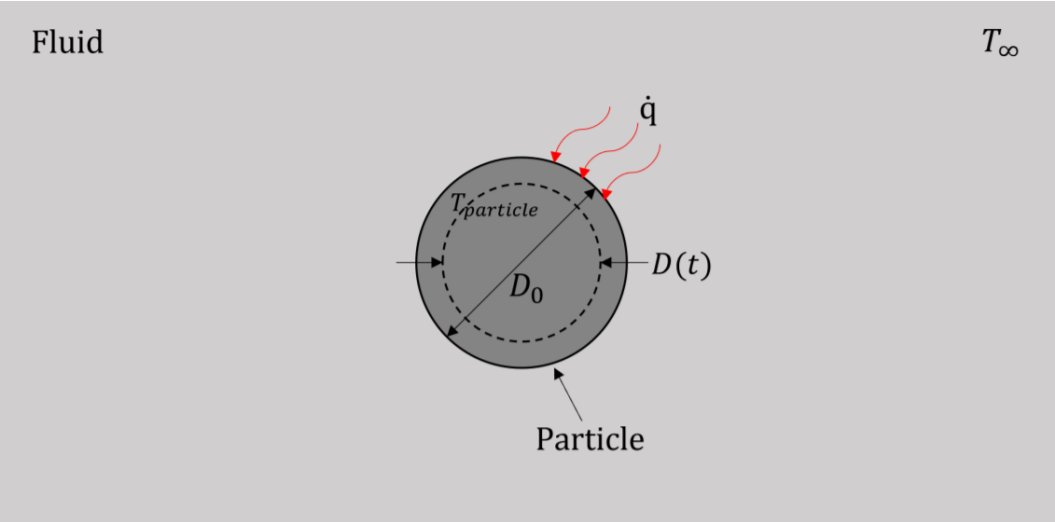


Figure B.1: Schematic of the simplified model of solid metal melting in an ambient pool of liquid.

The warming stage was defined by Equation B.1:

$$mc\frac{dT_{particle}}{dt} = hA(T_\infty - T_{particle}) \tag{B.1}$$

and the melting stage was defined by Equation B.2:

$$m\Delta h_f \frac{df}{dt} = hA\,(T_\infty - T_{MP}) \tag{B.2}$$

where f was the volumetric liquid fraction which increased from 0 to 1 during melting. The Nusselt number was known to be two for a submerged sphere in a stationary medium (Nu = 2). By definition, the convective heat transfer coefficient, h [$\mathrm{Wm^{-2}K^{-1}}$], was then given by Equation B.3. The geometric parameters were evaluated for a sphere as in Equations B.4 and B.5. The particle diameter is $D = D_0$ during the warming stage, and $D = (1-f)^{\frac{1}{3}}D_0$ during the melting stage.

$$h = \frac{2k_{fluid}}{D} \tag{B.3}$$

$$m = \rho\frac{4}{3}\pi\left(\frac{D}{2}\right)^3 \tag{B.4}$$

$$A = 4\pi\left(\frac{D}{2}\right)^2 \tag{B.5}$$

This two-part model was analytically solved to predict the time required for a particle to completely melt.

The time taken for a particle to reach its melting point, τ_{warm}, was given by Equation B.6. The time taken for a particle to melt at its melting point, τ_{melt}, was given by Equation B.7.

Table B.1: Parameters used in the model equations. Parameters without a subscript are always particle properties.

Symbol	Description	Unit
h	Convective heat transfer coefficient	$\mathrm{Wm^{-2}K^{-1}}$
k_{fluid}	Thermal conductivity of the fluid	$\mathrm{Wm^{-1}K^{-1}}$
$k_{particle}$	Thermal conductivity of the particle	$\mathrm{Wm^{-1}K^{-1}}$
c	Specific heat capacity of particle	$\mathrm{Jkg^{-1}K^{-1}}$
Δh_f	Latent heat of fusion of the particle	$\mathrm{Jkg^{-1}}$
D	Particle diameter	m
D_0	Initial particle diameter	m
m	Particle mass	kg
A	Particle surface area	$\mathrm{m^2}$
$T_{particle}$	Particle temperature (uniform throughout)	K
T_0	Initial particle temperature	K
T_{MP}	Particle melting point	K
T_∞	Far-field fluid temperature (assumed constant)	K
ρ	Particle density	$\mathrm{kgm^{-3}}$

The variation of fluid fraction with time, $f(t)$, was given by Equation B.8.

$$\tau_{warm} = \frac{\rho c D_0^2}{12 k_{fluid}} \ln \frac{T_\infty - T_0}{T_\infty - T_{MP}} \tag{B.6}$$

$$\tau_{melt} = \frac{3}{5} \frac{\rho D_0^2 \Delta h_f}{12 k_{fluid}(T_\infty - T_{MP})} \tag{B.7}$$

$$f = 1 - \left(1 - \frac{5}{3} \frac{12 k_{fluid}(T_\infty - T_{MP})}{\rho D_0^2 \Delta h_f} t\right)^{\frac{3}{5}} \tag{B.8}$$

The accuracy of this model increased as the Biot number decreased (Equation B.9). A Biot number less than 0.1 was considered sufficiently small for good model accuracy. The Biot number for frozen galinstan particles melting in liquid galinstan was 2, which was relatively high and limited the accuracy of this model. A table of relevant physical properties are in B.2.

$$Bi = \frac{hD}{k_{particle}} \tag{B.9}$$

Applying this model to frozen galinstan particles melting in a pool of liquid galinstan produced Figure B.2. The initial flat portion of the curve corresponded to the warming phase, and the remainder of the curve represented the melting phase. The warming time, τ_{warm} was predicted to be insignificant compared to the melting time, τ_{melt}.

From Figure B.2, the melting time for a 2 mm galinstan particle initially at -18°C in a pool at 25 galinstan was 0.5 seconds. This time frame was quite small, as the frozen galinstan particle would need to exist above 2 mm in diameter in liquid galinstan for several seconds to

Table B.2: Physical constants used in the melting particle model to produce the melting curves shown in Figures B.2 and B.6.

Material	Property	Value	Unit	Comments
Galinstan	Density (ρ)	6440	kgm^{-3}	
Galinstan	Specific heat capacity (c)	296	$Jkg^{-1}K^{-1}$	
Galinstan	Thermal conductivity (k_{fluid})	16.5	$Wm^{-1}K^{-1}$	
Galinstan	Melting point (T_{MP})	10.9	C	From observations of the bulk melting point.
Galinstan	Latent heat of fusion (Δh_f)	80100	Jkg^{-1}	Approximated as equal to that of gallium.
Water	Thermal conductivity (k_{fluid})	0.598	$Wm^{-1}K^{-1}$	

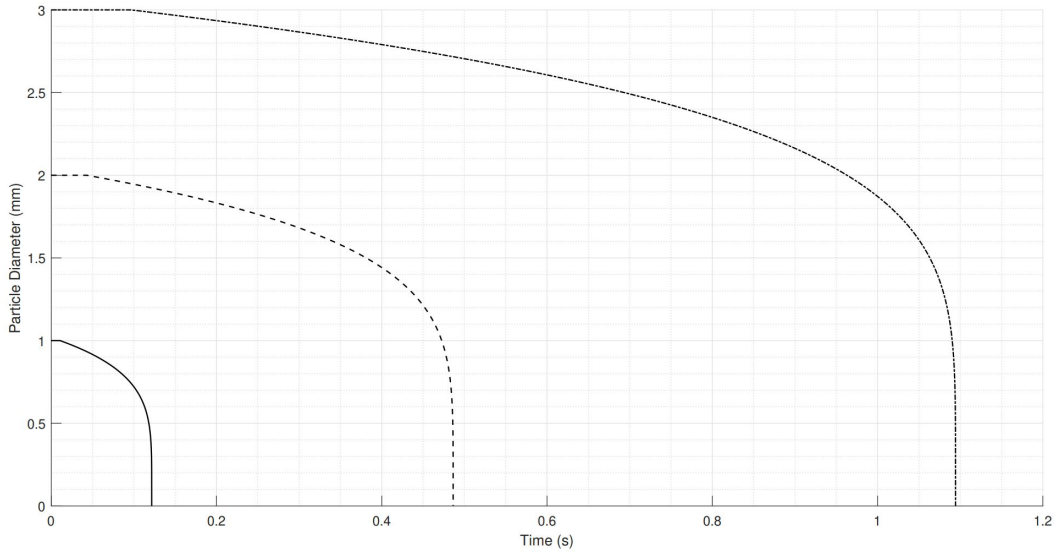


Figure B.2: Melting curves for spherical galinstan particles of various initial diameter, with an initial temperature of -18°C, submerged in room temperature (25°C) galinstan.

allow for particle embedding and movement to the inlet, and additionally for at least 2 more seconds as it flowed down the channel. The particle lifetime could be increased by increasing the initial particle diameter or reducing the initial particle temperature. The initial temperature of the particle was limited by the temperature of the in-house freezer. The particle size was limited by the fabrication method described in the next section, and the practicality of embdedding larger particles into the flowing liquid metal. Another possible solution was using gallium rather than galinstan particles, because gallium has a higher melting point (29.8°C) than galinstan (10°C) and would thus stay solid in solution for longer. Though in using gallium, considerations around altering the chemical composition of the bulk galinstan should be considered if large amounts of gallium are introduced.

The next section will describe the fabrication of galinstan and gallium micro particles, attempts to embed these particles in liquid galinstan, and experimental validation of this analytical model.

Experimental Method Development

2 mm frozen galinstan and gallium particles were created at OTI following a procedure suggested by Yu et al (140). The procedure was as follows:

Procedure for Making Frozen Galinstan/Gallium Particles:

1. Prepare 20 grams per litre of sodium dodecyl sulfate (SDS) in deionised water. The SDS is used to prevent the particles from coalescing.
2. Fit a 2.5 mL syringe with a 16 gauge needle and fill will galinstan/gallium to produce 2mm spheres (see Figure B.3).
3. Quickly release galinstan from the syringe into the SDS-water solution. Galinstan/gallium droplets should form (Figure B.4).
4. To decrease droplet size either use a smaller gauge needle or increase jetting velocity.
5. Freeze solution at –10°C so galinstan/gallium droplets solidify.
6. Cool solution to 4°C (fridge temperature).
7. Remove solid galinstan/gallium particles from solution using a fine sieve .
8. Quickly mix frozen galinstan/gallium particles with liquid galinstan just before the channel inlet (see Figure B.8).

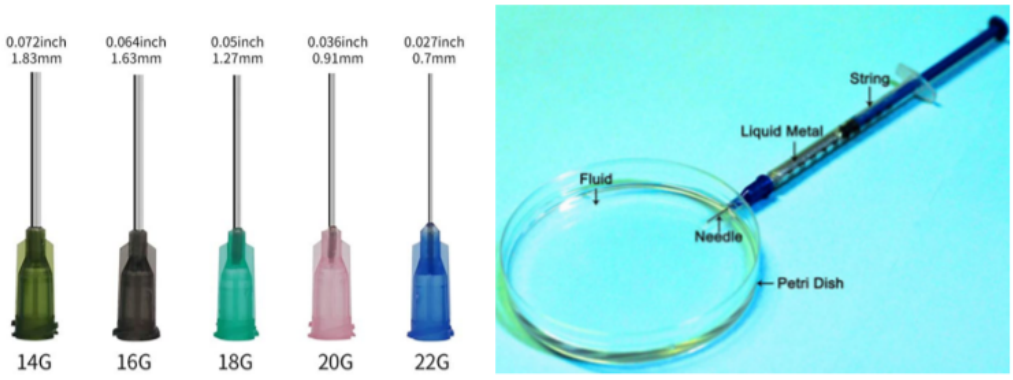


Figure B.3: **a)** Needle sizes available in the OTI lab. The measurements correspond to the needle inner diameters. **b)** An image of liquid metal being injected into the surfactant solution during the particle fabrication method. Image from (140)

Initially, galinstan spheres were attempted using the method described above. Liquid galinstan spheres did form in SDS solution (see Figure B.5 (A)), but attempts to freeze and isolate the galinstan spheres were unsuccessful. Interestingly, bulk amounts of galinstan were found to freeze at 10°C in the freezer, but micro particles remained liquid at -18°C (freezer temperature). This was likely due to a supercooling affect that occured at the micro scale

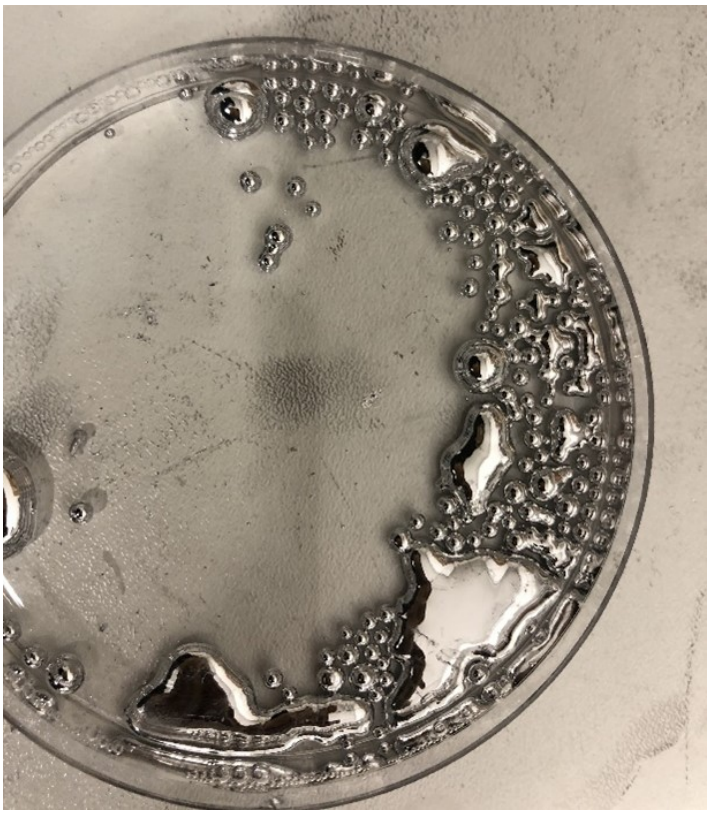


Figure B.4: Liquid galinstan droplets in SDS-water solution at room temperature

that reduced the melting point of galinstan (141). Both gallium and galinstan experienced a supercooling phenomena, which complicated the freezing regime especially at the micro scale. Supercooling occured in metals that had low melting points because these metals crystallised in lower symmetries. This was what causes gallium to melt at temperatures below the melting point and galinstan to begin to freeze at 10°C but not solidify until -19°C.

An attempt to make galinstan particles without the SDS solution was made by pipetting galinstan drops onto a petri dish and freezing overnight. Galinstan spheres formed in petri dishes that were uncovered (see Figure B.5(B)), but not in those that were covered (the reason for this is not yet understood). Any remaining liquid drops could solidify instantaneously by piercing the outer surface with a sharp instrument, likely because the piercing served as a source for nucleation that restructures the galinstan atoms into a crystalline structure characteristic of the solid phase. Accordingly, it was determined that fabricating 2 mm galinstan spheres is not feasible for these experiments.

Attempts to make gallium spheres were more successful. Gallium did also supercool, but due to the higher initial melting point, the -18°C freezer temperature was adequate to freeze gallium micro particles (see Figure B.5(C,D)).

For this experiment, the size of producible spherical particle was restricted to a maximum of 2 mm, above which the particles do not suspend adequately in the liquid SDS solution and appeared as disks similar to B.5 (B). Larger particles could be manufactured with the use of a deeper petri dish to balance buoyant forces of the particle with gravity.



Figure B.5: Results from particle fabrication trials. **A)** Liquid galinstan spheres of < 1 mm diameter in solid SDS solution. **B)** Solid galinstan particles formed from droplets. **C)** A successful batch of solid spherical gallium particles, with diameters in the range 2-4 mm. **D)** Spherical gallium particles with 2 mm diameter.

An attempt to validate the analytical model was attempted using non-spherical, frozen galinstan particles similar to those in B.5 (B) in water. Using water as the liquid medium both significantly increased the melting time (see Figure B.6) and allowed for visual confirmation of particle melting. The effective spherical diameter of the galinstan particle was determined by weighing the galinstan particle and correlating the mass to the equivalent spherical particle size.

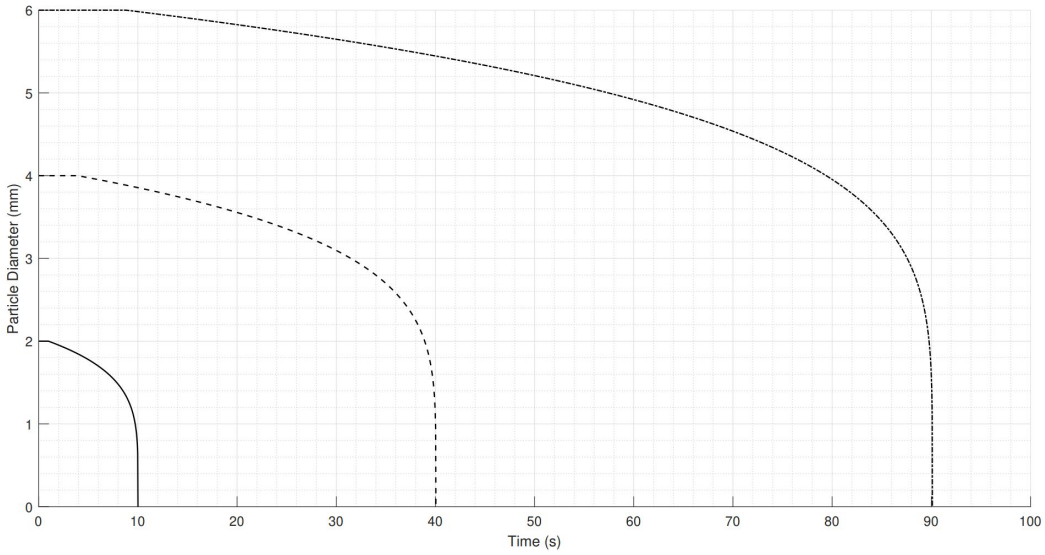


Figure B.6: Melting curves for spherical galinstan particles of various initial diameter, with an initial temperature of -18°C, submerged in 30°C water.

The galinstan particles were dropped in a clear funnel suspended in a bath of warm water at various temperatures (see Figure B.7). For each measurement, the galinstan particles were quickly transferred from the -18°C freezer and dropped into the warm water bath. Solid and liquid galinstan were visibly indistinguishable, so the galinstan particle was assumed to be melted when the galinstan fall through the stem of the funnel.

Twelve trials were conducted at a variety of water temperatures ranging from 34.9°C to 38.4°C. The analytical model results were on average 3.3 times greater than the experimental results. For galinstan melting in water, the Biot number was 0.0725, which would suggest that the analytical results should be accurate (Bi $<$ 0.1). There were a number of possible causes for the differences between the model and experimental results including the non-spherical particle shape, conductive heat transfer through the did does not account for the complex supercooling regime of galinstan, which as mentioned before varies significantly depending on particle size. Upon further validation studies, if the model consistently over-predicted the melting time by a factor of 3.3, then this could be accounted for in the model.

After the gallium particles were created, they could be used to track velocity using either the ScanControl system to track the unsubmerged top portion of the particle, the IR camera if the sphere is oxidized, or using the visual camera.

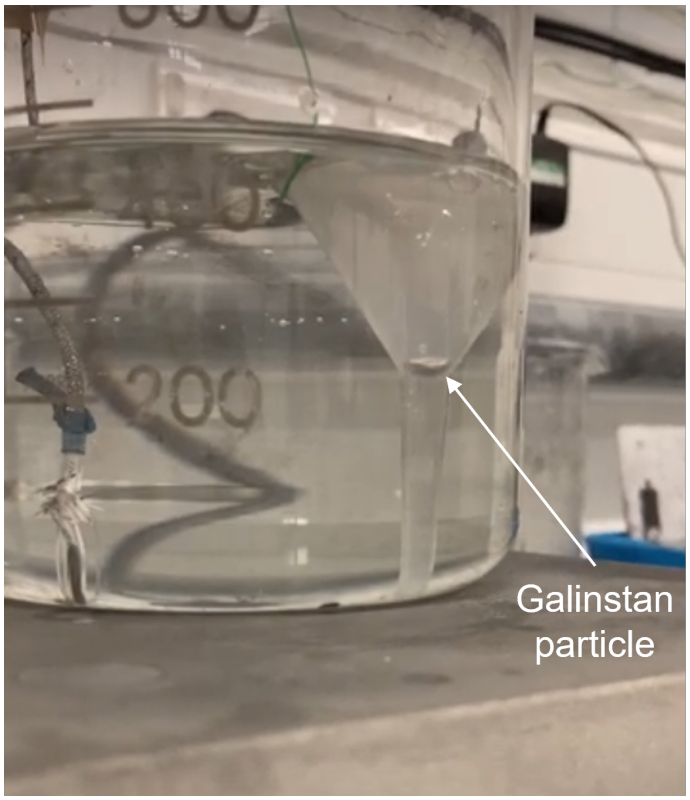


Figure B.7: Setup of the model verification experiment. An initially solid galinstan particle is placed within the Y of a funnel which is submerged in a heated water bath.

To embed the gallium particles in the liquid galinstan flow with minimal flow disruption and addition of ambient oxygen, a modification to the piping system was proposed (Figure B.8). The galinstan feed from the flowmeter was split in two using a Y junction. One line had plain galinstan flow and the second allowed for liquid galinstan to mix with the solid gallium particle feed. When the second galinstan line was filled, gate valves were used to allow for the mixed liquid and solid particle galinstan feed to flow to the channel so that a velocity measurement could be made.

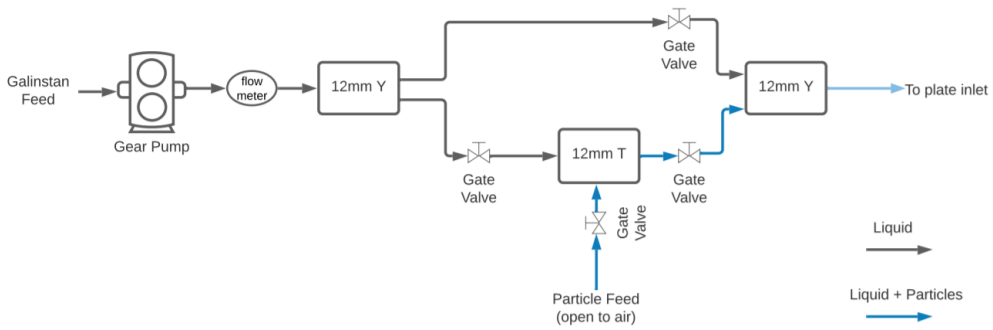


Figure B.8: Process and Instrumentation Diagram for a method to embed particles. The black lines show liquid galinstan lines and the blue lines have liquid galinstan and solid gallium.

Due to supercooling, gallium particles did melt in room temperature galinstan solution.

This was actually a favourable reaction as it minimised chance of pump failure from clogging. However, the time frame required for a partially submerged gallium (and also galinstan) particle to melt was difficult to predict due to supercooling and the seemingly high dependence of melting temperature on particle diameter in the micro regime. A 2 mm sphere of gallium placed on the surface of a pool of room temperature melted in 10 minutes. An attempt to flow the gallium particles on the flowing galinstan surface was made, but the particle remained stationary on the surface.

At the moment, neither gallium or galinstan particles can readily be used to track bulk velocity due to instantaneous melting that occurs when these particles are partially submerged. However, in the future, use of a colder freezer to overcome supercooling effects or exploitation of the spontaneous nucleation effect could yield galinstan micro particles.